Understanding Melting in Fused Filament Fabrication Process

José Luis Colón Quintana

A preliminary report submitted in partial fulfillment
of the requirements for the degree of

Doctor of Philosophy (Mechanical Engineering)

at the

University of Wisconsin-Madison

2021

Date of examination: August 10^{th}, 2021

The following are the members of the preliminary examination:

Tim A. Osswald, Professor, Mechanical Engineering

Lih-Sheng Turng, Professor, Mechanical Engineering

Pavana Prabhakar, Professor, Civing and Environmental Engineering

Alejandro Roldán-Alzate, Professor, Mechanical Engineering

Abstract

During the fused filament fabrication (FFF) process, understanding the melting mechanism is essential to model and predict the efficiency rate during extrusion. Efficiency is achieved when printing at the highest printing velocity is reached. Current FFF processes use low printing speeds to avoid under-extrusion and subsequently producing a faulty part. To successfully print at higher velocities, it is crucial to predict the feeding rate as a function of the material properties and its force. The work presented here allows understanding the melting mechanisms during an FFF process and improves an existing model based on the results.

The second chapter of the manuscript summarizes and discusses the state-of-the-art in the field of the FFF process. In particular, it discusses previous models analyzing the melting process and the prediction of filament velocity. For decades, a significant challenge in this process has been understanding and forecasting the printing speed of these machines. Hence, a fundamental part of this work proposal involves improving the melting models available in the present. In particular, the FFF melting model proposed by Osswald et al. [1] uses the concept of the pressure-induced melt removal process as its core.

The third chapter, a theoretical background, provides the basic knowledge necessary to understand the work presented here.

The fourth chapter focuses on understanding the base assumption of the pressured-induced melt removal process, backbone of the Osswald et al. model [1]. Experimental results were acquired and compared with analytical solutions and numerical simulations. Computed tomography technology was employed to visualize the melt film formation. An understanding of the melting temperature for amorphous materials was achieved. A distinguished transition on viscosity was observed for the amorphous materials suggesting that the melting temperature equals the glass transition temperature. Good prediction between all the methods was achieved. Results give insights into the melting phenomena of materials during the fused filament fabrication process.

The fifth chapter shows an improvement performed to the Osswald et al. model [1]. The model is improved by taking into account the shear-thinning behavior of the polymer material by including the power-law model as the viscosity model. This model will be called the Osswald-Colon model. Equations, model assumptions, and considerations are explained in detail. The model shows good agreement with experimental results assuming that the melting temperature of both amorphous and semi-crystalline materials equal the glass transition temperature. For the semi-crystalline material, a comparison was made

using the glass transition temperature and melting temperature. Moreover, a radiation heat transfer analysis was performed to account for the heating from the heated walls to the filament material.

The sixth chapter studies radiation heat transfer and nozzle diameter on a range of melting models. The radiation heat transfer was implemented to both the Osswald et al. model and the Osswald-Colon model. The radiation approach calculates the initial temperature of the filament as a function of filament velocity. Later, the melt film thickness is calculated and input into both melting models. The models are compared with experimental data obtained from a customized FFF machine. The data processed allowing the understanding of the critical force where slippage occurs. It was shown that the slippage would be dependent on the material properties and not the printing parameters. A good prediction was made when calculating the theoretical, critical force. It was shown the Osswald-Colon model approximates the best for the ABS data. However, this is not true when predicting the PLA data under the assumption of using the actual melting temperature (not the glass transition temperature). The results give insight into what models best describe the FFF process for a range of materials, nozzle diameters, and process temperature.

Based on the measurements, concepts, and results, future work is proposed in Chapter 7. A suggested setup is presented to visualize the density difference between solid and melted material during extrusion on a FFF machine. It is proposed to use a different boundary condition on the Osswald et al. model and Osswald-Colon model, which considers the velocity component in the r-direction. Also, it is suggested that experiments should be done to determine the contact area between the feeding mechanism and filament velocity for a range of FFF machines.

Acknowledgments

First, I thank my advisor and mentor, Professor Tim Osswald, for his technical and emotional support during this dissertation. Thank you for sharing your enthusiasm and for all the opportunities to grow as a researcher and individual.

My deepest gratitude to the members of my dissertation committee: Prof. Lih-Sheng Turng, Prof. Pavana Prabhakar, and Prof. Alejandro Roldan. Your encouragement and suggestions have been invaluable. I am grateful to have had the chance to learn from you all. In addition, there are many students and visiting scholars who made this research possible, including Friederike Burke, Nils Kroschel, Jesse Pollock, George Halunen, and Adam Schyvinck. Finally, I must also thank all the members of the Polymer Engineering Center for the discussions, ideas, support, and friendships. In particular, thank you to Gerardo Mazzei and John Estela. We experienced the best and worst of additive manufacturing technology and rheology together.

I want to thank my family for all the encouragement, my mother and father for always encouraging me to pursue my dreams and never give up. Thanks for always believing in me. Thanks to my grandparents for always loving and believing in me. To my sister, although we are constantly fighting, I still love you. Finally, I want to thank Nancy, my partner in crime, for being my unwavering support and being there in my worst and good moments, especially in the good moments. Those will never disappear from my mind. Thank you for always giving me moral support in the process and for always making me happy. Thanks for always smiling and being the wonderful person you are.

Symbols and Acronyms

Acronyms

CO	carbon monoxide
CO_2	carbon dioxide
HCL	hydrochloric acid
Tr	Trouton ratio
ABS	Acrylonitrile butadiene styrene
CT	Computed Tomography
CY	Carreau-Yasuda
DMA	Dynamic Mechanical Analysis
DSC	Differential Scanning Calorimeter
FFF	Fused Filament Fabrication
PA6	Polyamide 6 (Nylon)
PC	Polycarbonate
PL	power-law
PLA	Polylactic acid
PP	Polypropylene
PVC	Polyvinyl chloride
TGA	Thermogravimetric Analysis
TTS	Time-Temperature-Superposition

Symbols

T_m	melting temperature	^oC - K
$\dot{\gamma}$	shear rate	1/s
$\dot{m}_s$	mass flow rate of solid material	$\frac{kg}{s}$
$\eta_o(T)$	viscosity at the processing temperature	Pa-s
$\eta_o(T_{ref})$	viscosity at the reference temperature	Pa-s
$\hat{\rho}$	solid/melt density ratio	-
λ	consistency factor / heat of fusion	s / $\frac{J}{kg}$
ω	angular frequency	rad/s
ψ	nozzle angle according to Luo et al.	^{o}
ρ_m	density of molten material	$\frac{kg}{m^3}$
ρ_{pol}	density of polymer	$\frac{kg}{m^3}$
ρ_s	density of solid material	$\frac{kg}{m^3}$
θ	nozzle angle according to Osswald et al.	^{o}
E_a	activation energy	J/mol
k	thermal conductivity	$\frac{W}{m-K}$
k_m	thermal conductivity	$\frac{W}{m-K}$
l	molecular separation	m
L_B	length of barrel section	m
L_{cone}	length of contraction section	m
L_c	length of capillary section	m
$m(T)$	consistency index as a function of temperature	Pa-s
P	pressure	Pa
P_o	atmospheric pressure	Pa
Q	volumetric flow rate	$\frac{m^s}{s}$
r	radius	m

R	universal gas constant / rod radius	$\frac{J}{K-mol}/m$
T	temperature	K
T_b	temperature of hot surface	K
T_g	glass transition temperature	^oC - K
T_o	initial temperature	K
T_{ref}	reference temperature	K
T_s	surface temperature	K
u_s	speed of sound	m/s
v_r	velocity in the radial component	m/s
v_z	velocity in z-component	m/s
v_{sy}	velocity of solid polymer	m/s
$(b-1)$	power-law index of Carreau-Yasuda Model	-
α	nozzle angle according to Bellini et al. and Phan et al.	^{o}
α_s	thermal diffusivity	$\frac{m^2}{s}$
ΔP	pressure difference	Pa
δ	melt film thickness	m
$\dot{E}_{in}$	energy transfer from hot surface to filament material	W
$\dot{E}_s$	energy of solid material	W
ϵ	emissivity	-
η_∞	infinity-rate viscosity of Carreau-Yasuda Model	Pa-s
η_o	zero-shear viscosity of Carreau-Yasuda Model	Pa-s
μ	viscosity	Pa-s
μ_c	viscosity in capillary region	Pa-s
μ_f	viscosity in melt film region	Pa-s
σ	Stefan-Boltzmann constant	$\frac{W}{m^2K^4}$
σ_{uts}	ultimate tensile strength	Pa

τ_{rz}	shear stress	Pa
τ_{UT}	ultimate shear strength	Pa
$\vec{F_\tau}$	force due to shear stress component	N
$\vec{F_p}$	force due to pressure component	N
a	width transition of zero-shear viscosity and power-law region, Carreau-Yasuda Model	-
$A_{contact}$	contact area	m^2
A_o	area of filament inside the nozzle	m^2
$a_{T-Arrhenius}$	Arrhenius shift factor	-
a_{T-WLF}	Williams-Landel-Ferry (WLF) shift factor	-
a_T	shift factor	-
C_1	WLF constant	-
C_2	WLF constant	K
c_p	specific heat	$\frac{J}{kg-K}$
C_s	specific heat	$\frac{J}{kg-K}$
D_B	barrel diameter	m
D_c	capillary diameter	m
F_N	rod force	N
F_{sz}	filament force	N
Hz	hertz	1/s
$K(T)$	consistency index	Pa-s
L	nozzle length	m
m_c	consistency index of capillary region	Pa-s
n	power-law index	-
p	filament pressure	Pa
p_i	capillary pressure	Pa

R_i^*	tilted capillary radius	m
R_i	capillary radius	m
R_o^*	tilted filament radius	m
R_o	filament radius	m
T_{eff}	effective temperature	K
T_h	heater temperature	K
T_{if}	filament initial temperature	K
T_L	Liquid temperature	K
T_{room}	room temperature	K
T_S	Solid temperature	K
U_o	melt velocity	m/s
U_{sz}	filament velocity	m/s
V_o	volume of filament inside of nozzle	m^3
${}_2F_1$	hypergeometric function	-

Table of Contents

List of Figures

List of Tables

1. Introduction

Fused Filament Fabrication (FFF) has been at the forefront of Additive Manufacturing (AM) due to the low cost of machines and materials and the ability to manufacture complex geometries. It is also popular among users due to the broad availability of AM machines in the market. In addition, the FFF process has gained popularity in the last decade due to design freedom from fabricating complex geometries previously unattainable. During an FFF process, a filament is fed towards a heated nozzle. Inside the nozzle, the material is melted and extruded. During the material extrusion, neighboring beads are together in a diffusion dominant welding process [2]. This process is repeated layer by layer until the object is entirely manufactured, as depicted in Figure 1.1.

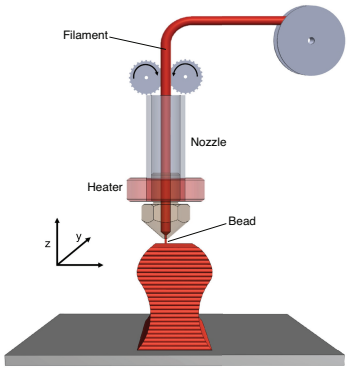

Figure 1.1: Schematic of a FFF process.

Because the building process requires a layer by layer structure, the time required to print an object increases with decreasing nozzle diameter and layer height [3]. Therefore, many parameters have been studied to understand the FFF process fully. These range from filler orientation during process [4, 5] and effect of printing speed [6] to solidification of layers [7], and the mechanical properties arising from the printing orientation [8, 9]. When talking about the printing speed of the FFF process, it is necessary to understand the melting mechanism to use the machine at its fullest potential. To obtain a successful print, it is required to raise the temperature of the filament material to the melt state and extrude the material to form the desired part. However, as the printing rate increases, it is crucial to have melted material to print. If no material is being extruded, the resulting print would be

a defective part. This means that parts could be produced at a higher rate while maintaining their structural properties if the melting inside the nozzle is understood.

This work aims to understand the FFF process's melting mechanism by predicting the filament force and filament velocity using an improved analytical model. In addition, a study was performed to understand the experimental threshold of the melting temperature for thermoplastics polymers. Moreover, a study was done to understand the effect of process parameters on the experimental results and compare this with the different melting models.

Chapter two summarizes and discusses the state-of-the-art in the field of the FFF process. In particular, it discusses previous models analyzing the melting process and the prediction of filament velocity. For decades, a significant challenge in this process has been understanding and forecasting the printing speed of these machines. Hence, a fundamental part of this work proposal involves improving the melting models available in the present. In particular, the FFF melting model proposed by Osswald et al. [1] uses the concept of the pressure-induced melt removal process as its core.

The third chapter, a theoretical background, provides the basic knowledge necessary to understand the work presented here.

Chapter four focuses on understanding the base assumption of the pressured-induced melt removal process developed by Stammers and Beek [10], the backbone of the Osswald et al. model [1]. Experimental results were acquired and compared with analytical solutions and numerical simulations. Computed tomography technology was employed to visualize the melt film formation. An understanding of the melting temperature for amorphous materials was achieved. A distinguished transition on viscosity was observed for the amorphous materials suggesting that the melting temperature equals the glass transition temperature. Good prediction between all the methods was achieved. Results give insights into the melting phenomena of materials during the fused filament fabrication process.

Chapter five shows an improvement performed to the Osswald et al. model [1]. The model is improved by taking into account the shear-thinning behavior of the polymer material by including the power-law model as the viscosity model. This model will be called the Osswald-Colon model. Equations, model assumptions, and considerations are explained in detail. A customized setup has been built, consisting of the essential components to extrude to be used inside a computed tomography system. The model shows good agreement with experimental results assuming that the melting temperature of both amorphous and semi-crystalline materials equal the glass transition temperature. For the semi-crystalline material, a comparison was made using the glass transition temperature and melting temperature. Moreover, a radiation heat transfer analysis was performed to account for the heating from the heated walls to the filament material.

Chapter six studies the radiation heat transfer and nozzle diameter on a range of melting models. The radiation heat transfer was implemented to both the Osswald et al. model and the Osswald-Colon model. The radiation approach calculates the initial temperature of the filament as a function of filament velocity. Later, the melt film thickness is calculated and input into both melting models. The models are compared with experimental data obtained from a customized FFF machine. The data processed allowing the understanding of the critical force where slippage occurs. It was shown that the slippage would be dependent

on the material properties and not the printing parameters. A good prediction was made when calculating the theoretical, critical force. It was shown the Osswald-Colon model approximates the best for the ABS data. However, this is not true when predicting the PLA data under the assumption of using the actual melting temperature (not the glass transition temperature). The results give insight into what models best describe the FFF process for a range of materials, nozzle diameters, and process temperature.

Chapter seven details a research plan for future work. A suggested setup is presented to visualize the density difference between solid and melted material on a FFF machine during extrusion. It is proposed to use a different boundary condition on the Osswald et al. model and Osswald-Colon model, which considers the velocity component in the r-direction. Also, it is suggested that experiments should be done to determine the contact area between the feeding mechanism and filament material for a range of FFF machines. This will allow for the determination of the critical force, which provides how fast the filament can be extruded.

2. State of the Art

Fused Filament Fabrication (FFF) has been at the forefront of Additive Manufacturing (AM). This process requires low-cost machines and can manufacture complex geometries that common manufacturing techniques cannot manufacture. It is also popular among users due to the broad availability of AM machines in the market. During an FFF process, a filament is fed towards a heated nozzle. Inside the nozzle, the material is melted and extruded. During the material extrusion, neighboring beads are joined in a diffusion dominant welding process [2]. This process is repeated layer by layer until the object is fully manufactured. Because the building process requires a layer by layer structure, the time required to print an object increases with decreasing nozzle diameter and layer height [3]. Many parameters have been studied to understand the FFF process fully. Some of these are the filament diameter dependence [11], filler orientation during process [4, 5], micro-structure of FFF parts using different types of methods [12], surface quality [13, 14], effect of printing speed [6], bonding strength between beads [15], printing parameters [16, 17], solidification of layers [7] and the mechanical properties arising from the printing orientation [8, 9] to name a few.

When talking about the printing speed of the FFF process, it is necessary to understand the melting mechanism to use the machine at its fullest potential. To obtain a successful print, it is essential to raise the temperature of the filament material to the melt state and extrude the material to form the desired part. However, as the printing rate increases, it is vital to have melted material to print the part. If no material is being extruded, the resulting print would be a defective part. This means that parts could be produced at a higher rate while maintaining their structural properties if the melting inside the nozzle is understood.

Various models have been proposed to explain the melting behavior of the polymer film. One of the first models developed to predict the force necessary to successfully print was presented by Bellini et al. [18]. Bellini et al. assumed that melting of the filament material occurs right after the material enters the nozzle. During the process, the solid filament acts as a plunger to push the melted polymer through the nozzle generating the bead. This assumption has been used widely by many [19–21]. However, this model only works when using low printing speeds. Since the material is heated as it moves downwards towards the nozzle, low filament speeds allow the material to melt [19] fully.

For this reason, the model does not work for high printing speeds. The model proposed by Luo et al. [22] takes a heat transfer approach by solving a Graetz-Nusselt problem. Their work focuses on the boundary between the solid and molten polymer in the heated portion of the nozzle channel. Here, the solution is an upper bound estimate and also a semi-empirical

model as the threshold temperature is measured. The model is capable of predicting at low printing speeds up to 1.5 mm/s. Both models need two parameters to predict the printing process. These are the filament speed and the filament force. Due to the technological advancements, other authors have taken the task to measure the filament force accurately, and velocity during printing [6, 23–26]. By incorporating a force sensor, the pressure can be measured in real-time. Also, by combining an encoder, the velocity at which the filament is fed can be measured. Results have shown that it is possible to print at filament velocities higher than three mm/s. However, once it reaches a specific rate, a phenomenon prevents the machine from printing at the desired speed. This is attributed to not having enough melted material, which creates wear and slippage of the filament [25, 26]. For this reason, it is essential to understand the melting mechanism to predict the FFF process at higher printing rates.

Recently, a new approach has been developed to explain the melting behavior of the filament in a FFF process. This approach, known as the "Fused Filament Fabrication Melting Model" was proposed by Osswald et al. [1] in 2018. This model incorporates the formation of a melt thickness that varies as a function of the force exerted by the solid filament. During the derivation of the model, a Newtonian viscosity was assumed to simplify the actual rheological behavior of polymeric melts. Current results are promising. However, many simplifications were made during its derivation. One such simplification is the use of a constant viscosity which neglects the shear-thinning behavior of polymers. During the comparison of results, the authors used a Power-Law viscosity model. Furthermore, they used an iterative process where the velocity calculated was used to calculate the viscosity at the given moment.

It is thought that the model proposed by Osswald et al. [1] has the potential of describing the melting of polymer material at higher filament speeds. The backbone of this thought is that the authors used the concept of pressure-induced melt removal developed by Stammers [10]. An analogy to this concept is the melting of butter in a hot pan. By feeding a polymer vertically, in this case towards a hot surface, a melt film is created between the heated surface and the solid material. This film is a function of the velocity or force you feed the material and the surface temperature. The same thing is believed to happen during an FFF process. Most commercial printing nozzles possess a significant short nozzle length, approximately 10 mm, which is not enough to fully melt the material before reaching the end of the nozzle. This means that the material does not reach its melting temperature. Still, the filament's temperature before it makes contact with the hot end is higher than the ambient temperature. This temperature increase happens due to the heat transfer from the heated walls to the filament, assuming there is no contact between the filament and heated wall when traveling downwards. When the filament reaches the bottom of the heating nozzle, a melt film is created. This melt film is later pushed to the capillary section of the nozzle and extruded. The assumption that there is no contact between the heater walls and the filament is an oversimplification because the filament diameter is smaller than the nozzle diameter, so a gap between the two should exist. Nonetheless, this assumption makes for a good first approximation.

The work presented in this document is based on the assumption that a melt film is created when the filament makes contact with the bottom of the nozzle. This work pro-

poses studying and understanding the melting in an FFF process for amorphous and semi-crystalline materials. Understanding the melting mechanisms during this process is essential to model the mechanism of the FFF process. It is also necessary to understand the solid-liquid interface during the process [27–29]. A pressure-induced melt removal process was performed to understand the creation of a melt film during the material's melting.

The FFF model derived by Osswald et al. [1] was improved upon by adding the shear-thinning effect of thermoplastic materials. The shear-thinning effect was implemented by using the power-law model during derivation. The improved model was validated by comparing with experimental data obtained with a customized FFF machine having a force sensor and an encoder. These were useful to compare the observed filament velocity and filament force with the different viscosity models.

Moreover, a study was performed to study the effect of radiation heat transfer and nozzle geometry on the FFF models. Radiation from the heated walls of the nozzle to the filament material increases the initial filament temperature. The filament temperature was calculated as it affects the melt film thickness. A range of FFF models were used and compared with the improved Osswald et al. model. The study examines what models best describe the melting and rate mechanisms of the FFF process for a range of printing conditions.

The procedures, materials, and results for each of these three studies are shown and described in Chapters 4 - 6 respectively.

3. Background

3.1 Polymer Structures

Amorphous polymers possess a randomly arranged molecular structure. Due to their network, amorphous thermoplastics are characterized by the length of their -C-C bond. The majority of amorphous thermoplastics tend to have a clear appearance because the -C-C bond is smaller than the wavelength of visible light. As the temperature is decreased, the amorphous material behaves as an elastic solid. When the temperature is increased, the modulus is negligible, and the material enters the viscoelastic region where it can flow. This transition between the elastic and viscoelastic region happens when the polymer reaches the glass transition temperature (T_g). The glass transition temperature of an amorphous polymer can also be affected by pressure. As pressure increases, a higher temperature is needed to slide polymer chains past one another. As a result, the glass transition temperature increases.

Contrary to amorphous thermoplastics, in semi-crystalline thermoplastics, the molecules are aligned in an ordered crystal structure. The characteristic size of semi-crystalline thermoplastics vary between 50 - 500 μm [30]. Due to this size, semi-crystalline polymers are translucent and not transparent. Semi-crystalline materials are not perfectly crystalline as metals are; they possess random and oriented crystal structures. The balance between the random and oriented structure is affected by the cooling rate. Compared to amorphous thermoplastic, semi-crystalline thermoplastics do not gradually soften with an increase in temperature [31]. Instead of softening, they remain solid until the melting temperature is reached.

3.2 Generalized Newtonian Fluids

Generalized Newtonian fluids are characterized by viscosity dependence on shear rate and time history. Compared to Newtonian fluids, there is a non-linear relationship between the stress and shear rate. The disentanglement of the molecule chains causes this non-linearity during flow. The molecules are highly entangled at low deformation rates, while at higher deformation rates, the molecules are stretched out and disentangled. This makes it easier for the molecules to slide past one another [30, 32, 33]. The materials used in this work are known as pseudoplastic materials or shear-thinning materials. These are characterized

by decreasing viscosity with increasing shear rate. To measure the viscosity of materials, different methods are available. Primarily these are done under shear rate and frequency. The effect of temperature needs to be accounted for since the viscosity is a function of temperature. To model the viscosity as a function of temperature and shear rate, rheological models are necessary. The methods and rheological models used in this work are presented next.

3.3 The Cox-Merz Rule

Polymer fluids can be characterized by steady shear and dynamics measurements. For this reason, a way to relate these two methods is essential. The Cox-Merz rule [34] (shown in Equation 4.3) is an empirical rule that states that the dependence of the steady shear viscosity on the shear rate can be determined from the dynamic viscosity as a function of frequency as the two resulting curves are approximately identical.

$$|\eta^*(w)| = \eta(\dot{\gamma} = w) \tag{3.1}$$

3.4 Time-Temperature Superposition Principle

The time-temperature superposition principle relates time to temperature for viscoelastic materials. Since some experimental methods have a limited time scale, it is possible to describe different temperatures to create a master curve at a reference temperature. A temperature variation corresponds to a shift in the time scale when determining relaxation times and viscosities for polymer melts [33]. Two commonly used models to calculate this shift are available and will depend on the material's structure. These models are the Arrhenius shift factor (Equation 3.2) and the WilliamsLandelFerry (WLF) shift factor (Equation 3.3) for semi-crystalline and amorphous polymer, respectively.

$$\ln a_{T-Arrhenius} = \frac{-E_a}{R}\Big(\frac{1}{T_{ref}} - \frac{1}{T}\Big) \tag{3.2}$$

$$\log a_{T-WLF} = \frac{-C_1(T - T_{ref})}{C_2 + (T - T_{ref}))} \tag{3.3}$$

where E_a is the activation energy, R is the universal gas constants, and C_1 and C_2 are constants. The shift factor can also be expressed as shown in Equation 3.4.

$$a_T = \frac{\eta_o(T)}{\eta_o(T_{ref})} \tag{3.4}$$

Where $\eta_o(T_{ref})$ is the viscosity at the reference temperature and $\eta_o(T)$ is the temperature at the corresponding processing temperature.

3.5 Viscosity Models

3.5.1 Power Law Model

The simplest model capable of describing the shear-thinning behavior of thermoplastic materials is the power-law model proposed by Ostwald [35], and Waele [36]. The model describes the viscosity as a function of temperature and shear rate as shown in Equation 3.5.

$$\eta = m(T)\dot{\gamma}^{n-1} = m\left|\frac{\partial v}{\partial z}\right|^{n-1} \tag{3.5}$$

Where m is the consistency index, n is the power-law index, and $\dot{\gamma}$ is the shear rate. In some cases, the consistency index can include a temperature dependence in the viscosity term as presented in Equation 3.6. The power-law index determines the class of the fluid. A power law index (n) of 1 indicates a Newtonian fluid, $n > 1$ indicates a shear-thickening fluid, and $n < 1$ a shear-thinning liquid. These variables are material-dependent.

$$m(T) = m_o e^{-a(T-T_o)} \tag{3.6}$$

This model, compared to others, is easy to implement in phenomenological equations. However, the modeled viscosity range over-predicts the viscosity at low deformations (low shear rates).

3.5.2 Carreau-Yasuda Model

Compared to the power-law model, the Carreau-Yasuda model can predict the viscosity at low and higher shear rates. The viscosity model is shown in Equation 4.4.

$$\frac{\eta - \eta_\infty}{\eta_o - \eta_\infty} = (1 + (\lambda\dot{\gamma})^a)^{\frac{b-1}{a}} \tag{3.7}$$

Where η_o is the zero-shear viscosity and η_∞, is the infinite-rate viscosity. The parameter λ is the consistency factor and has units of time, where $1/\lambda$ is the critical shear rate at which the viscosity decreases. The power-law index is expressed as $(b-1)$ and a represents the width of the transition region between the zero-shear viscosity and the power-law region. Since pseudo-plastics rarely reach the infinite shear viscosity, this parameter can be assumed to be zero. At higher shear viscosities, near infinity, the Carreau-Yasuda model approximates the power-law model.

3.6 Thermal Conductivity

The thermal conductivity, k, is most often used to quantify heat transfer through a polymer material. By definition, energy is transported proportional to the speed of sound [32]. This allows thermal conductivity to be expressed in terms of the speed of sound as shown in Equation 3.8.

$$k = c_p \rho_{pol} u_s l \tag{3.8}$$

Where u_s is the speed of sound, ρ_{pol} is the density of the polymer at a given temperature, l is the molecular separation, and C_p is the specific heat. Compared to metals, where the thermal conductivity remains constant over a range of temperatures, amorphous polymers show that the thermal conductivity increases with increasing temperature until the glass transition temperature, T_g. Above the glass transition temperature, the thermal conductivity decreases with increasing temperature. For semi-crystalline thermoplastics, the thermal conductivity is higher in the solid state compared to the molten state.

Anisotropy in polymers plays a role in thermal conductivity. Polymers with a high degree of orientation, like semi-crystalline polymers, have much higher thermal conductivity than amorphous polymers due to the direction of the polymeric chains. When a polymer is mixed with an inorganic filler, the thermal conductivity of the matrix material usually increases. However, the thermal conductivity around the melting temperature can decrease for semi-crystalline polymers.

Compared to metals, polymers possess significantly lower thermal conductivity. This difference in magnitude, between 0 to 1 $\frac{W}{mK}$ for most polymers and 5 to 300 $\frac{W}{mK}$ for metals, is due to the separation between the atoms that comprise each material. For metals, the separation between atoms is lower due to the inter-metallic bonding than polymers, where the distance of Van-der-Waals bonding is greater. As a result, energy is transferred more easily through metals than through polymers.

3.7 Glass Transition and Melting Temperature

The glass transition temperature is one of the essential properties in the manufacturing of polymers. The glass transition temperature is when the materials transition from the rigid solid state to a soft, more pliable material. During this transition, the material is allowed to flow due to an applied deformation or stress. The ASTM E1356 standard is used to measure this property, which requires Differential Scanning Calorimetry (DSC). When mixing two incompatible polymers, two glass transition temperatures are visible when measuring the elastic modulus of the blend [32].

The melting temperature (T_m) is the highest temperature at which the crystalline structure can exist. The polymer is considered a viscoelastic liquid beyond this temperature. It has been noted that the ratio between T_g and T_m is often 2/3, as shown in Equation 3.9 [32]

$$\frac{T_g}{T_m} \approx \frac{2}{3} \tag{3.9}$$

where the temperatures, T_g and T_m, are expressed in Kelvin.

3.8 Specific Heat and Heat of Fusion

The specific heat, C_s, represents the energy required to change the temperature of a unit mass of material by one degree [37]. This energy can be measured at constant pressure or volume. The specific heat at constant pressure includes the effect of volumetric change. It is more significant than at constant volume. However, one can assume that both are the same.

The specific heat of fusion (λ) is the energy needed to convert one gram of 100 % crystalline solid into molten liquid at a temperature T [38]. The heat of fusion is observed as a discontinuity in the specific heat at the melting point. This discontinuity includes the heat required to melt the crystallites [37]. These properties are seen in semi-crystalline material due to its molecular structure. For an amorphous material, no heat of fusion is required.

3.9 Solid and Melt Density

For a polymer, density is defined as the ratio of molar mass and molar volume as shown in Equation 3.10.

$$\rho = \frac{M}{V_m} \tag{3.10}$$

As mentioned earlier, a polymer can have a wide range of structures. The crystalline state is associated with a regular arrangement of chain molecules. These chains can be aligned parallel to each other or can twist on themselves to form crystallites. For a crystalline polymer, the volume can be approximated to 1.4 times its van der Waals volume ($V_{cr} = 1.43V_w$). For an amorphous polymer it is $V_{cr} = 1.60V_w$. Many properties are directly connected with density. Since molar volume is easy to measure, the density of polymers is available at standard conditions, which include the effect of temperature [39].

Due to the branching of the molecules in a semi-crystalline polymer, chains are packed together more efficiently and tightly than an amorphous material. For this reason, the density of a semi-crystalline material (ρ_c) is higher than an amorphous (ρ_a) [40] material.

Melt density corresponds to the density of the polymer in a melt-liquid state. Since the properties of a polymer are highly influenced by the temperature, its density in a melt state is different than at ambient temperature. At high temperatures, the molecule chains will expand and separate. However, finding the melt density is difficult since data is rarely published in material datasheets. However, as a general guideline, the melt density can be approximated as 90 % of the solid density for an amorphous polymer, and 80 % for a semi-crystalline polymer [41]. Actual melt density values will vary by material types, grades, temperature, and pressure applied to each material.

3.10 Melting with Pressure Flow Removal

Stammers and Beek developed the melting with pressure flow removal model [10] to describe an approximate theoretical model of the melting of material onto a hot surface. This concept is the main idea behind the derivation of the melting model in an FFF process which was developed by Osswald et al. [1]. In this process, a material is pressed into a hot surface. The melt is removed by the squeezing flow of the solid material on the melt by applying a force. This force is the dominant rate-controlling variable of this process.

Consider a polymer rod of radius R pressed by a forced F_N against a hot surface of the same radius with constant temperature T_s as shown in Figure 4.5. A melt film is formed that is being squeezed out by radial flow. To solve this problem, the following simplified assumptions were made:

1. The solid is rigid and moves with constant velocity towards the hot surface.
2. The film between the solid polymer and the hot surface has a constant thickness, δ.
3. Film flow is laminar.
4. The fluid is Newtonian.
5. Temperature independent viscosity.
6. Constant thermophysical properties.
7. Steady-state condition.
8. Negligible gravitational forces.
9. Negligible convection and viscous dissipation on the film.

Some of these assumptions lead to an oversimplification of the solution. However, these assumptions allow the "construction" of a simple model for the process, enabling insights into the nature of the process.

With the rigid polymer assumption, the total mass flow rate of melting of the solid polymer ($\dot{m}_s$) can immediately be written as shown in Equation 3.11.

$$\dot{m}_s = \pi(-v_{sy})\rho_s R^2 \tag{3.11}$$

where $v_{sy} < 0$ is the velocity of the solid polymer. The goal is to find a relationship between the velocity, the processing conditions, and the material's physical properties. By pressing the rod against the plate, a radial velocity profile will be induced in the melt film. This flow removes the newly melted polymer from the location of melting and drains it. The mean radial velocity ($\bar{v}_r$) at any location r can be expressed in terms of the velocity v_{sy} by performing a mass-balance analysis as shown in Equation 3.12.

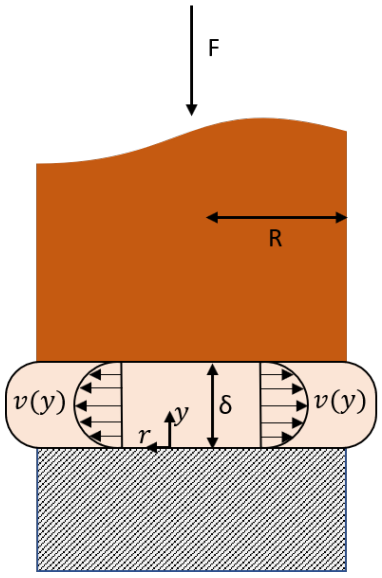

Figure 3.1: Schematic of a pressure-induced melt removal of a solid polymer.

$$(-v_{sy})\rho_s \pi r^2 = 2\pi r \delta \bar{v}_r \rho_m \tag{3.12}$$

where δ is the local separation between the interface and the plate. The mean radial velocity in Equation 3.12 with $\hat{\rho} = \rho_s/\rho_m$ is given by Equation 3.13.

$$\bar{v}_r = \frac{r(-v_{sy})\hat{\rho}}{2\delta} = \frac{1}{\delta}\int_0^{\delta} v_r dy \tag{3.13}$$

Where the radial component of the equation of motion reduces to Equation 3.14.

$$\frac{dP}{dr} = \mu \frac{d^2 v_r}{dy^2} \tag{3.14}$$

Equation 3.14 is integrated over y, with boundary conditions $v_r(0) = 0$ and $v_r(\delta) = 0$, giving Equation 3.15.

$$v_r = \frac{1}{2\mu}\frac{dP}{dr}(y - \delta)y \tag{3.15}$$

To obtain an expression for the pressure gradient $\frac{dP}{dr}$ versus the radial position r, Equation 3.15 is substituted into Equation 3.13.

$$-\left(\frac{dP}{dr}\right) = \frac{6\mu(-v_{sy})r\hat{\rho}}{\delta^3} \tag{3.16}$$

Integrating Equation 3.16 with boundary condition $P(R) = P_o$, where P_o is atmospheric pressure, leads to the pressure profile shown in Equation 3.17.

$$P(r) - P_o = \frac{3\mu(-v_{sy})\hat{\rho}}{\delta^3}(R^2 - r^2) \tag{3.17}$$

The total force F_N is calculated by integrating over the area of the rod as shown in Equation 3.18.

$$F_N = \int_0^R 2\pi r P(r) dr = \pi R^2 P_o + \Big(\frac{3\mu\pi(-v_{sy})\hat{\rho}R^4}{2\delta^3}\Big) \tag{3.18}$$

Rearranging Equation 3.18 to get a relationship between v_{sy} in terms of the external total force F_N gives Equation 3.19.

$$(-v_{sy}) = \frac{2\delta^3(F_N - \pi R^2 P_o)}{3\mu\pi\hat{\rho}R^4} \tag{3.19}$$

The velocity of the solid polymer cannot be calculated since the value δ is still unknown. This value is determined by performing an energy balance in the solid-melt interface as shown in Equation 3.20. This equation is known as the Stefan Condition, and it will be explained in more detail in the mathematical model section of this thesis.

$$k_m\Big(\frac{T_b - T_m}{\delta}\Big) = \rho_s(-v_{sy})[\lambda + C_s(T_m - T_o)] \tag{3.20}$$

Where T_o is the initial temperature of the solid, T_b is the temperature of the hot surface, T_m is the melting temperature, k_m is the thermal conductivity of the melt material, ρ_s is the solid density, λ is the heat of fusion, and C_s is the specific heat of the material. Solving both Equation 3.19 and Equation 3.20 for δ results in the final expression for the rod velocity as shown in Equation 3.21.

$$(-v_{sy}) = \frac{0.6787}{R}\Big(\frac{F_N - \pi R^2 P_o}{\mu\hat{\rho}}\Big)^{1/4}\Big(\frac{k_m(T_b - T_m)}{\rho_s[\lambda + C_s(T_m - T_o)]}\Big)^{3/4} \tag{3.21}$$

The results show that the rate of melting increases with the total force, F_N, to the one-fourth power. This means that with increasing force, the film thickness is reduced, thus increasing the rate of melting [42]. However, the pressure drop that is needed to squeeze out the melt increase with decreasing film thickness.

3.11 Poiseuille Flow

Poiseuille flow, or tube flow, is encountered in several polymer processes such as extrusion dies, sprues, and runner systems inside injection molds [30]. It is also found in FFF processes, specifically in the capillary of the printing nozzle. Starting with the equations of motion, the velocity profile can be calculated using the boundary conditions at the tube walls. The velocity profile using a power-law model [43] is shown in Equation 3.22.

$$v_z(r) = \frac{R}{1+s}\Big(\frac{R\Delta P}{2mL}\Big)^s\Big[1 - \Big(\frac{r}{R}\Big)^{s+1}\Big] \tag{3.22}$$

$s = 1/n$, m is the consistency index, n is the power-law index, L is the capillary or tube length, R is the capillary radius, and ΔP is the pressure difference between the capillary entrance and exit. The volumetric flow rate is calculated using Equation 3.23.

$$Q = \left(\frac{\pi R^3}{s+3}\right)\left(\frac{R\Delta P}{2mL}\right)^s \tag{3.23}$$

3.12 X- Ray Computed Tomography

X-ray Computed Tomography (CT) is a non-destructive technique for visualizing interior features within solid objects obtaining the digital information on their geometries and properties [44]. It was the first non-invasive radiological method allowing the generation of tomographic images of every part of the human body without superimposition of adjacent structures [45]. Nowadays, it has found its way into the materials science field and many industrial applications. Using this method, the study of cracks, voids, and inclusions such as fibers and particles embedded into a matrix material is possible without damaging the studied object. This is particularly important in Industrial applications for inspecting the quality of sensitive and high constraint parts. In recent years, there has been an effort to develop monitoring techniques to allow the in-situ study of properties during a CT [46]. Compared to a digital image composed of pixels, a CT image is composed of voxels (volume elements). The gray levels in a CT image correspond to X-ray attenuation, reflecting the proportion of X-rays (scattered or absorbed) as they pass through each voxel. This attenuation is a function of X-ray energy and the density and composition of the tested material. For this reason, CT is the technique chosen to study the melting of the polymer during an FFF process.

3.12.1 Fundamentals

Tomographic imaging consists of directing X-rays at an object from multiple orientations and measuring the decrease in intensity along with a series of linear paths. This decrease, characterized by Beer's Law, describes intensity reduction as a function of X-ray energy, path length, and material linear attenuation. An algorithm is later used to reconstruct the distribution of X-ray attenuation in the volume being imaged [44]. The CT setup consists of three major components. These are an X-ray source, a detector, and a movable table capable of rotation along the z-axis between the source and detector. During a scan, an object is placed in the table and rotated 360^o at several steps. These steps are user-controlled and can increase the resolution of the scanned object. The scanning time increases with rising steps. During each stage, the sample is exposed to the X-ray that penetrates the object and is received by the detector. During the radiation, the X-rays are attenuated along the way, leading the sensor to receive a weak signal. The intensity of the attenuation is dependent on the thickness of the object, and the radiopacity (function of material density and atomic number) of the material [47]. This effect is best described by using the Beer-Lamber Law of

attenuation as shown in Equation 3.24.

$$I(x) = I_o e^{-\mu x} \tag{3.24}$$

I is the X-ray intensity behind the object, I_o is the intensity without the object, x is the length of the x-ray path through the object, and μ is the linear attenuation coefficient of the object the material for the X-ray energy employed.

3.12.2 Image Artifacts

During the scanning of an object, image imperfections or artifacts are observed and classified according to their origin. These can result due to physics-related and system-related causes. The latter includes poor calibration of detector sensitivity and time-, temperature-, or irradiation-history-dependent drift in detector sensitivity. Others can be due to inadequacies in the reconstruction algorithm, non-uniform scanning motion, or fluctuations in X-ray tube voltage.

Physics-related causes involve quantum noise, X-ray scattering, beam hardening, and nonlinear partial volume effects. These are explained in further detail below [45]:

- Quantum noise: Physical unavoidable statistical fluctuations in the x-ray beam intensity will show up as signal-dependent noise in the projection data. A reduction of the noise level requires an increase in x-ray intensity or data acquisition time, along with an increase in patient dose. The signal dependency of the quantum noise leads to typical radial noise structures in the reconstructed images.

- X-ray scattering: In fan beam type systems, it is possible to use detectors that are sufficiently collimating to reduce the effect of scattering adequately. In sensor ring-based systems, however, mathematical scatter models have to be used to correct this effect.

- Beam hardening: It is the phenomenon occurring when an x-ray beam comprised of polychromatic energies passes through an object, resulting in selective attenuation of lower energy photons [48]. Simple empirical corrections are usually sufficient to compensate for this effect.

- Nonlinear partial volume effects: As a consequence of the exponential, thus nonlinear, attenuation of radiation when high-contrast structures are immersed only partially in the imaged slice, the measured data becomes inconsistent with the mathematical model used for reconstruction. This can be reduced by reducing the slice thickness.

3.13 Existing FFF Melting Models

Currently, there exist many models to predict the melting rate during the FFF process. These models are distinct and involve using viscoelastic and thermal properties and mechanical

properties of the materials used for the extrusion. Figure 3.2 shows a schematic of the hot-end. The image will be a reference when talking about the different FFF models. Bellow are standard FFF models used in the literature, and that will be compared to the work presented here.

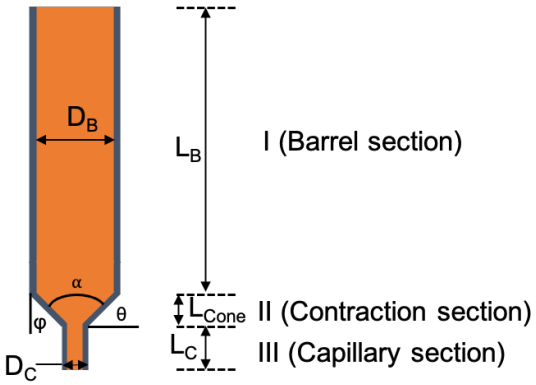

Figure 3.2: Schematic of a pressure-induced melt removal of a solid polymer.

3.13.1 Bellini et. al Model

The FFF model proposed by Bellini et al. [18] assumes that the material inside the nozzle is in a melt state. In the analytical model, the feeding force F relates the pressure drop ΔP through the hot-end as shown in equation 6.1.

$$F = \Delta P A_F \tag{3.25}$$

Where A_F is the cross-sectional areal of the filament material, the pressure drop through the hot-end is approximated by the sum of the pressure drops through the different sections of the nozzle as shown in Figure 3.2. For the Bellini et., al model [18], the total pressure drop is described by equation 6.2.

$$\Delta P = \Delta P_{barrel} + \Delta P_{cone} + \Delta P_{capillary} \tag{3.26}$$

where ΔP_{barrel}, ΔP_{cone}, and $\Delta P_{capillary}$ are the pressure drop in the barrel, contraction, and capillary respectively and are shown in Equation 6.3 - 6.5.

$$\Delta P_{barrel} = K(T)\Big[\frac{1+3n}{4n}\frac{32Q}{\pi D_B^3}\Big]^n \frac{4L_B}{D_B} \tag{3.27}$$

$$\Delta P_{contraction} = K(T)\Big[\frac{1+3n}{4n}\frac{32Q}{\pi}\Big]^n \Big(\frac{1}{D_C^{3n}} - \frac{1}{D_B^{3n}}\Big)\frac{2}{3n * tan(\frac{\alpha}{2})} \tag{3.28}$$

$$\Delta P_{capillary} = K(T)\Big[\frac{1+3n}{4n}\frac{32Q}{\pi D_C^3}\Big]^n \frac{4L_C}{D_C} \tag{3.29}$$

where $Q = VA_F$. Here, V is the filament velocity, L_B is the barrel length, D_B is the barrel diameter, L_C is the capillary length, D_C is the capillary diameter, $K(T)$ is the consistency index as a function of the temperature, n is the power-law index of the material, and α is the angle of the nozzle. To calculate the consistency index for a range of temperatures, the time-temperature superposition principle is used.

3.13.2 Phan et al. Model

Phan et al. [49] use a similar approach as Bellini et al. [18]. However, Phan et al. model the pressure drop in the conical region by modifying the Cogswell model [50]. The model uses both shear viscosity (η) and elongational viscosity (η_e). Power-law relations govern both viscosities under the generalized Newtonian fluid (GNF) framework. Here, m and L are the consistency index for the shear and elongational viscosity. For the Phan et al. model, the total pressure drop is described by equation 6.6.

$$\Delta P = \Delta P_\alpha + \Delta P_o + \Delta P_{capillary} \tag{3.30}$$

Where ΔP_α, ΔP_o, and $\Delta P_{capillary}$ are the pressure drop in the truncated cone region, reorganization of the melt from the converging area into the capillary, and capillary respectively and are shown in Equation 6.7 - 6.8. The $\Delta P_{capillary}$ has the same expression as in the Bellini et al. model.

$$\Delta P_\alpha = K(T)\Big[\frac{1+3n}{4n}\frac{32Q}{\pi D_C^3}\Big]^n \frac{2}{3n * tan(\frac{\alpha}{2})} + L\frac{2^{1-m}}{3m} tan\Big(\frac{\alpha}{2}\Big)^m \Big(\frac{32Q}{\pi D_C^3}\Big)^m \tag{3.31}$$

$$\Delta P_o = K(T)\Big[\frac{1+3n}{4n}\frac{32Q}{\pi D_C^3}\Big]^n \frac{1.18}{n^{0.7}} \tag{3.32}$$

Both Bellini et al. and Phan et al. models assume a fully developed laminar flow inside the hot end channel with a uniform Temperature T equal to the heater temperature. Equation 6.7 includes both the shear and extensional consistency indexes. Here, it is assumed that both power-law indexes are equal and the Trouton ratio (ratio of extensional viscosity to shear viscosity) $Tr = L/K = 5$, similar as Phan et al. [49]. Phan et al. also neglect the wall shear stress contribution in the barrel section due to its supposedly low shear rates.

3.13.3 Luo et al. Model

The model proposed by Luo et al. [22] is an upper-bound estimate and takes a heat transfer approach by solving a Graetz-Nusselt problem. Their work focuses on the boundary between the solid and molten polymer in the heated portion of the tube. Here, the solution is an upper bound estimate and also a semi-empirical model as the threshold temperature is measured. For Luo et al. model, the total force is described by equation 6.9.

$$F = (\pi R_B^2)(\Delta P_1 + \Delta P_2 + \Delta P_3 + \Delta P_4 + \Delta P_5) \tag{3.33}$$

where ΔP_1 is the pressure drop of the solid portion of the filament, ΔP_2 is the pressure drop of the melt inside the cylindrical tube, ΔP_3 is the pressure drop of the melt inside the conical tube, and ΔP_5 is the pressure drop of the melt inside the print nozzle. ΔP_4 is used to represent the pressure drop from the conical tube to the print nozzle. The pressure drop for each section are shown in equation 6.10 - 6.13.

$$\Delta P_2 = 2\mu_c\Big[(L_B - Z_s L)\Big(\frac{(N+2)U}{R_B^N}\Big)^n\Big] \tag{3.34}$$

$$\Delta P_3 = \frac{2\mu_c}{3n * sin\phi}\Big[\frac{3(3n+1)UR_B^2 sin\phi}{4n(1-cos\phi)^2(1+2cos\phi)}\Big]^n\Big(\frac{1}{R_B^{3n}} - \frac{1}{R_C^{3n}}\Big) \tag{3.35}$$

$$\Delta P_4 = \mu_c\Big(\frac{3n+1}{n}\frac{UR_B^2}{R_C^3}\Big)^n\frac{1.18}{n^{0.7}} \tag{3.36}$$

$$\Delta P_5 = 2\mu_c L_C\Big(\frac{(N+2)U}{R_C^N}\Big)^n \tag{3.37}$$

where $N = (1 + \frac{1}{n})$, n is the power-law index, Z_s is the percentage of the solid portion in the filament, $L = L_B + L_{cone}$, μ_c is the constant viscosity, and U is the filament velocity. In this work, we assumed that the viscosity varies with temperature and will be equal with $\mu_c = K(T)$ where $K(T)$ is the consistency index as a function of temperature. According to Luo et al., for small Z_s, it implies that only a small portion of the filament is solid inside the nozzle. Subsequently, ΔP_1 and $Z_s L$ can be neglected. Regrouping the terms, the expression for the force results in equation 6.14.

$$F = \pi R_B^2\Big[2K(T)L_B\Big(\frac{N+2}{R_B^N}\Big)^n + \frac{2K(T)}{3n * sin\phi}\Big(\frac{3(3n+1)R_B^2 sin\phi}{4n(1-cos\phi)^2(1+2cos\phi)}\Big)^n * \Big(\frac{1}{R_C^{3n}} - \frac{1}{R_B^{3n}}\Big) + K(T)\Big(\frac{3n+1}{n}\frac{R_B^2}{R_C^3}\Big)^n\frac{1.18}{n^{0.7}} + 2K(T)L_C\Big(\frac{N+2}{R_C^N}\Big)^n\Big]U^N \tag{3.38a}$$

3.13.4 Osswald et al. Model

Last, the model proposed by Osswald et al. [1], also known as the fused filament fabrication melting model, assumes that a melt film is created at the contraction surface and flows parallel to the conic surface towards the capillary region. Here the authors used the pressure-induced melt removal process as a baseline for their model. The melt film thickness is assumed to be uniform and is calculated using the Stefan Condition as shown in equation 6.15.

$$\delta = \frac{k(T_h - T_m)}{\rho_s U_{sz}[\lambda + C_s(T_m - T_o)]} \tag{3.39}$$

Where T_h is the heater temperature, T_m is the melting temperature of the filament, T_o is the initial temperature of the filament, k is the thermal conductivity of the filament, ρ_s

is the density of the solid filament, λ is the heat of fusion of the filament, C_s is the specific heat, and U_{sz} is the filament velocity. The model relates the feeding force and the filament velocity as shown in equation 6.16.

$$F = -\frac{6\pi\mu_f U_{sz}\frac{\rho_s}{\rho_m}R_B^4}{\delta^3 cos\theta}\Big[ln(\frac{R_C}{R_B}) + \frac{3}{4} + \frac{1}{4}(\frac{R_C}{R_B})^4 - (\frac{R_C}{R_B})^2\Big] + 8\pi\mu_c U_{sz}\frac{\rho_s}{\rho_m}L_C\Big[(\frac{R_B}{R_C})^4 - (\frac{R_B}{R_C})^2\Big] \quad (3.40a)$$

μ_f is the viscosity in the melt film area, μ_c is the viscosity in the capillary region, ρ_m is the molten filament density, and α is the nozzle angle. The Osswald et al. model is the baseline for the work presented in this document. Improvements and verifications will be made to ensure the validity of assumptions and accuracy of the model.

4. Understanding Melting of Amorphous Polymers

The work explores the fundamentals of the melting process for amorphous materials expanding on the work presented by Stammers and Beek [10]. The pressure-induced melt removal process is studied in detail. The process, although fundamental, allows for an understanding of the melting process during the fused filament fabrication (FFF) process. Experimental results were analyzed using state-of-the-art equipment. A total of four materials were tested. PVC and PC are amorphous materials, and PA6 and PP are semi-crystalline materials. A setup was built to allow the application of a constant force. The resulting melt film was analyzed using computed tomography technology. The experimental results were compared with numerical simulation results originating from COMSOL Multiphysics and the analytical solution derived by Stammers and Beek. Rheological and thermo-mechanical tests were used to find the softening temperature of amorphous materials. Results showed a straightforward transition for the melting temperature for both amorphous and semi-crystalline materials. It is suggested that for amorphous materials, the glass transition temperature can be used as the melting temperature ($T_m = T_g$). When comparing all three results (experimental, analytical, and numerical), values are within the same range and magnitude. A good approximation was achieved for PA6 and PVC, which have semi-crystalline and amorphous structures, respectively. Result give insights into the melting process and melting mechanisms during the extrusion of materials in the fused filament fabrication process.

4.1 Introduction

The FFF process has gained popularity in the last decade due to the expiration of essential patents that have allowed a competitive market to flourish, with a variety of open-source, cost-effective machines that are affordable to home users [8, 51]. In essence, the FFF process works by melting filaments of thermoplastic material, extruding the polymer melt through a nozzle, and recreating the part's geometry on a layer-by-layer basis. The melting behavior of the filament has been of significant interest in past years. It has been the topic of several publications that attempt to shed light upon its underlying physics [1, 18–22, 49, 52].

While understanding the formation of the polymer melt within the nozzle is paramount to optimization efforts that can increase the effectiveness and the speed of production of FFF

parts. Unfortunately, no definitive answer exists to explain how it occurs. Various methods exist to model the melting behavior of the polymer film [53, 54]. However, only a handful of models deal with the case of FFF directly. The model proposed by Osswald et al. [1] uses the concept of pressure-induced melt removal, first derived by Stammers and Beek [53] and further explained by Tadmor and Gogos [55]. The model incorporates the formation of a melt thickness that varies as a function of the force exerted by the solid filament. Here, the melt is removed by the squeezing action of the solid on the melt. Others have used this concept [56, 57] to explain the melting of polymer in different processing techniques.

To model the melt film thickness generated from the pressure-induced melt removal process, the authors[1, 53, 54] used Stefan's condition. In Stefan's condition, a heat transfer balance is performed at the solid-melt interface. It assumes that the heat conduction from the heated surface to the interface equals the amount of heat needed to melt the polymer material plus the heat dissipation from the solid-melt interface to a temperature T_∞. An important parameter needed to model the melt film thickness formation is the melting temperature of the polymer. In the case of amorphous thermoplastic material, there is no sharp distinction between liquid and solid states. Thus a melting temperature that allows discerning between the two behaviors does not exist. However, a softening temperature can be used instead. Tadmor and Gogos [55] suggested using the glass transition temperature as the melting temperature to obtain the mechanical properties. This is not the case for a semi-crystalline material. These materials possess a defined melting temperature where the material undergoes a transition from solid to melt.

This work explores the fundamental of melting of amorphous materials expanding on the work presented by Stammers and Beek [10]. Experimental validation will be corroborated using state-of-the-art equipment. A setup was built to allow the application of constant force during melting. The melt film is analyzed afterward using Computed Tomography (CT) scans. The results are compared with simulations that originate from COMSOL Multiphysics, as well as the analytical solution presented by Stammers et al. [53]. The derivation of an improved model, create by Stammers et al., was attempted, including the effects of convection heat transfer during flow. An attempt to find the softening temperature of amorphous material was made using rheological and thermal equipment. Dynamic mechanical analysis (DMA) and differential scanning calorimeter (DSC) tests were performed and compared. The simulation setup, material properties, and experimental procedure are described in detail. The results shown here will aid in understanding the physics of melt formation in the FFF process for amorphous materials.

4.2 Experimental

4.2.1 Materials

For the work presented here, four materials were used. The materials were outsourced from Grainger (Madison Branch, Madison, WI, USA) with a 6.35 mm (0.25 in) diameter. The materials of choice were polycaprolactam (PA6), polypropylene (PP), polycarbonate (PC),

and polyvinyl chloride (PVC). The last two materials have an amorphous structure, while the former two have a semi-crystalline structure. To perform the COMSOL simulation, rheological properties, as well as thermal properties, were needed. Available properties were taken from literature and are shown in Table 4.1. In addition, actual thermal and rheological values were measured for all the materials to guarantee a more accurate analytical comparison.

Table 4.1: Material thermal and rheological properties. Taken from [33, 58].

Materials	ρ (kg/m^3)	c_p (J/g-K)	k (W/m-K)
PVC	1160 - 1350	0.8 - 0.9	0.13 - 0.20
PA6	1120 - 1150	1.59 - 1.70	0.22 - 0.33
PC	1200 - 1240	1.17 - 1.50	0.19 - 0.21
PP	900 - 910	1.8	0.17 - 0.25

4.2.2 Setup

The experimental setup, similar to Stammers and Beek [53], consisted of a built-in heated plate with a guiding system that supports the weight and the holding position of the material rod. The material selected for the heated plate was aluminum due to its easy machineability. Two cartridge heaters were placed at the center of the plate to maintain an accurate temperature during the experiments. The cartridge heater dimensions were 6.35 mm in diameter and 76.2 mm in length and possess a power of 200 W. To control the temperature, a K-type thermocouple with a temperature controller was used.

The guiding system consisted of a squared tower. Four linear bearings were used along with a platform to allow accurate movement of the weight used. A guide was attached to two supports connected to the tower to maintain the rod steady. A schematic of the setup is shown in Figure 4.1.

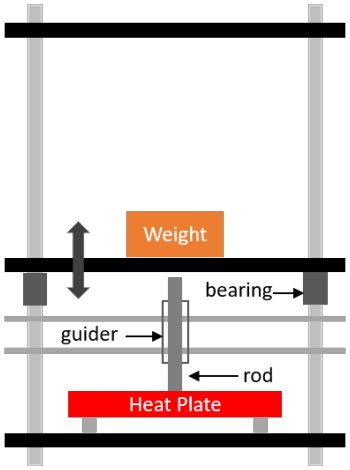

Figure 4.1: Schematic of experimental setup.

4.2.3 Experimental Procedure

Two sets of experiments were performed. First, the melt film thickness was compared using two different cooling methods. The first method consisted of an annealing process. Here, the material was cooled down slowly from the processing temperature to ambient temperature. The second method consisted of a quenching process using water. Here, the material undergoes a drastic change in temperature from the processing temperature to the temperature of the water. These methods were performed to determine how the cooling rate affects the melt film thickness. The procedures were done using a weight of 3.97 kg (38.945 N). Later, a weight of 5.76 kg (56.486 N) was used to study the effect of force on the melt film thickness. The temperatures used are shown in Table 4.2.

Table 4.2: Processing temperatures.

Force	38.945 N	56.486 N
Material	Temperature (^oC)	Temperature (^oC)
PA6	275	270
PP	230	230
PVC	230	230
PC	210	220

The temperatures selected were at least 40 ^{o}C above the glass transition and the melting temperature. Once the heated plate was raised to the respective temperatures, an aluminum

foil was placed on the heated plate. After one minute of heating the aluminum foil, the material rod was contacted with the heated aluminum foil. Right after placing the rod, the mass was positioned for the application of the force. After allowing the material to melt and flow for 30 seconds, the weight was removed along with the aluminum foil to maintain the shape of the melt film created due to the melting process. Finally, each rod was left to solidify at ambient temperature or was placed on a water bath. A schematic of the process is shown in Figure 4.2.

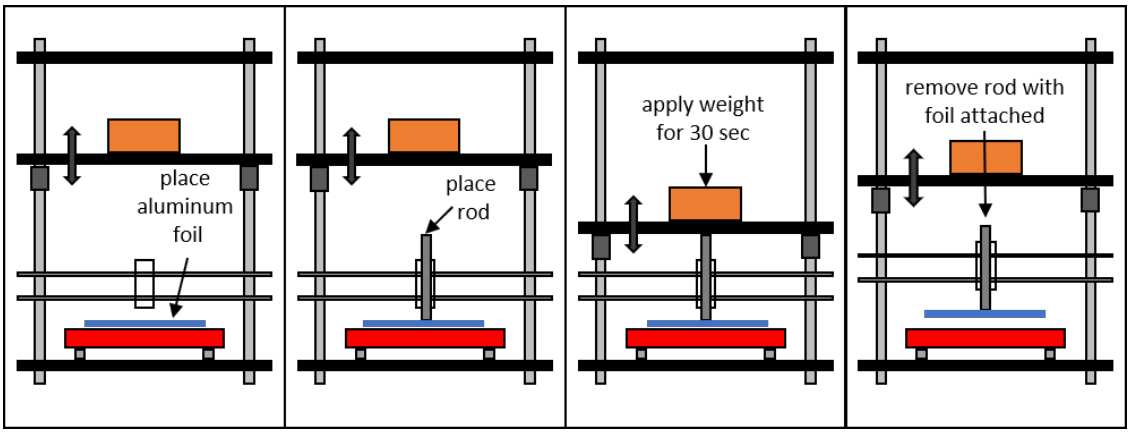

Figure 4.2: Schematic of experimental procedure.

A total of 5 samples were performed for each material to verify the reproducibility of the results. To reduce scanning time in the CT scan, all the samples were scanned at the same time. The drawback of this is that the resolution of the CT scan is lower. However, the resulting resolution allows visualization and measurement of the melt film thickness. A higher resolution can be achieved if each rod is analyzed separately.

4.2.4 Micro Computed Tomography (μ-CT) of Melt Film

A ZEISS METROTOM 800 (ZEISS, Germany) was used to measure the dimensions of the melt film thickness. A resolution of 41.8 μm/pixel was used to obtain a good-resolution image. The μ-CT data comprises a 3D reconstruction of the scanned sample, which is exported to 2D image stacks [59]. The shape of the melt film thickness can be clearly distinguished in the grayscale images. Fiji [60], an open-source image processing software, was used to analyze the ZEISS METROTOM 800 output data. Using the resolution of the scan and the Scale Bar tool in Fiji, the dimensions of the melt film were measured for all the materials.

4.2.5 Pressured Induced Melt Removal Solution

The analytical solution of the pressured induced melt removal solution was taken from Tadmor and Gogos [55] and Stammers and Beek [53]. Equation 4.1 was used to calculate the

vertical filament velocity. Next, the viscosity was computed using the power-law model. Finally, the rate obtained was used to calculate the melt film thickness using the Stefan Condition [61] shown in Equation 6.15.

$$U_{sz} = \frac{2\delta^3}{3\pi\mu_f R^4 \beta}(F - \pi p_o R^2) \tag{4.1}$$

$$\delta = \frac{k(T_h - T_m)}{\rho_s U_{sz}[\lambda + C_s(T_m - T_o)]} \tag{4.2}$$

where $\beta = \frac{\rho_s}{\rho_m}$, ρ_s is the density of the solid material, ρ_m is the density of the melt material, F is the filament force, μ_f is the viscosity of the melt film, p_o is the atmospheric pressure, R is the rod radius, k is the thermal conductivity of the material, U_{sz} is the filament velocity, T_h is the heater temperature, T_m is the melting temperature, T_o is the ambient temperature, C_s is the specific heat, and λ is the heat of fusion.

4.2.6 Thermogravimetric Analysis (TGA)

A Netzsch TGA 209 F1 (NETZSCH GmbH & Co. Holding KG, Selb, Germany) was used for the thermogravimetric analysis to ensure that the materials will not degrade during the sample preparation. A temperature ramp of 10 K/min was utilized from 30^oC to 800^oC. The final temperature was held for 10 min before cooling. TGA will allow the determination of decomposition events of the materials. It will also aid in determining the presence of fillers and additives within each material.

4.2.7 Differential Scanning Calorimetry (DSC)

A Netzsch DSC 214 Polyma (NETZSCH GmbH & Co. Holding KG, Selb, Germany) was used for the thermal analysis. To perform a high-quality measurement, the methods presented in the Netzsch DSC Handbook [62] were used. Here, the sample mass, the isothermal phase, heating/cooling rates (10 K/min), crucible type, and test atmosphere are suggested. The initial temperature for all the materials was 20 ^{o}C. A pierced lid aluminum crucible was used for all the materials. Two heating phases were made for each material to eliminate processing influences on the result [63]. The first heating shows the entire history of the sample, which will be used for the determination of the softening/melting temperature for all the materials tested [62].

The second set of experiments were performed following the same procedure as suggested by the DSC Handbook. However, the heating rate was modified to 2 K/min. This temperature will be used to compare heating rates and be consistent with the heating rate used in the DMA procedure.

4.2.8 Double Shear Test

Sample Preparation

The double shear test requires cylindrical samples. To obtain the samples, the raw material was cut into smaller pieces. Later, the material was compression molded using a Carver press Auto C-PL, H (Carver, Inc, Wabash, Indiana). The process temperature, maximum applied force, and process time are shown in Table 4.3.

Table 4.3: Compression Molding Parameters.

Material	Temperature (^oC)	Max Force (lbs)	Compression Time (min)
PA6	300	8000	6
PP	330	7000	5
PVC	220	8000	10
PC	320	6500	5

A cutting die was later used to cut the samples to a diameter of 9.5 mm. Finally, an adhesive, a thin film of Sico MET 700, was used to attach the samples to the test fixture.

Instrument Setup

A Netzsch Dynamic Mechanical Thermal Analyzer EPLEXOR®500N (DMTA) (NETZSCH GABO Instrument GmbH, Ahlden, Germany) was used for the double shear test. A temperature sweep was performed with a frequency of 1 Hz. A temperature ramp of 2 K/min was used. This temperature ramp allowed for homogenization of the material during testing. A strain % of 0.05 was used for all the materials to maintain the material in the linear viscoelastic region. A total of six tests were performed for all samples. The initial temperature for the first three samples was 30 ^oC while the other three samples were at a temperature close to the inflection temperature (T_g or T_m) respectively. The temperature ranges for the materials are shown in Table 4.4.

Table 4.4: Temperature range for double shear test.

Material	First Temperature Range (^oC)	Second Temperature Range (^oC)
PA6	30 - 300	120 - 300
PP	30 - 240	140 - 240
PVC	30 - 240	65 - 240
PC	30 - 240	110 - 240

4.2.9 COMSOL Multiphysics

COMSOL Multiphysics was used to simulated the melt film formation of the process. The software was selected due to the level set physics that allows the interaction between two fluids. Since the material is being melted on a hot plate, the material will flow to the outer region of the rod, interacting with the air in the area.

Simulation Setup

It is necessary to simulate the pressure-induced melt removal process to simulate the material and air interface interaction. The physics which allows this simulation are laminar flow, level set, and heat transfer in fluids. A time-dependent study with phase initialization was employed for the simulation. The phase initialization is required for the level set physics.

In the global definition, variables were created. In particular, the heater temperature and the viscosity model parameters were specified for each material and heater temperatures. Later, a step function was created for the application of the force. Finally, an analytical function was developed to evaluate the viscosity as a function of temperature.

The geometry was modeled axisymmetric in a 2D plane. Here, a rod (polymer) with a radius of 3.175 mm and a length of 15 mm was used. Next to the rod, an air region with a height of 7 mm and a width of 5 mm was created. Since the melt film is created next to the heated region (area of interest), only this area was modeled. Later, the regions were assigned with the respective material. Figure 4.3 shows the geometry. Next to the PVC and air interface, a region was removed (0.01 mm by 1 mm) to approximate the simulation setup to the experimental setup.

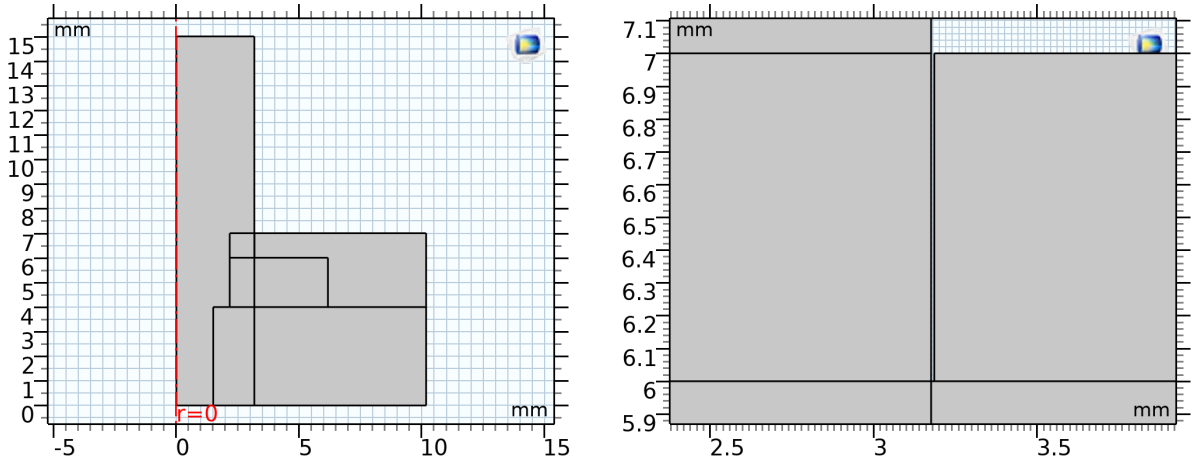

(a) (b)

Figure 4.3: COMSOL geometry where (a) is the entire geometry and (b) is a region were material was removed.

Each material properties were assigned according to the simulated material. In the laminar flow physic, two-fluid properties and material regions were created. Walls and

outlets were specified. As the materials have high viscosity, the inertial terms were neglected. Finally, a pressure inlet was applied at the top of the rod, assigning the applied force to the material. The pressure was set together with the step function, which helps the numerical simulation at the first steps. A slip wall boundary condition (from (3.175, 6) to (3.175, 15)) was assigned simulating the guider used in the experimental setup.

In the level set physic, the reinitialization parameter was set to $14*10^{-5}$ m/s. A good estimation of the reinitialization parameter is the maximum expected velocity magnitude [64]. At the same time, the initial values of both materials were specified, and the initial interface was defined. Finally, a cubic discretization was selected to increase the resolution of the material and air interface.

In the heat transfer in fluids physic, two liquids were assigned. A temperature was given to the lower surface of the air and polymer. An outflow was also set to allow heat flow out of the geometry. Moreover, the Phase Change Material feature for the material was enabled, which tracks the position of the melting region within the simulation. Here the melting temperature and the heat of fusion of the material were specified. Notice that the heat of fusion was given only for PA6 and PP as these are semi-crystalline materials and have a defined melting temperature. For the Amorphous materials, the heat of fusion had a zero value, and the glass transition temperature was used as the melting temperature.

Two multiphysics were enabled for the simulation. These are two-phase flow and non-isothermal flow. In the two-phase flow physic, each material was assigned. In the non-isothermal flow physic, the viscous dissipation option was disabled. Also, the surface tension between the materials was disabled.

A fine free triangular mesh was used for most of the geometry. An extra-fine mesh was used to increase the resolution of the area of interest using fluid dynamics physics. The rest of the geometry was meshed using a regular mesh as shown in Figure 4.4.

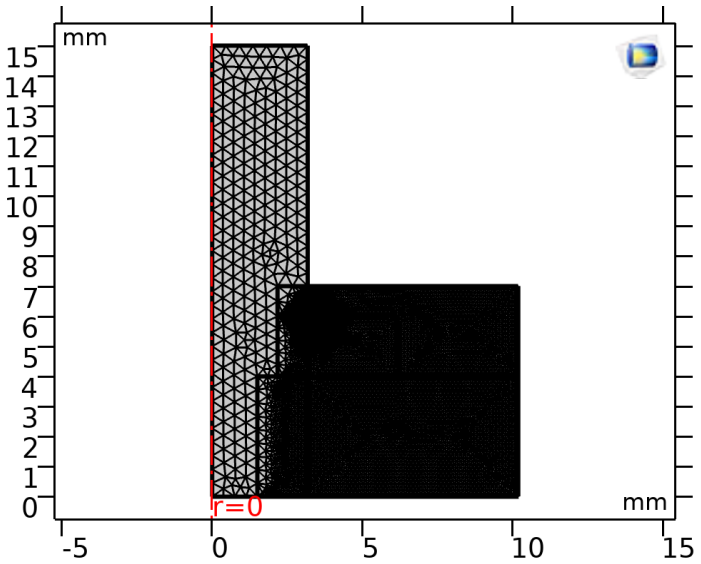

Figure 4.4: Schematic of the mesh resolution for the simulation geometry.

A simulation time of 35 seconds was implemented to compare the experimental data, including starting and removing the sample from the heated surface. Finally, the data is processed and compared with both the experimental data and the analytical solution.

4.2.10 Rheological Properties

The rheological properties of PA6, PP, PVC, and PC were measured using a AR 2000ex rheometer (TA Instruments, Inc., New Castle, DE) with 25 mm parallel plate geometry. The dynamic viscoelastic properties were determined within the frequency range of 0.1 Hz - 100 Hz (0.0628 - 628.3 rad/s) using a strain value within the viscoelastic region (strain % of 0.1). A frequency sweep test was performed for all materials. The specific temperatures are shown in Table 4.5.

Table 4.5: Rheometer Temperatures

Materials	Temperatures (^oC)			
PA6	270	300	330	-
PP	180	200	230	260
PVC	210	215	230	245
PC	200	215	230	245

The gap used for the test was 1 mm. Applying the Cox-Merz rule [34], which states that the complex viscosity and steady shear viscosity are equivalent when the angular frequency w is equal to the constant shear rate $\dot{\gamma}$ [65] as shown in Equation 4.3.

$$|\eta^*(w)| = \eta(\dot{\gamma} = w) \tag{4.3}$$

Since the instrument used for the viscosity test has a limited shear rate range, the time-temperature-superposition (TTS) principle was performed. The Carreau-Yasuda (CY) model was used to predict the viscosity as a function of the shear rate as shown in Equation 4.4

$$\frac{\eta}{\eta_o} = (1 + (\lambda\dot{\gamma})^a)^{\frac{b-1}{a}} \tag{4.4}$$

where η_o is the zero-shear viscosity, λ is the consistency, b is the rate index, and a is the transition index. The CY viscosity model was used to describe the viscosity of the materials fully. The fitting parameters for the CY model were found using the Matlab fitting tool.

4.3 Pressure Induced Melt Removal Process Including Convection Term

This section shows the derivation of the pressure-induced melt removal process, including convection effects within the melt film thickness. The derivation, as well as the boundary conditions and assumptions, will be described in this section.

4.3.1 Mathematical Derivation

The derivation is performed under the assumption of the creation of a melt film thickness. Here, a rod of material is pressed towards a hot surface. During the melting of the rod, a film is created. This film is expected to vary due to the force or pressure it is pressed towards the heated surface. A schematic of this process is shown in Figure 4.5. The derivation is similar to Stammers and Beek [53]. In addition, the effect of convection will be incorporated into the energy equation.

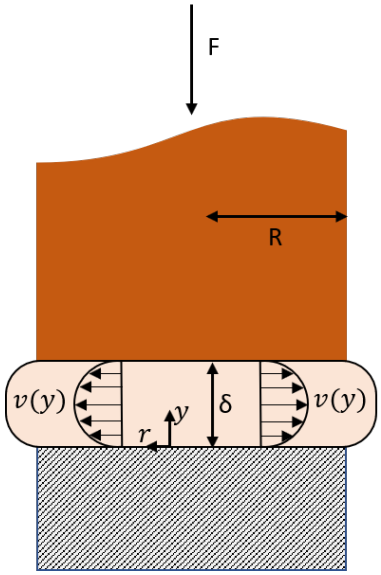

Figure 4.5: Schematic of a pressure-induced melt removal of a solid polymer.

Taking the solution of Tadmor and Gogos [55] and Stammers and Beek [53] the velocity of the rod can be calculated using Equation 4.1.

To calculate the viscosity of the melt film at a given filament velocity, it is necessary to calculate an average shear rate in the melt film region. After substitution, the shear rate term is given by Equation 4.5.

$$\frac{\partial v_r}{\partial z} = \frac{6r(-U_o)}{\delta^3}(z-\delta) \tag{4.5}$$

To use this term for any viscosity model, an average shear rate is calculated using Equation 4.6.

$$\langle \frac{\partial v_r}{\partial z} \rangle = \frac{1}{V} \oint_V \frac{\partial v_r}{\partial z} dV \tag{4.6}$$

Substituting the expression and integrating over the respective limits, the average shear rate results in Equation 4.7.

$$\langle \frac{\partial v_r}{\partial z} \rangle = \frac{2}{3} \frac{R}{\delta^2} U_o = \frac{2}{3} \frac{R}{\delta^2} U_{sz} \beta = \dot{\gamma}_f \tag{4.7}$$

Energy Equation

The velocity of the solid polymer cannot be calculated since the value δ is still unknown. This value is determined by performing an energy balance in the solid-melt interface as shown in Equation 4.8.

$$-k_m \frac{dT_L}{dz}|_{z=\delta} = \rho_s U_{sz} \lambda - k_s \frac{dT_S}{dz}|_{z=\delta} \tag{4.8}$$

To solve this equation, it is necessary to calculate the temperature distribution of the solid filament and the melt film area. The following are the boundary conditions required to solve the respective temperature distributions.

$$T_L = T_h \quad \text{at} \quad z = 0 \tag{4.9a}$$

$$T_L = T_m \quad \text{at} \quad z = \delta \tag{4.9b}$$

$$T_S = T_m \quad \text{at} \quad z = \delta \tag{4.9c}$$

$$T_S = T_\infty \quad \text{at} \quad z = \infty \tag{4.9d}$$

Energy Balance of Solid Filament

Simplifying the energy equation in the solid filament results in Equation 4.10.

$$\rho_s C_p v_z \frac{\partial T_S}{\partial z} = k_s \frac{\partial^2 T_S}{\partial z^2} \tag{4.10}$$

Substituting $v_z = -U_{sz}$ results in Equation 4.11.

$$-\rho_s C_p U_{sz} \frac{\partial T_S}{\partial z} = k_s \frac{\partial^2 T_S}{\partial z^2} \tag{4.11}$$

C_p is the specific heat of the solid filament, and k_s is the thermal conductivity of the solid material. Simplifying the expression results in Equation 4.12.

$$\frac{\partial^2 T_S}{\partial z^2} + a \frac{\partial T_S}{\partial z} = 0 \tag{4.12}$$

where $a = \frac{U_{sz}}{\alpha_s}$ and $\alpha_s = \frac{k_s}{\rho_s C_p}$. Solving the second order differential equation results in Equation 4.13.

$$T_S(z) = \frac{C_2 e^{-az}}{a} + C_3 \tag{4.13}$$

Using the respective boundary conditions, the temperature distribution and the temperature gradient are shown in Equation 4.14 and 4.15 respectively.

$$T_S(z) = T_\infty + (T_m - T_\infty)e^{(a(\delta - z))} \tag{4.14}$$

$$\frac{dT_S}{dz} = -a(T_m - T_\infty)e^{(a(\delta - z))} \tag{4.15}$$

Energy Balance at Melt Film Region

Similar to the energy balance performed in the solid filament, simplification in the melt region results in Equation 4.16.

$$\rho_m C_p \langle v_z \rangle \frac{\partial T_L}{\partial z} = k_m \frac{\partial^2 T_L}{\partial z^2} \tag{4.16}$$

where $\langle v_z \rangle = -\frac{U_o}{2}$ is the average velocity of the melt region. This term is calculated by integrating the velocity profile in the z-direction over the entire volume, similar to the process performed in Equation 4.6. Simplifying the equation results in Equation 4.17.

$$\frac{\partial^2 T_L}{\partial z^2} + b\frac{\partial T_L}{\partial z} = 0 \tag{4.17}$$

where $b = \frac{U_o}{2\alpha_L}$, and $\alpha_L = \frac{k_m}{\rho_m C_p}$. Solving the differential equation results in Equation 4.18.

$$T_L(z) = \frac{C_4 e^{-bz}}{b} + C_5 \tag{4.18}$$

Using the respective boundary conditions results in the temperature profile and temperature gradient in the melt region as shown in Equation 4.19 and 4.20 respectively.

$$T_L(z) = T_h + (T_m - T_h)\frac{e^{-zb} - 1}{e^{-\delta b} - 1} \tag{4.19}$$

$$\frac{dT_L}{dz} = -b(T_m - T_h)\frac{e^{-zb}}{e^{-\delta b} - 1} \tag{4.20}$$

Solution of Energy Balance at Solid-melt Interface

To solve Equation 4.8 it is necessary to solve the temperature gradient of both the solid filament and melt region at the interface $z = \delta$. These are shown in Equation 4.21 and 4.22.

$$\frac{dT_S}{dz}|_{z=\delta} = -a(T_m - T_\infty) \tag{4.21}$$

$$\frac{dT_L}{dz}|_{z=\delta} = -b\frac{(T_m - T_h)}{(1 - e^{\delta b})} \tag{4.22}$$

Substituting these terms into Equation 4.8 results in Equation 4.23.

$$k_m b\frac{(T_m - T_h)}{(1 - e^{\delta b})} = \rho_s U_{sz}\lambda + k_s a(T_m - T_\infty) \tag{4.23}$$

Solving for the melt film thickness δ results in Equation 4.3.1.

$$\begin{aligned}\delta &= \frac{1}{b}\ln\Big[1 - \frac{k_m b(T_m - T_h)}{(\rho_s U_{sz}\lambda + k_s a(T_m - T_\infty))}\Big] \\ &= \frac{2k_m}{U_{sz}\rho_s C_p}\ln\Big[1 + \frac{1}{2}\frac{C_p(T_h - T_m)}{(\lambda + C_p(T_m - T_\infty))}\Big]\end{aligned} \tag{4.24}$$

Compared to the solution of Stammers et al. [10], the melt film thickness derived in this work takes into account the effect of convection within the melt film. For comparison purposes, the term used by Stammers is shown in Equation 6.15.

4.4 Results and Discussion

4.4.1 TGA Results

TGA results using a nitrogen and air atmosphere are shown in Figure 4.6. The results visualize when a mass loss occurs and the number of events that indicate the type of molecule that degrades. For the PA6 material under nitrogen atmosphere, the sample displayed a single-stage degradation in the temperature range of 380 - 515 ^oC corresponding to the degradation of neat PA6, which results in a residual mass of 3.16 %. For the air atmosphere, the data displayed a second-stage degradation (between 480 - 540 ^oC). The second-stage degradation might be linked with the oxidation and aromatization of aliphatic carbons followed by the release of CO and CO_2 gases [66]. The first stage has a mass change of 88.25 %, while the second stage has a mass shift of 9.91 % resulting in a residual mass of 1.12 %.

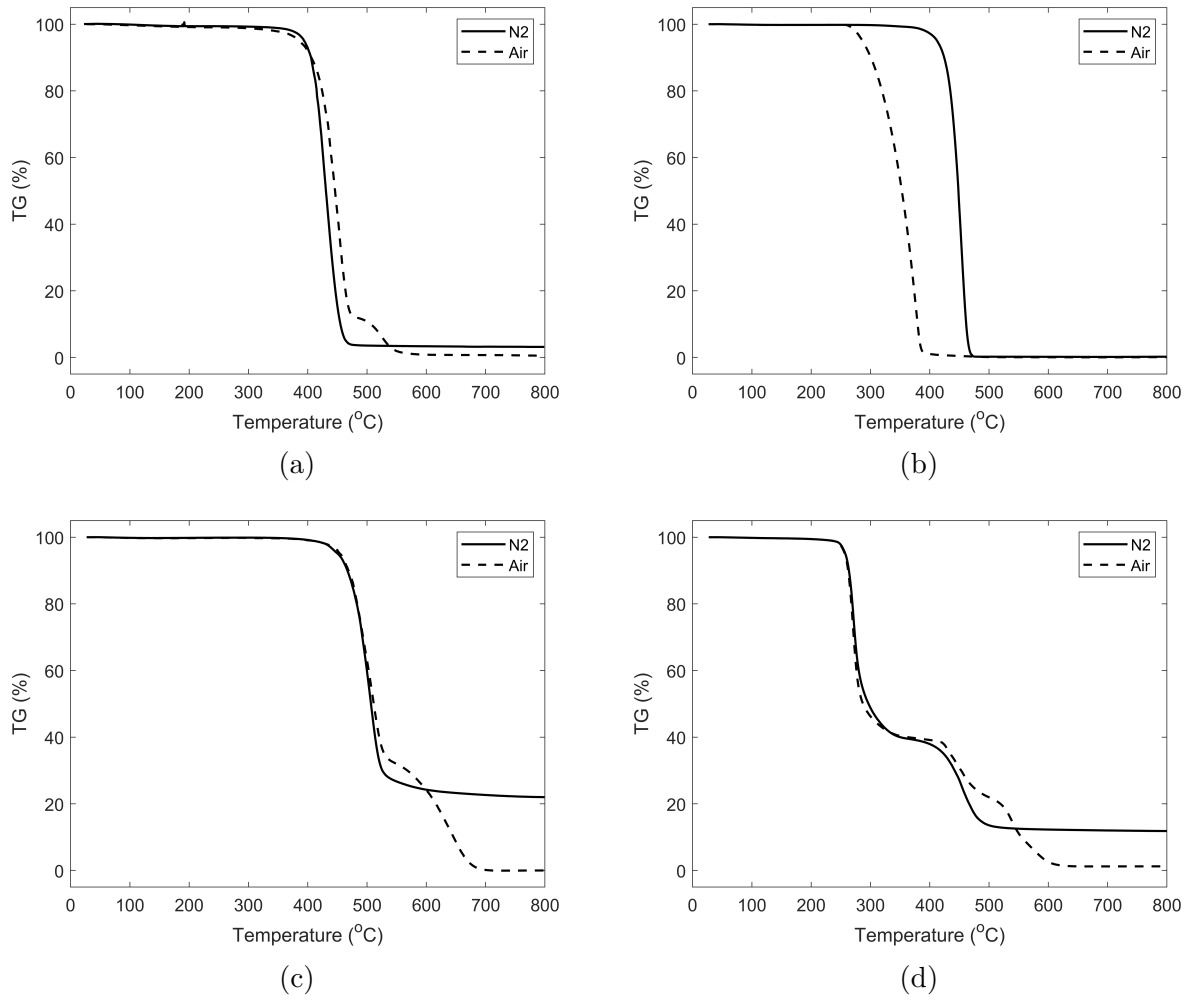

Figure 4.6: TGA Results for (a) PA6, (b) PP, (c) PC, and (d) PVC.

For the PP material, a first-stage degradation can be observed for both nitrogen and air atmosphere. No char residue is left for the PP showing the complete decomposition property of PP when exposed to high heat. Degradation under nitrogen occurs in the range of 340 - 480 ^oC with a residual mass of 0.22 %, which can be described as the degradation of the PP skeleton [67]. For an atmosphere of air, degradation occurs at a range of 260 - 400 ^oC with a residual mass of 0.11 %.

For the PC material, a first-stage degradation can be observed for a nitrogen atmosphere. Degradation starts at 400 ^oC and ends at 600 ^oC with a residual mass of 22.0 %. For the air atmosphere, a second-stage is observed from 550 ^oC to 700 ^oC with a residual mass of 0.01%. These results are similar in value to what is found in literature [68, 69].

For the PVC material, a second-stage degradation can be observed for both nitrogen and air atmosphere. For the nitrogen atmosphere, carbonaceous char during decomposition was formed. Initial decomposition between 240 ^oC and 300 ^oC was rapid. The decomposition

rate was slowed dramatically when the mass % reached 40 % and was not decreased until temperatures of about 400 ^oC. From there on to 500 ^oC decomposition was fast. Above this temperature, the char formed decomposed slowly. The first decrease corresponded to the decomposition of HCL, while the second decrease corresponded to unsaturated hydrocarbons [70]. In the air, the rate of decomposition was similar to nitrogen. However, decomposition continued at temperatures above 500 ^oC. The first decomposition was HCL, while the second corresponds to CO_2. The residual mass resulted in 11.83 % for a nitrogen atmosphere, while the air atmosphere had a residual mass of 1.24 %.

The values found here suggest the processing temperature for each material to avoid decomposition. The temperatures are 400 ^oC for PA6 and PC, 250 ^oC for PVC, and 350 ^oC for PP. These temperatures were taken into consideration when processing the samples for the DMA test.

4.4.2 DSC Results

DSC results for two heating ramps are shown in Figure 4.7. The results are averaged from three runs, all at the same conditions.

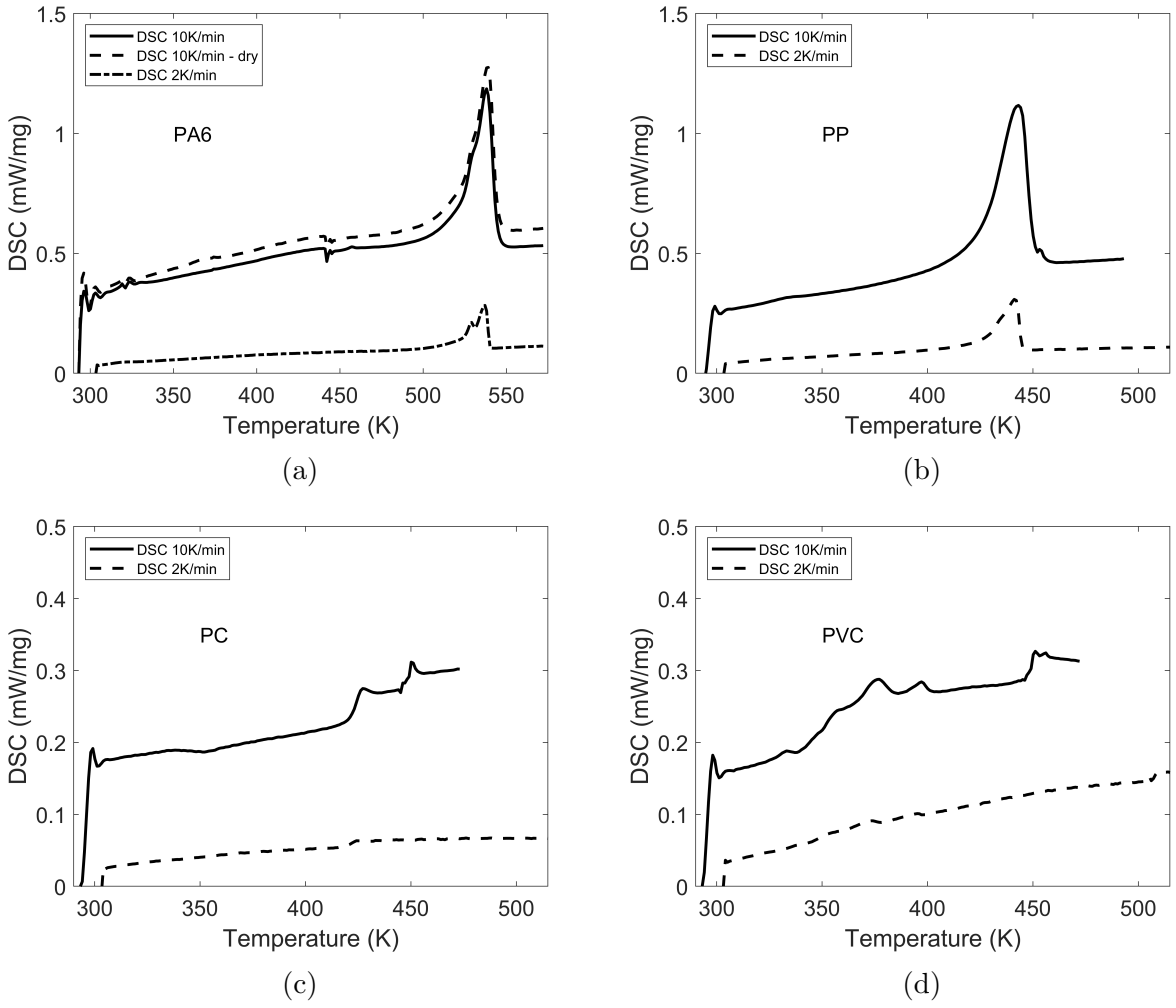

Figure 4.7: DSC Results for (a) PA6, (b) PP, (c) PC, and (d) PVC.

Figure 4.8a shows the DSC result for the PA6 material. At a temperature ramp of 10 K/min, an exothermic region can be observed around a temperature of 443K. To discard the presence of water, the PA6 was dried at a temperature of 85 ^oC for 12 hours. As observed in the figure, the exotherm can be observed even for the dry material. This transition is not observed for a 2K/min temperature ramp due to the sensitivity decrease. For a high heating rate, the resolution is decreased while the sensitivity increased. The opposite happens when the heating rate is decreased [71]. The exothermic region is due in part to the recrystallization of the PA6 molecules at the respective temperature [72, 73]. The melting temperature and the heat of fusion of PA6 and PP are shown in Table 4.6.

Table 4.6: Melting temperature and heat of fusion of PA6 and PP

Condition	Melting Temperature, T_m (^oC)	Heat of Fusion, λ (J/kg)
PA6 - 10 K/min	264.95	68590
Dry PA6 - 10 K/min	265.55	71220
PA6 - 2 K/min	263.87	69310
PP - 10 K/min	170.01	103400
PP - 2 K/min	168.18	95670

Figure 4.8c and Figure 4.8d shows the results for the PC and PVC respectively. As shown in the figure for PC, the glass transition can be observed for both heating rates. Artifacts at the end of the data can be seen for the 10 K/min heating rate. These artifacts are also present for PVC for both heating rates. Artifacts are thermal events that do not directly relate to changes in the physical properties of the sample [74].

For the PVC material, the first transition occurs at 65.15 ^oC and represents the glass transition temperature. The first endothermic region represents the melting of the partially gelled crystallites or the level of gelation present in the first area. The second endotherm means the melting of crystallites that did not gel during the heating of the sample [75]. With this information, the degree of gelation can be determined. To calculate the degree of gelation, two endothermic areas, H_a and H_b, are needed [76]. The degree of gelation can be calculated using Equation 4.25.

$$DegreeofGealtion = \frac{EndothermA}{EndothermA + EndothermB} \tag{4.25}$$

Endotherm A and B are 4998 J/kg and 626 J/kg for a 10 K/min heating rate. The degree of relation results in 88.87 %. The higher the degree of gelation, the better the mechanical properties of the material will be [77]. The melting temperature for PC and PVC are shown in Table 4.7.

Table 4.7: Glass transition temperature of PC and PVC

Condition	PC - 10 K/min	PC - 2 K/min	PVC - 10 K/min	PVC - 2 K/min
T_1g (^oC)	151.48	148.18	65.15	72.27
T_2 (^oC)	-	-	117.28	107.54
T_3 (^oC)	-	-	130.15	126.36

4.4.3 DMA Results

DMA results for all the materials are shown in Figure 4.8. Here, the viscosity is plotted as a function of temperature.

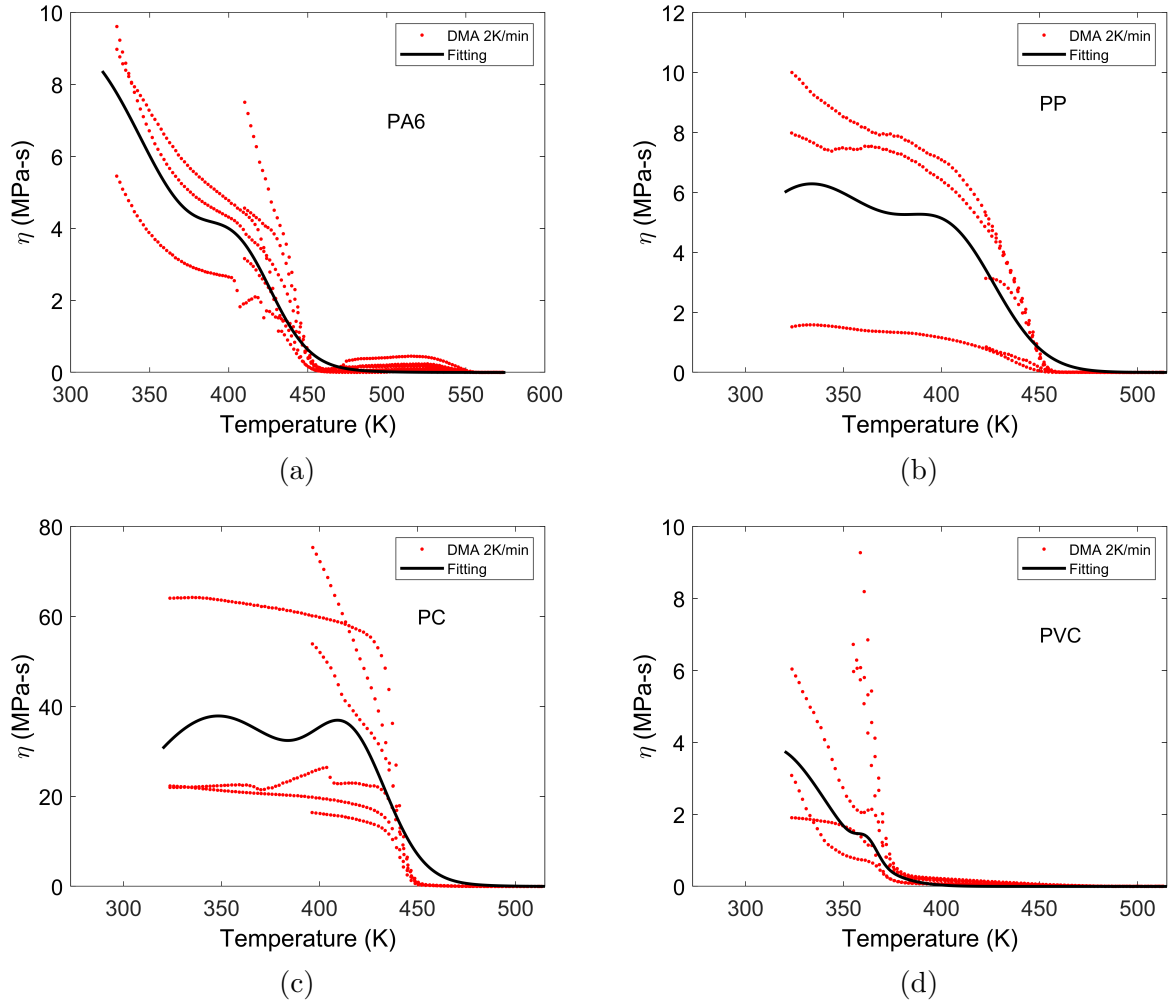

Figure 4.8: DMA Results for (a) PA6, (b) PP, (c) PC, and (d) PVC.

As mentioned, the tests were performed using a heating rate of 2 K/min to allow for homogenization of the material during the trial. PP, PC, and PVC can be seen as a clear transition from the steady viscosity to a decrease in viscosity, characteristic of thermoplastic materials. The change from constant viscosity to a reduction in viscosity happens at a temperature of 157 ^oC, 162 ^oC, and 86 ^oC for PP, PC, and PVC, respectively. These correspond to the glass transition temperature of PC and PVC. It also corresponds to the melting temperature of PP. For the PA6 material, two transition temperatures are observed. The first transition happens at a temperature of 163 ^oC while the second transition happens at 266 ^oC. The latter corresponds to the melting temperature. The first transition corresponds

to the material's recrystallization, which can also be seen in the DSC test for PA6. This first transition can be partly due to the thermal history of the material, primarily in the production process of the sample.

The viscosity for all the materials was fitted and modeled using a Gaussian function of second-order as shown in Equation 4.26. The fitting parameters are shown in Table 4.8. The R^2 values for all the fittings are higher than 50 %, indicating that the model has a moderate effect on the temperature.

$$\eta(T) = \sum_{i=1}^{n} a_i e^{-(\frac{T-b_i}{c_i})^2} \tag{4.26}$$

Table 4.8: Viscosity model parameters (Viscosity with units of MPa)

Material	a_1 (MPa-s)	b_1 (K)	c_1 (K)	a_2 (MPa-s)	b_2 (K)	c_2 (K)	R^2	R_2-adjusted
PA6	9.095	296.4	82.08	2.258	407	31.79	0.8959	0.8946
PP	6.26	332.6	61.37	3.391	406.5	33.58	0.6429	0.639
PVC	3.894	312.1	40.9	0.505	362.3	7.429	0.7635	0.7596
PC	37.86	348	61.01	24.73	416.1	26.52	0.5574	0.5502

Here the a_i parameters correspond to the viscosity before the first inflection. The b_i parameter corresponds to the temperature shift at which the inflection occurs. The c_i parameter corresponds to an amplitude parameter which helps to control the shape of the function. The Gaussian function used is similar in shape to the Maxwell-Wiecher model, shown in Equation 4.27 which is used to model stress relaxation of polymers [32].

$$E(t) = \sum_{i=1}^{n} E_i e^{-(1/\lambda_i)t} \tag{4.27}$$

Here E_i corresponds to the steady modulus before inflection, and λ_i corresponds to the time where the inflection occurs. Both models qualitatively represent the experimental values. However, the models differ in part due to the properties that predict. For the Gaussian function, since the viscosity is a function of many parameters (e.i. temperature, rate of deformation, materials, etc.), it requires more parameters than the Maxwell-Wiechert model to predict the data behavior.

4.4.4 DSC vs DMA

A comparison between the DSC and DMA can be observed in Figure 4.9. When comparing the DSC and DMA results, it can be noticed that the inflection temperature (melting

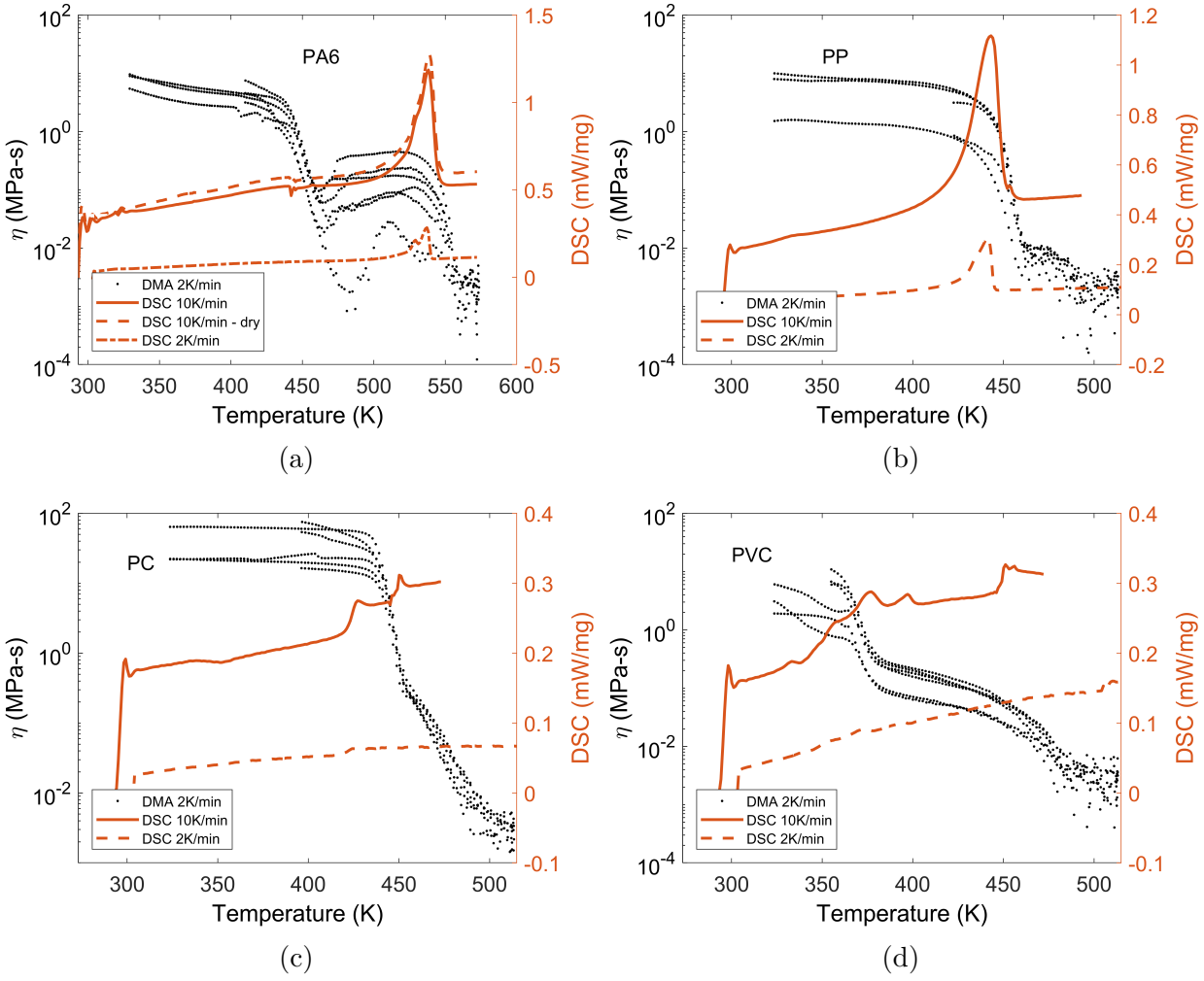

Figure 4.9: Comparison of DSC and DMA results for (a) PA6, (b) PP, (c) PC, and (d) PVC.

temperature and glass transition temperature) is shifted between tests. A temperature difference of 2 ^oC, 13 ^oC, 11 ^oC, and 21 ^oC are seen for PA6, PP, PC, and PVC respectively. This difference is due in part to the heat transfer mechanisms present in the tests. The DSC shows the thermal response of the sample, while the DMA shows the thermal and fatigue response of the sample. The DSC device is a thermal analysis instrument that determines the temperature and heat flow associated with material transitions as a function of time, and temperature [78]. The signal of the DSC is a function of many parameters. Some of the parameters are sample mass, sample size (superficial area), and heating rate. At the same time, the mechanical and thermal response of the DMA will be a function of the heating rate, sample thickness, sample diameter, temperature, time, and frequency, among others [79]. The DMA results will be used for T_g and T_m since it possesses between 10 to 100 times the sensitivity to the changes occurring at T_g [80].

4.4.5 Rheological Properties

A master curve was created using the viscosity data and the Trios software from TA Instruments (TA Instruments, DE, USA). A time-temperature-superposition (TTS) was used to find the shift factor in the x-direction. The reference temperature selected were 215 ^oC for PVC and PC, 270 ^oC for PA6, and 200 ^oC for PP. The Arrhenius model was used for the PA6 and PP material, while the Williams-Landel-Ferry (WLF) model was used for PVC and PC. The activation energy was 70022.8 J/mol for PA6 and 22035.4 J/mol for PP. The C_1 and C_2 parameters were 0.6377 and 12.8285 K for PVC and 3.4847 and 127.51 K for PC. Figure 4.10 shows the shift factor for all the materials.

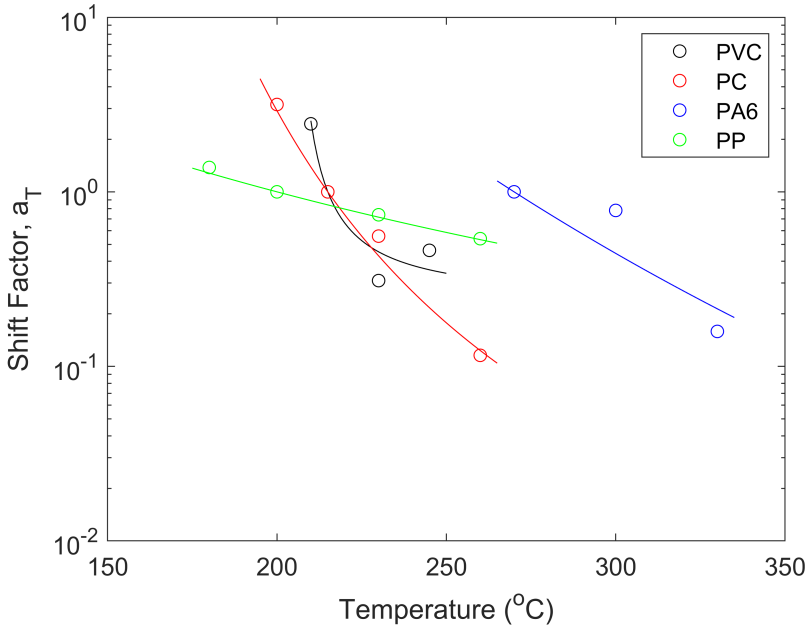

Figure 4.10: Shift factor for PVC, PC, PA6, and PP.

Figure 4.11 shows the master curve of the complex viscosity together with the Carreau-Yasuda model. The Carreau-Yasuda parameters were calculated using the Matlab curve fitting tool. The parameters for the model are shown in Table 4.9.

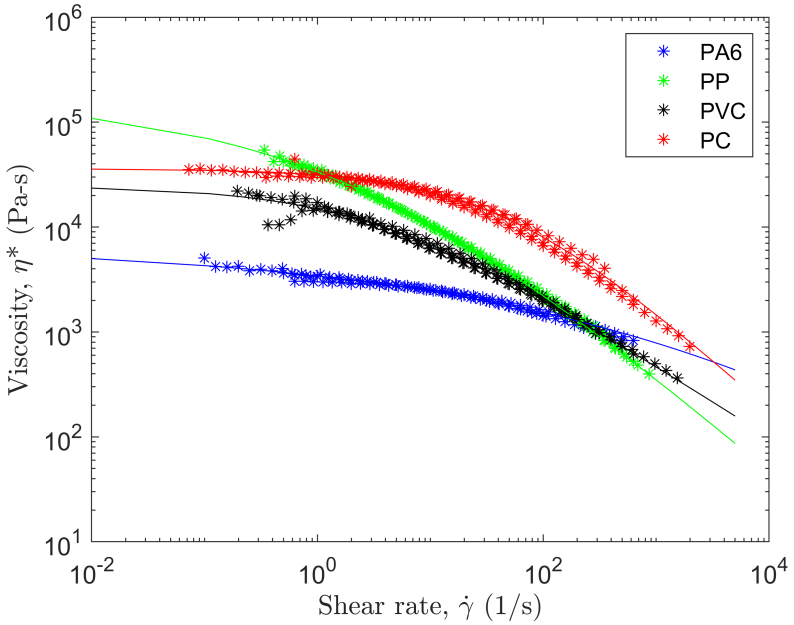

Figure 4.11: Master curve (shear rate dependent on complex viscosity as a function of temperature) for PVC, PC, PA6, and PP.

Table 4.9: Carreau - Yasuda Parameters

Material	Carreau-Yasuda Parameters				
	η_o (Pa-s)	λ (s)	a (-)	b (-)	R^2
PA6	6730	$2.536*10^{-5}$	0.188	$5.306*10^{-3}$	0.9850
PP	$1.65*10^5$	0.4697	0.3405	$5.149*10^{-2}$	0.9991
PVC	$2.462*10^4$	0.3952	0.5633	0.3138	0.9912
PC	$3.598*10^4$	0.02153	0.6195	$2.611*10^{-5}$	0.9912

Using the presented master curve allows for determining the viscosity within a range of shear rate and temperature. Therefore, the model will be of value when calculating the viscosity for the analytical models.

4.4.6 Experimental Results

CT Scan

Figure 4.12 shows the CT scan results of all the materials using a force of 56.456 N. A difference in the melting of both polymer structures is observed. The PA6 and PP, considered

semi-crystalline, show a defined melt film with no deformation of the material near the film. This result was expected. It is assumed that the melt film is formed and flows once the polymer reaches the melting temperature. The PC and PVC show a transition curve right above the melt film. The figures can be explained using the viscosity data shown in Figure 4.8. For the PA6 and PP material, it can be seen that there is a sharp decrease in viscosity right after the material reaches the melting temperature. For the PC and PVC, once the material reaches the glass transition temperature, there is a gradual softening or viscosity reduction. As the material can flow once it reaches T_g, it forms a transition in viscosity or curve as shown in Figure 4.12c and Figure 4.12d. As the material in contact with the hot surface is at a higher temperature, the viscosity is lower than the point where the material is at its T_g. As there is a gradient of temperature and subsequently a gradient in viscosity, the material creates a transition when flowing. To obtain an average melt film thickness, a total of 5 samples were scanned for each condition. Only one cross-section of each sample was analyzed, measuring the thickness at each side of the rod. The values reported in the following section are averages of 8 - 10 values.

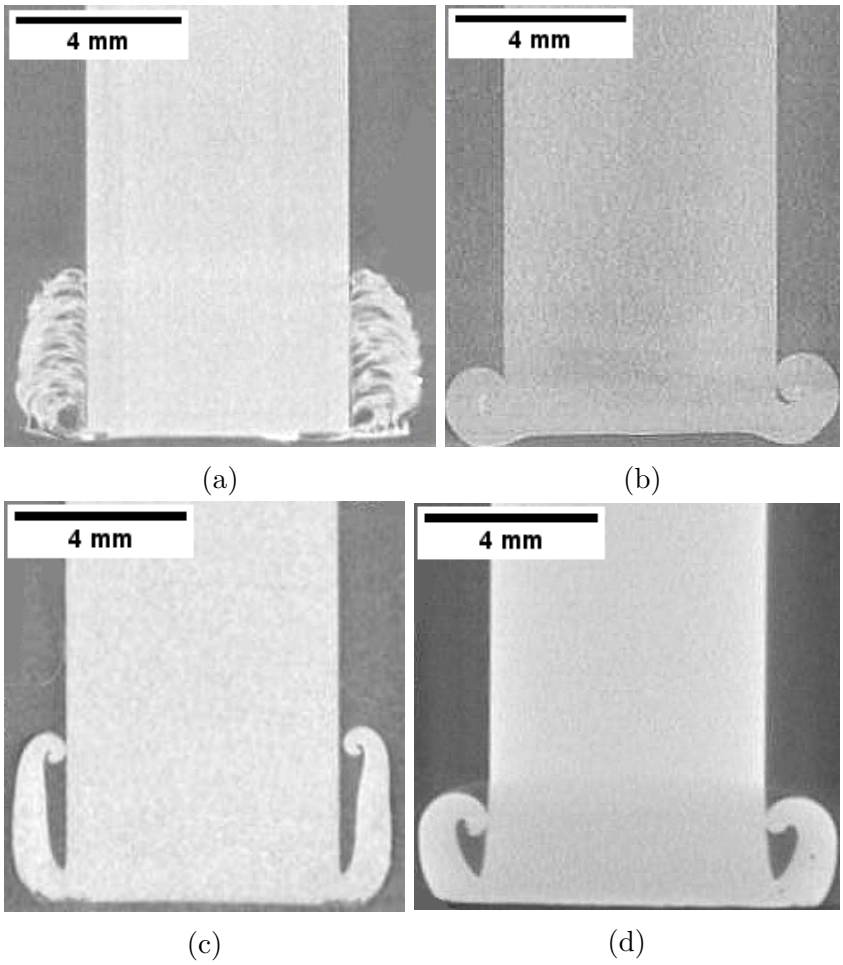

Figure 4.12: Computed tomography image of (a) PA6, (b) PP, (c) PC, and (d) PVC.

Effect of cooling rate. Force = 38.945 N

Figure 4.13 shows the melt film thickness comparison between cooling processes. As noted, there is not a significant difference between the cooling processes. For the annealing process, the melt film thickness was 0.24 mm, 0.85 mm, 0.82 mm, and 0.69 mm for PA6, PP, PC, and PVC. The melt film thickness was 0.28 mm, 0.84 mm, 0.78 mm, and 0.69 mm for PA6, PP, PC, and PVC for the quenching process. The significant standard deviation seen for some of the materials may be due to the experimental procedure. Moreover, even though the force was applied for 30 seconds, some tests may have taken a few seconds more to remove the sample from the heated surface entirely. Nonetheless, the magnitude of melt film thickness between both cooling processes is within the same range.

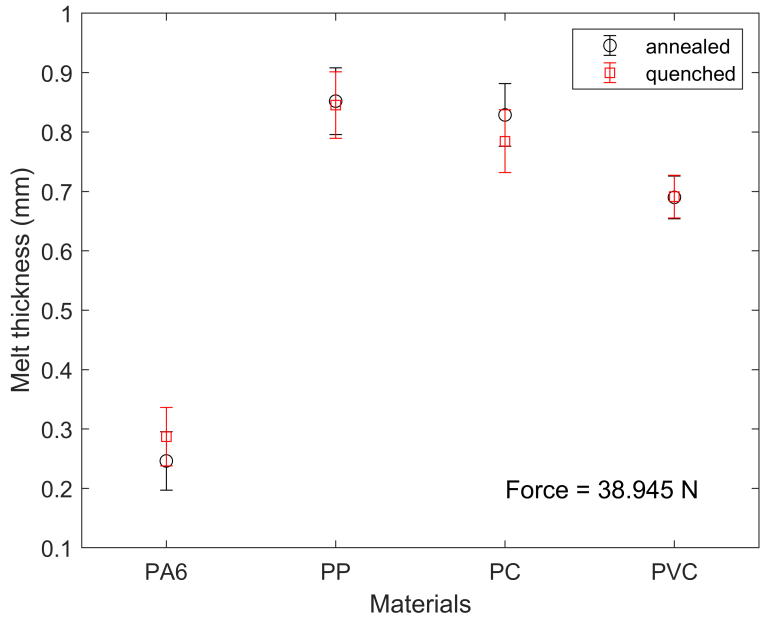

Figure 4.13: Melt film thickness comparison of cooling processes.

Force = 56.456 N

Figure 4.14 shows the comparison of melt film thickness for two different applied forces. It also shows the result using two different cooling processes for a force of 38.945 N. The experimental melt thickness for a force of 56.456 N is 0.644 mm for PVC, 0.708 mm for PC, 0.774 mm for PP, and 0.224 mm for Nylon.

Results are as expected. Increasing the filament force decreases the melt film thickness. This can be seen in the following way. Increasing the filament force also increases the filament velocity. Higher filament velocity makes the material near the hot surface flow radially at a higher rate. Subsequently, producing a lower melt film thickness. This flow results from the applied force exerted on the rod and the heat conduction from the hot surface to the

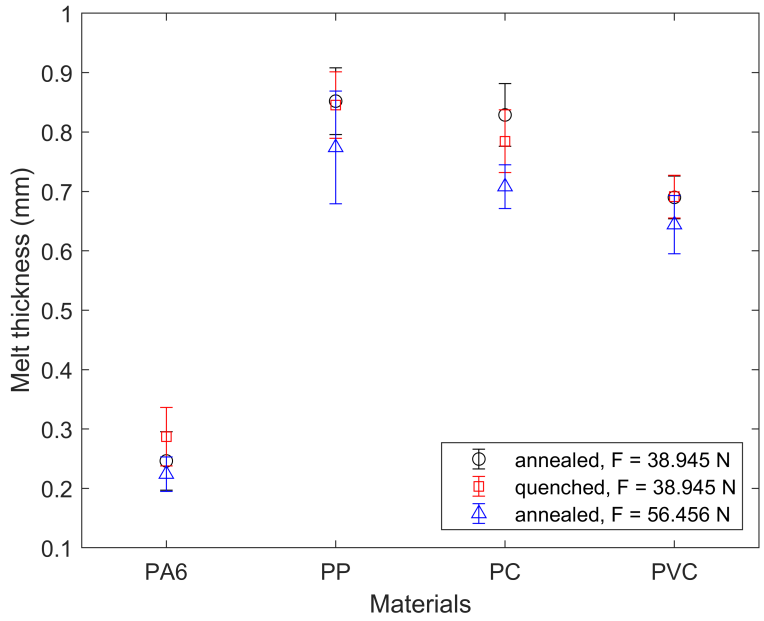

Figure 4.14: Melt film thickness comparison of PA6, PP, PC, and PVC using a two different forces.

rod. As the rod increases in temperature, the viscosity decreased, allowing the material to flow radially. The experimental results will be compared with the analytical models and numerical simulation for comparison purposes.

4.4.7 Analytical Model

During the calculation of the melt thickness, it is assumed that the melting temperature for the amorphous materials is T_g. For the semi-crystalline materials, the respective melting temperature is used. As it is assumed that the temperature gradient is lineal, the temperature of the melt film was taken as the average temperature between the melting temperature and the heater temperature ($T_{film} = \frac{T_h+T_m}{2}$). This temperature was used to calculate the viscosity of the melt film.

Figure 4.15 and Figure 4.16 show the analytical melt film thickness for a force of 38.945 N and 56.456 N, respectively. Both figures are comparing two heat transfer mechanisms. These are conduction as the only mechanism, and the other conduction and convection are mechanisms present during melting. As shown in the figures, the melt film thickness is smaller when using conduction and convection mechanisms. This phenomenon is expected as convection allows melting and removal of material when the melted polymer flows radially. Although the result is desired, the difference in mechanism is not as significant.

For this reason, the incorporation of convection is not as relevant during the computation of the process. Although it is crucial to account for all the heat transfer mechanisms during a process, it is up to the reader to choose which solution to use. For comparison purposes,

the existing solution which incorporates only the effect of conduction will be used.

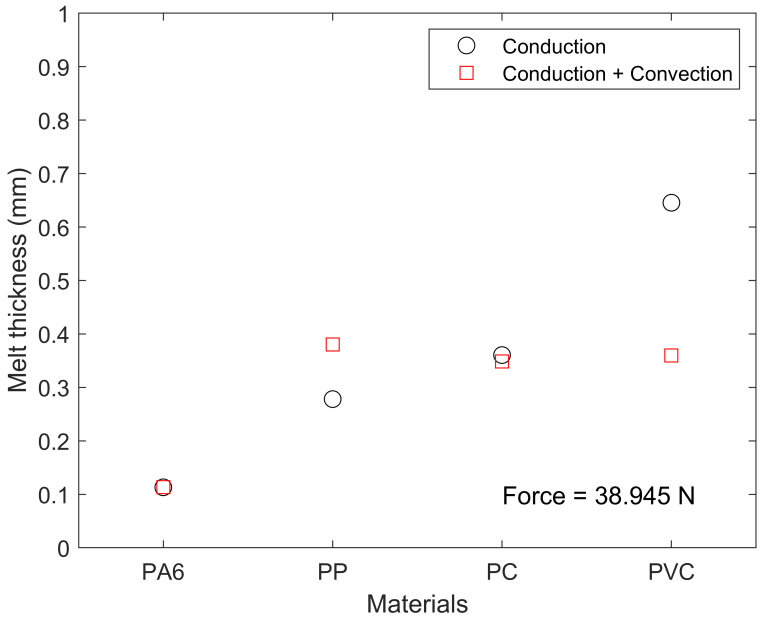

Figure 4.15: Analytical melt film thickness using a force of 38.94 N

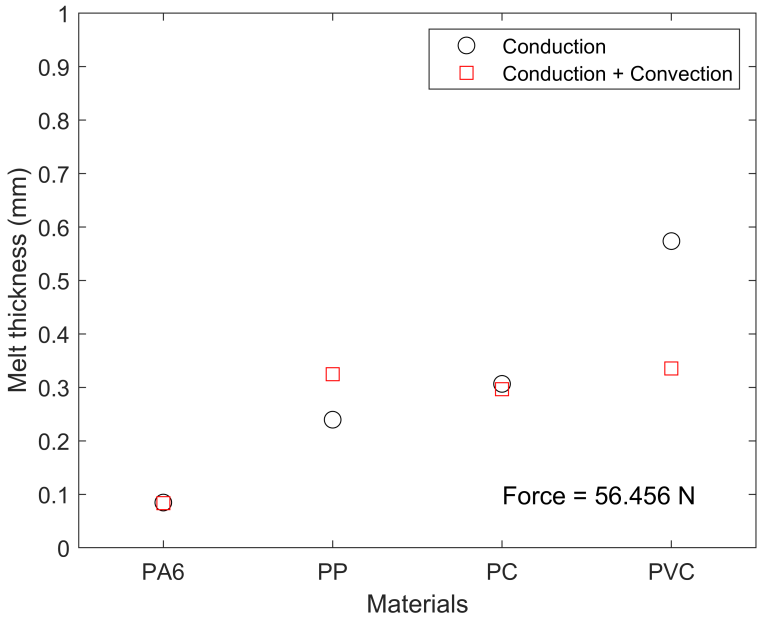

Figure 4.16: Analytical melt film thickness using a force of 56.45 N

4.4.8 Numerical Solution: COMSOL Multiphysics

COMSOL Multiphysics was used to calculate the numerical solution of the process. Boundary conditions, temperatures, and filament forces were used similar to the experimental procedure. For representation purposes, only the PVC results with a force of 56.456 N will be shown here. Figure 4.17 shows the volume fraction result for four different time steps. As seen in the figure, the evolution of the melt film thickness can be observed. Radial flow is achieved, which is comparable to the experimental results shown in Figure 4.12. During the pressure-induced melt removal process, the material is pushed towards the heated plate and melted. Later, the squeezing action causes the material to flow radially, as observed in the figure.

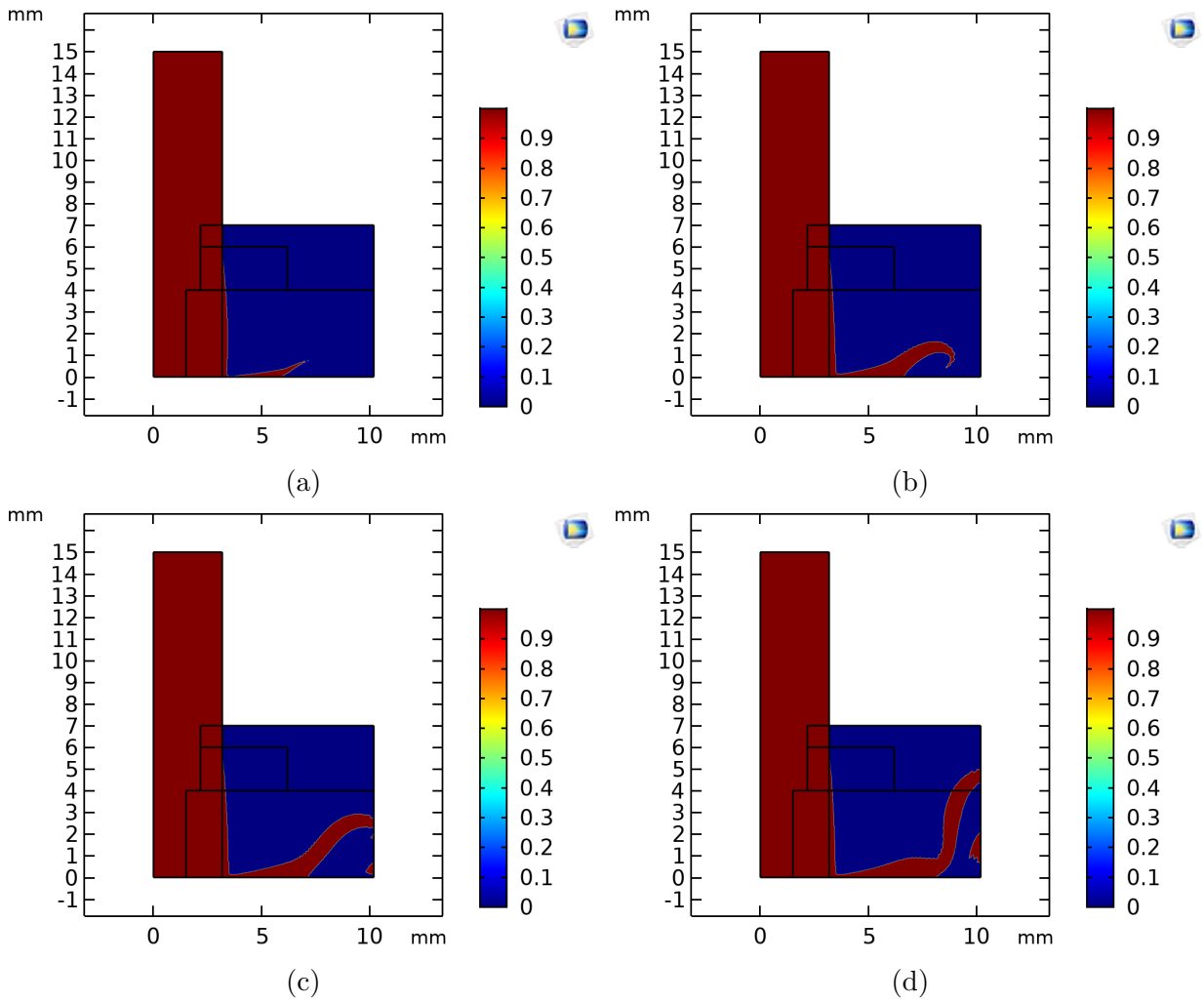

Figure 4.17: Transient COMSOL simulation results. Figure shows the volume fraction of PVC at a force of 56.456 N for (a) 7.5 sec, (b) 15 sec, (c) 22.5 sec, and (d) 30 sec.

Figure 4.18 shows the melting phase of the material. Here, a value of 1 denotes when the

material reaches the melting temperature, while zero indicates a solid material. The results obtained from Figure 4.18 will be used to compare with the analytical and experimental results. The reason behind this decision is that it is assumed that the material can flow once it reaches the melting temperature. However, the viscosity is high below this temperature, which does not allow flow during the respective conditions.

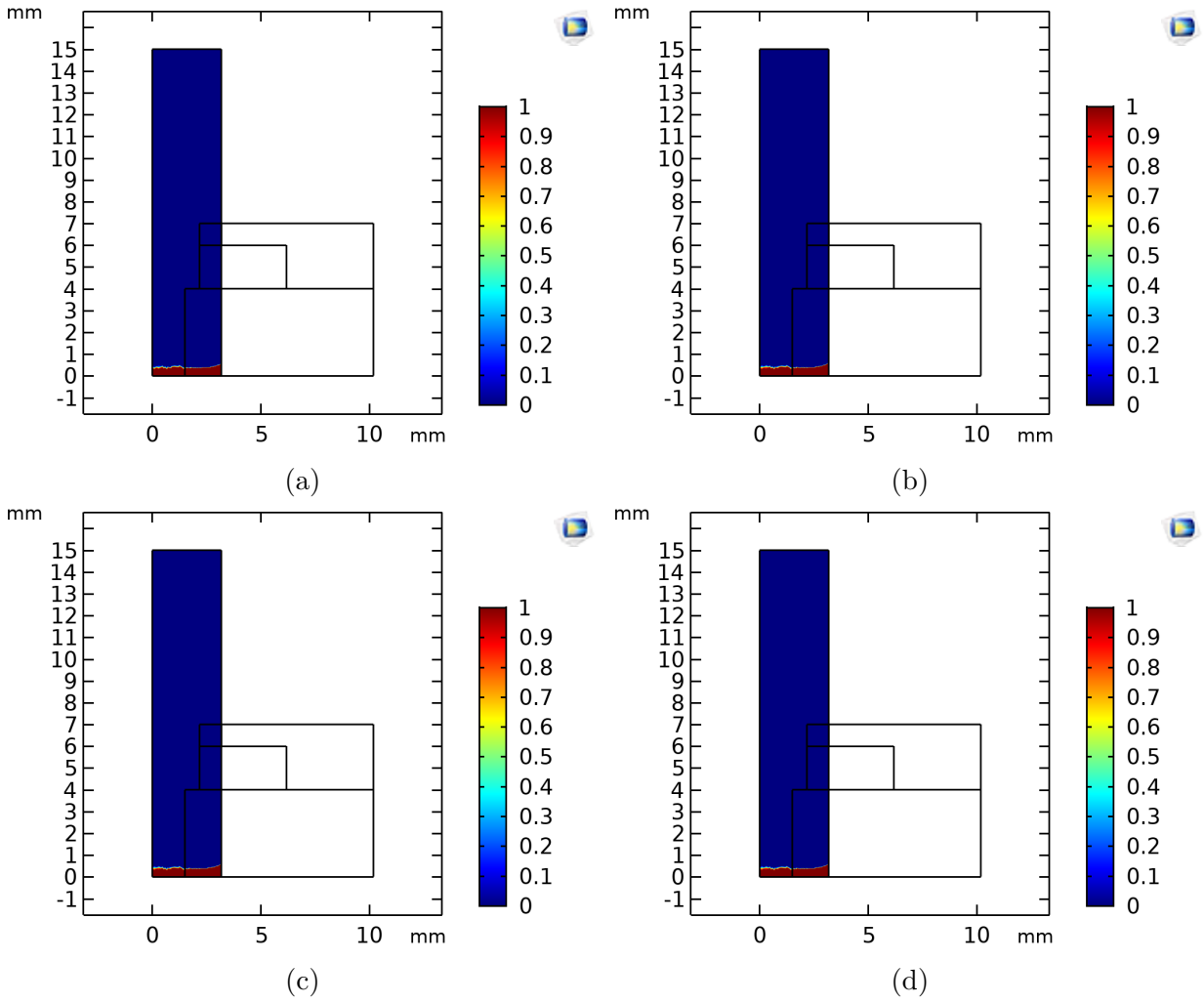

Figure 4.18: Transient COMSOL simulation results. Figure shows the melting region of PVC at a force of 56.456 N for (a) 7.5 sec, (b) 15 sec, (c) 22.5 sec, and (d) 30 sec.

Figure 4.19 shows the melt film thickness for both filament forces. The melt film thickness was measured from the heating surface to the solid-melt interface region. As seen in the figure, the higher the force, the smaller is the melt film thickness. These results were expected and can also be seen in the experimental results. For a force of 38.945 N, the melt film thickness values are 0.06 mm, 0.63 mm, 0.88 mm, and 1.12 mm for PA6, PP, PVC, and PC, respectively. At the same time, the results for a force of 56.456 N are 0.02 mm, 0.59 mm, 0.60 mm, and 1.22 mm, respectively.

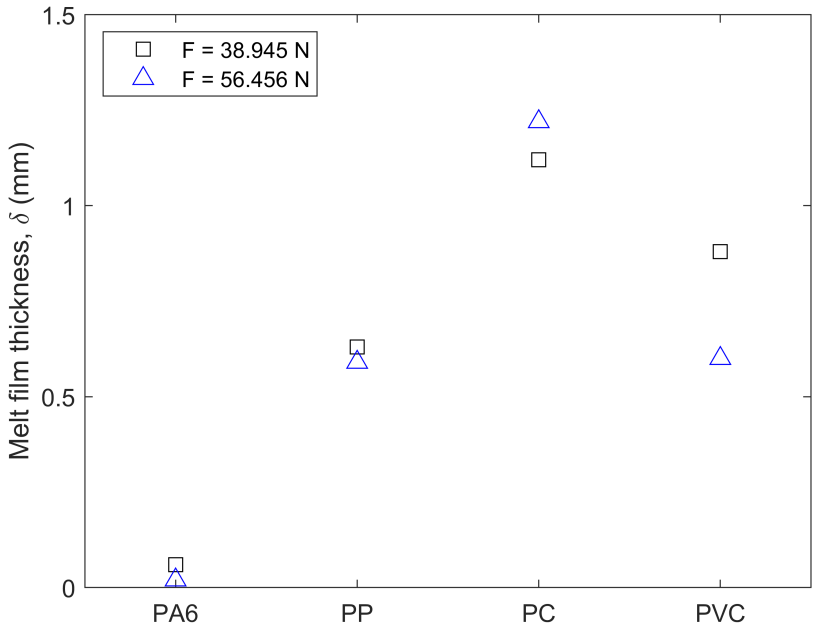

Figure 4.19: Melt film thickness for simulation results using the phase change feature

4.4.9 Comparison of Methods

Figure 4.20 and Figure 4.21 show the comparison of the melt film thickness. Here the experimental results are compared with the analytical solution and the numerical simulation. As observed, there is a discrepancy of results between methods for PP and PC material. For the PA6 and PVC, there is good accuracy of values within the different techniques. However, for PP and PC, the analytical and numerical methods are 50% of the experimental value. In the analytical approach, the solution depends on the mechanical properties and the rheological properties. Another reason for the discrepancy is the boundary conditions used, thermal effects present during the process, and the assumptions made during the solution of the analytical model.

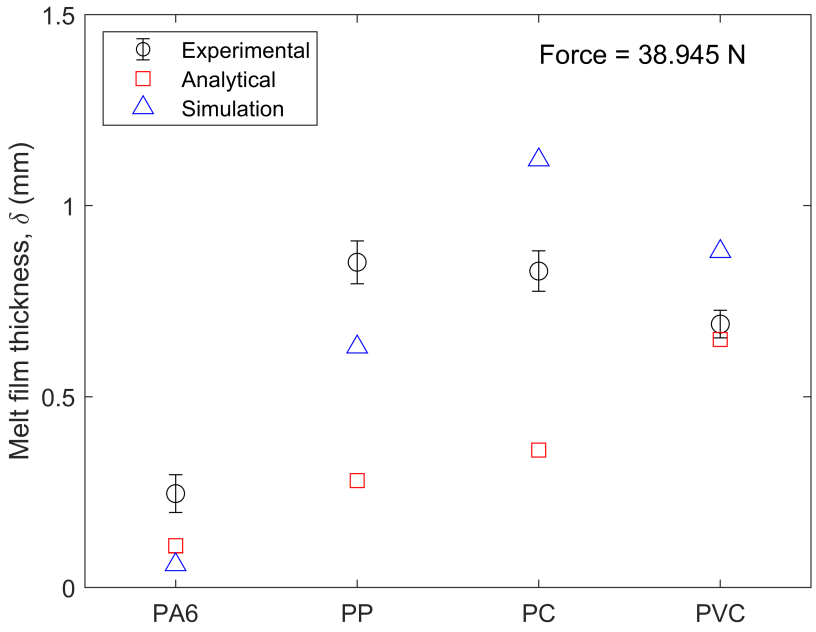

Figure 4.20: Melt film thickness comparison for a force of 38.945 N.

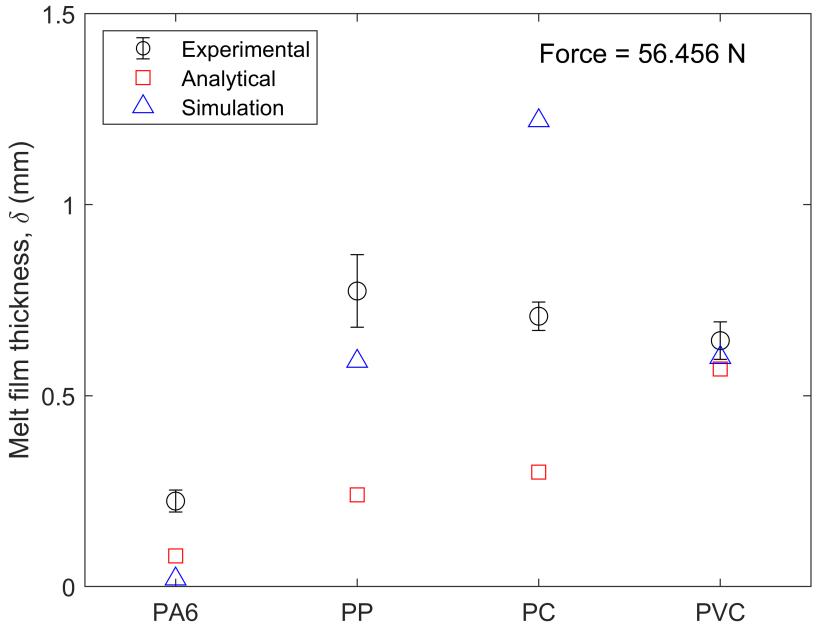

Figure 4.21: Melt film thickness comparison for a force of 56.456N.

The numerical method used here uses the phase-change feature within the heat transfer of fluid physic. The transition from solid to liquid is defined by the melting temperature and the transition interval between phases 1 and 2. Moreover, the latent heat of fusion is assigned to semicrystalline materials, which provide the heat necessary to achieve the melt state. A good approximation was achieved for both PVC and PA6. However, as the mechanical properties were found in literature, these may not represent the materials' actual properties and could be the reason for the PP and PC material discrepancy.

The experimental method could have included errors in the values obtained. For example, even though no resistance was felt when removing the rod with the aluminum foil, the technique employed here could have elated the melt thickness after removing the rod from contact with the heating plate. Also, due to manual labor, other sources of error could have arisen during the application of the force and its duration.

The accuracy of the solution arises from the premise of knowing the melting temperature of a thermoplastic material. This is a topic widely investigated even today. The determination for some polymers is precise due to their structured composition. Due to the molecular structure of polymers, they need to reach a specific temperature for the molecules to allow deformation, and subsequently, flow. However, these materials are not 100 % crystalline. This allows for the non-crystalline molecules to deform below the melting temperature for the semi-crystalline materials. Because of the results obtained, it is shown that the assumptions used for the amorphous materials ($T_m = T_g$) are a correct assumption and will be used throughout the work presented here.

4.5 Conclusion

The results presented here to aid in understanding the effect of the melting temperature for both amorphous and semi-crystalline polymers. The fundamental work valid the pressured-induce melt removal process developed by Stammers and Beek [53]. Moreover, the results shine a light on the melting process during the fused filament fabrication (FFF) process. The curvature formation above the amorphous materials' melt film confirms that flow is possible before reaching a melt state. This is a direct result of the gradient in temperature and subsequently gradient in viscosity.

As the filament material is enclosed within a heated nozzle, radiation and heat transfer will occur from the heated walls to the filament material. As the material is fed towards the heated nozzle, contact with the nozzle will occur. Subsequently, a melt film thickness will be formed, varying as a filament force and filament velocity function. The higher the filament velocity, the smaller the melt film thickness will be. The results allow for the understanding of the melting process during the FFF process.

This solution is helpful if it is assumed that there is no heat transfer from the ambient to the filament material. For this reason, it is believed that the assumptions made by Osswald et al. [1] on their FFF melting model are valid. Therefore, the idea will be explored in the following section by improving the current Osswald et al. model [1] and verifying the accuracy of the results using the respective assumptions and parameters.

5. Implementation of shear thinning behavior in the fused filament fabrication melting model: analytical solution and experimental validation

Fused Filament Fabrication (FFF) has been at the forefront of Additive Manufacturing (AM) due to low costs, the ability to manufacture complex geometries, and the broad availability of AM machines in the market. Various theoretical models have been proposed to explain the melting behavior of the polymer filament in the FFF process. The most prevalent model involves the formation of a pool of polymer melt at the nozzle that is pushed out of the orifice by the solid filament acting as a piston [18]. An alternative model that suggests forming a melt film, with thickness varying as a function of the force exerted by the solid filament, is used as the basis for this work. This model, known as the "Fused Filament Fabrication melting model," was proposed by Osswald et al. [1] and assumes a Newtonian fluid, which is a simplification of the actual rheological behavior of polymeric melts. This work aims to improve this model by implementing the shear-thinning behavior of the material into the equations. The analytical solution of the shear-thinning model is compared to models found in the literature using experimental data at different printing conditions. By comparing these models, it was shown that the implementation of shear-thinning effects enhances the prediction of the melting behavior of the filament material at both low and high printing temperatures using the corresponding assumptions.

5.1 Introduction

Fused Filament Fabrication (FFF) has been at the forefront of Additive Manufacturing (AM) due to the low cost of machines and materials, the ability to manufacture complex geometries, and the broad availability of AM machines in the market. The FFF process has gained popularity in the last decade due to design freedom from fabricating complex geometries previously unattainable. During the manufacture of an object, the material is molten and extruded through a heated nozzle. As a result of the material extrusion, neighboring beads are fused in a diffusion dominant welding process [2]. This process is repeated layer by layer

until the object is entirely manufactured, as depicted in Figure 5.1a. Because the building process requires a layer by layer structure, the time required to print an object increases with decreasing nozzle diameter and layer height [3].

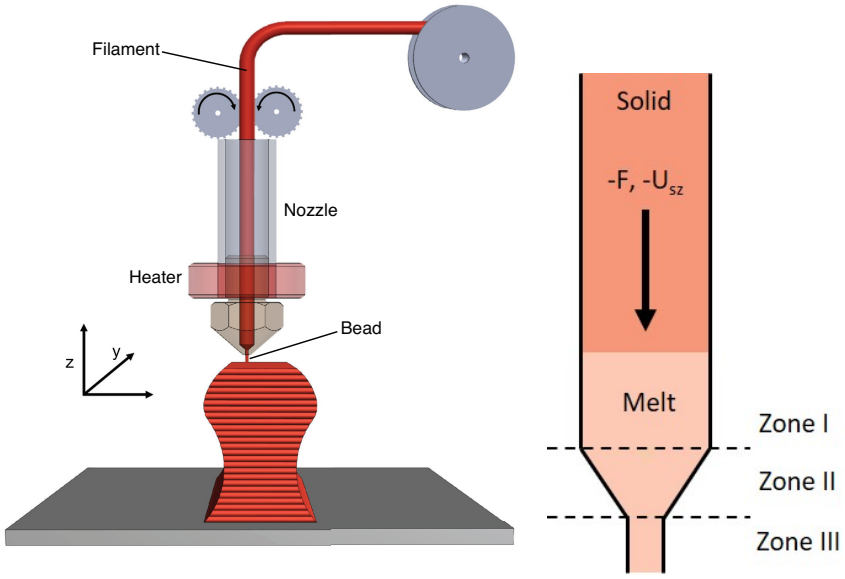

(a) (b)

Figure 5.1: Schematic of (a) FFF Process and (b) Bellini's assumption [18].

The melting behavior of the filament in the FFF process has been of significant interest in the past years [18–21]. As with any industrial revolution, high flow rates are needed to maximize throughput. To prevent under extrusion [81] or nozzle clogging, a model in the limit of high flow rates are desirable.

Various models exist to explain the melting behavior of the filament. The model proposed by Bellini et al. [18] assumes that melting of the filament material takes place right after the material enters the nozzle. This is the case only in the limit of low flow rates. This assumption has been used widely by many [19–21], using the solid filament as a plunger to push the melted polymer through the nozzle generating the bead. A schematic of this process is shown in Figure 5.1b. It is essential to mention that the assumption of buckling of the filament material and melt backflow was not considered in these works. The upper-bound estimate proposed by Luo et al. [22] takes a heat transfer approach by solving a Graetz-Nusselt problem. Their work focuses on the boundary between the solid and molten polymer in the heated portion of the tube. Here, the solution is an upper bound estimate and a semi-empirical model as the threshold temperature is measured. Recently, Serdeczny et al. [82] developed a numerical solution that accounts for the re-circulation of polymer melt inside the nozzle. Under specific conditions, they found that melting of the filament occurs only at the surface of the contraction section of the printing nozzle, which is similar to the analytical model derived by Osswald et al. [1] and the work presented herein. Other authors have taken the task to measure the force accurately, and filament velocity during

printing [6, 23–26]. By incorporating a force sensor, the force can be measure in real-time. Also, by including an encoder, the velocity at which the filament is fed can be measured. Recently, a new approach has been developed to explain the melting behavior of the filament in a FFF process. This approach, known as the "Fused Filament Fabrication Melting Model" was proposed by Osswald et al. [1] in 2018. It incorporates the formation of a melt film that varies as a function of the force exerted by the solid filament and neglects radial heat transfer. This is the extreme of running the FFF-printer at high flow rates as the material has effectively no time to melt while traveling through the nozzle. It also assumes a Newtonian fluid for the material, which simplifies the actual rheological behavior of polymeric melts. Apart from Luo's semi-empirical upper-bound estimate, all models apply only in the regime of low flow rates [18–21].

This work is based on the approach proposed by Osswald et al. The FFF model is improved by incorporating the shear-thinning behavior of polymeric materials using the power-law model to simulate the viscosity of these materials. Also, the deviatoric stress is taken into account for the calculation of the filament force. The assumptions, boundary conditions, and derivations will be shown in this paper, and results will be compared using the mentioned models from the literature. Furthermore, an FFF printer produced by FusedForm Corp. (Bogotá, Colombia) was modified by incorporating a force sensor above the print-head capturing real-time force measurements. In addition, an encoder and thermistor collect filament length and temperature data as a function of time. The data obtained was used to compare the models at different printing temperatures and using different materials.

5.2 Mathematical Model

As stated by Osswald et al. [1], the mathematical model is derived in a tilted cylindrical coordinate system to account for the nozzle angle, α, as depicted in Figure 5.2b. This model assumes melting with pressure flow removal [10, 42] so that the solid filament is pushed towards the heated nozzle with force F_z. No radial heat transfer is considered during the derivation of the model. It is also assumed that backflow does not occur during the process. Once the steady-state condition is reached, using a force $-F_z$, a melt film thickness δ is created at the nozzle-filament interface as shown in Figure 5.2a. This melt film thickness, which is unknown, varies with the magnitude of the force exerted on the solid filament. The derivation presented here assumes a shear-thinning material. Therefore the power-law model is used in the equations rendering the momentum equation non-linear. This equation can be solved for the filament velocity given a force, while the solution will depend on the power-law model parameters. The temperature of the melt-solid interface is defined as T_m, which is the temperature at which the filament melts. When dealing with semi-crystalline polymers, the heat of fusion λ is needed to melt the crystallites [32]. When the solid filament is subjected to a force $-F_{sz}$, it moves at a vertical velocity $-U_{sz}$. When deriving the melting model, it is assumed that the filament velocity (U_{sz}) is known, solving for the filament force (F_z) and the melt film thickness.

5.2.1 Geometric Description and Boundary Conditions

The equations are derived in a tilted coordinate domain to simplify the geometrical representation as shown in Figure 5.2.

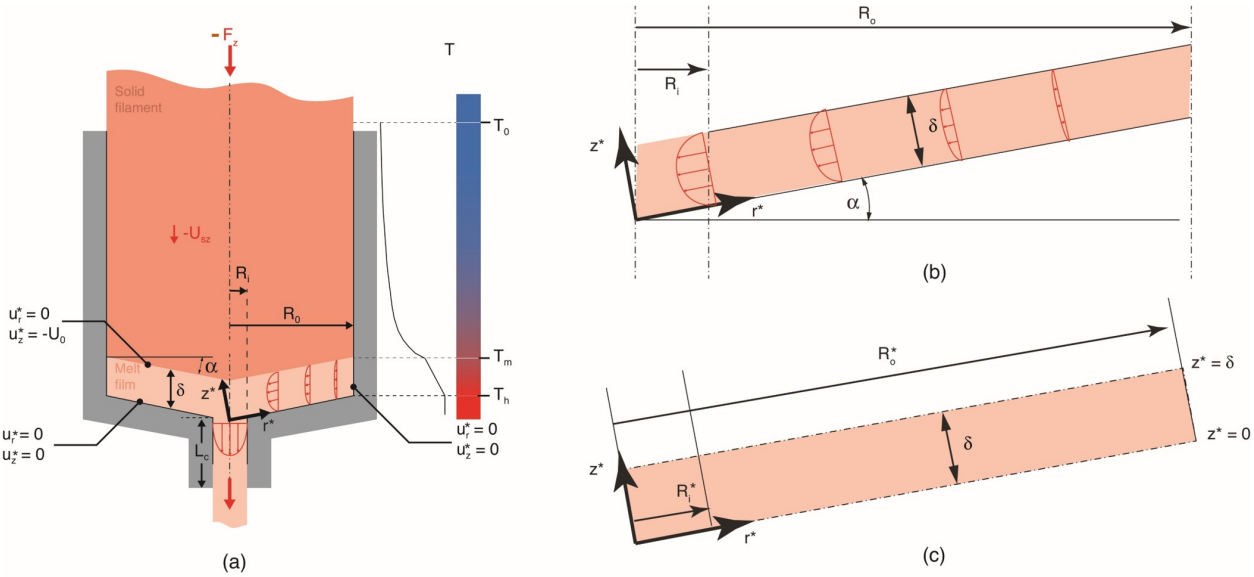

Figure 5.2: Schematic of (a) melting mechanism, (b) the new tilted or transformed coordinate system $r^* - z^*$, and (c) boundary conditions.

The relationship between the tilted $(r^* - z^*)$ domain and non-tilted $(r - z)$ domain is given by Equation 5.1.

$$u_r^* = u_r cos(\alpha) \tag{5.1a}$$

$$r^* = \frac{r}{cos(\alpha)} \tag{5.1b}$$

$$R_o^* = \frac{R_o}{cos(\alpha)} \tag{5.1c}$$

$$R_i^* = \frac{R_i}{cos(\alpha)} \tag{5.1d}$$

To model the melt flow behavior inside the nozzle, the following boundary conditions are applied.

$$u_r^* = 0 \quad \text{at} \quad z^* = 0 \tag{5.2a}$$

$$u_r^* = 0 \quad \text{at} \quad z^* = \delta \tag{5.2b}$$

$$u_z^* = 0 \quad \text{at} \quad z^* = 0 \tag{5.2c}$$

$$u_z^* = (-U_o)\cos\alpha \quad \text{at} \quad z^* = \delta \tag{5.2d}$$

$$u_r^* = 0 \quad \text{at} \quad r^* = R_o^* \tag{5.2e}$$

$$p = p_i \quad \text{at} \quad r = R_i^* \tag{5.2f}$$

The first three boundary conditions and the fifth result from the no-slip condition at the walls of the FFF nozzle. The fourth boundary condition represents the filament velocity at the solid-melt interface. Finally, the last boundary condition is the inlet pressure (p_i) at the entrance of the capillary zone.

5.2.2 Governing Equations

Considering that the filament travels vertically and that it does not rotate, the continuity equation reduces to Equation 5.3.

$$\frac{1}{r^*}\frac{\partial}{\partial r^*}(r^* u_r^*) + \frac{\partial u_z^*}{\partial z^*} = 0 \tag{5.3}$$

The melt film's order of magnitude analysis has been performed to identify the predominant terms in the momentum equations. This analysis was conducted under the assumption of pressure-induced melt removal [42] (non-tilted coordinate system), which is the concept behind this model. Results of the order of magnitude analysis can be observed in Equations 5.4a-5.4d.

$$\frac{\partial v_r}{\partial z} = \frac{U_o R_o}{\delta^2} \tag{5.4a}$$

$$\frac{\partial v_r}{\partial r} = \frac{U_o}{\delta} \tag{5.4b}$$

$$\frac{\partial v_z}{\partial z} = \frac{U_o}{\delta} \tag{5.4c}$$

$$\frac{\partial v_z}{\partial r} = \frac{U_o}{R_o} \tag{5.4d}$$

Assuming that the melt film is small compared to the filament radius ($\delta \ll R_o$), it can be shown that the predominant term is the velocity gradient $\frac{\partial v_r}{\partial z}$. Also, with this estimate, it can be shown that the terms in the continuity equation have the same magnitude. With this, the momentum equations are reduced to Equations 5.5a - 5.5c.

$$\text{r-component} \quad 0 = -\frac{\partial p}{\partial r^*} + \frac{\partial}{\partial z^*}\left(\tau_{zr}^*\right) \tag{5.5a}$$

$$\theta\text{-component} \quad 0 = \frac{\partial p}{\partial \theta} \tag{5.5b}$$

$$\text{z-component} \quad 0 = \frac{\partial p}{\partial z^*} \tag{5.5c}$$

Equations 5.5a - 5.5c tell us that the pressure can be approximated as a function of the r^* component alone.

5.3 Mathematical Derivation

Starting with the momentum equations in the r-component, the power law model is substituted in Equation 5.5a which results in Equation 5.6.

$$0 = -\frac{\partial p}{\partial r^*} + \frac{\partial}{\partial z^*}\left(\tau_{zr}^*\right), \quad \tau_{zr}^* = m_f \left|\frac{du_r^*}{dz^*}\right|^{n-1} \frac{du_r^*}{dz^*} \tag{5.6}$$

where m_f is the consistency index of the melt film and n is the power law index. Equation 5.6 is integrated with respect to z and solved for the velocity gradient using $\frac{\partial v_r^*}{\partial z^*} = 0$ at $z^* = \frac{\delta}{2}$ resulting in Equation 5.7.

$$\left|\frac{du_r^*}{dz^*}\right|^{n-1} \frac{\partial v_r^*}{\partial z^*} = \frac{1}{m_f}\frac{\partial p}{\partial r^*}\left(z^* - \frac{\delta}{2}\right) \tag{5.7}$$

Two cases have to be distinguished in Equation 5.7. The first corresponds to a negative slope of the velocity gradient ($\frac{\partial v_r^*}{\partial z^*} \leq 0$), and the second corresponds to a positive slope of the velocity gradient ($\frac{\partial v_r^*}{\partial z^*} \geq 0$). A schematic of both cases is shown in Figure 5.3.

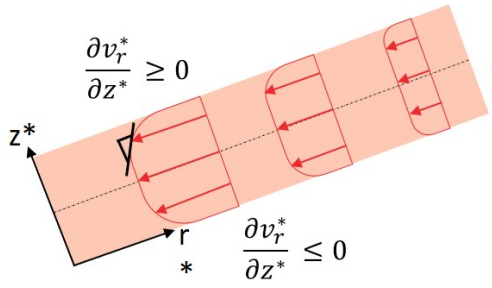

Figure 5.3: Schematic of velocity (red) and velocity gradient (black line) inside the FFF nozzle.

The solution of both cases are shown in Equation 5.8a and 5.8b which yields the velocity gradient for both scenarios.

$$\frac{\partial v_r^*}{\partial z^*} \leq 0, \qquad \frac{du_r^*}{dz^*} = -\left(\frac{1}{m_f}\frac{\partial p}{\partial r^*}\right)^{\frac{1}{n}}\left(\frac{\delta}{2} - z^*\right)^{\frac{1}{n}} \tag{5.8a}$$

$$\frac{\partial v_r^*}{\partial z^*} \geq 0, \qquad \frac{du_r^*}{dz^*} = \left(\frac{1}{m_f}\frac{\partial p}{\partial r^*}\right)^{\frac{1}{n}}\left(z^* - \frac{\delta}{2}\right)^{\frac{1}{n}} \tag{5.8b}$$

Integrating both terms by using the boundary condition $v_r^* = 0$ at $z^* = 0$ and $v_r^* = 0$ at $z^* = \delta$, the velocity equation results in Equation 5.9a and 5.9b.

$$\frac{\partial v_r^*}{\partial z^*} \leq 0, \qquad u_r^* = \left(\frac{n}{n+1}\right)\left(\frac{1}{m_f}\frac{\partial p}{\partial r^*}\right)^{\frac{1}{n}}\left[\left(-z^* + \frac{\delta}{2}\right)^{\frac{n+1}{n}} - \left(\frac{\delta}{2}\right)^{\frac{n+1}{n}}\right] \tag{5.9a}$$

$$\frac{\partial v_r^*}{\partial z^*} \geq 0, \qquad u_r^* = \Big(\frac{n}{n+1}\Big)\Big(\frac{1}{m_f}\frac{\partial p}{\partial r^*}\Big)^{\frac{1}{n}}\Big[\Big(z^* - \frac{\delta}{2}\Big)^{\frac{n+1}{n}} - \Big(\frac{\delta}{2}\Big)^{\frac{n+1}{n}}\Big] \tag{5.9b}$$

These two equations are substituted individually into the continuity equation (Equation 5.3). Integrating both expression with respect to z^* using the boundary condition $v_z^* = 0$ at $z^* = 0$ and equating both for the crossover point ($z^* = \frac{\delta}{2}$) results in Equation 5.10a and 5.10b.

$$\frac{\partial v_r^*}{\partial z^*} \leq 0, \qquad v_z^* = -\frac{1}{r^*}\Big(\frac{n}{n+1}\Big)\Big(\frac{1}{m_f}\Big)^{\frac{1}{n}}\frac{\partial}{\partial r^*}\Big(r^*\frac{\partial p}{\partial r^*}^{\frac{1}{n}}\Big)$$
$$\Big[-\Big(\frac{1}{2n+1}\Big)\Big(-z^* + \frac{\delta}{2}\Big)^{\frac{2n+1}{n}} - \Big(\frac{\delta}{2}\Big)^{\frac{n+1}{n}} z^* + \Big(\frac{n}{2n+1}\Big)\Big(\frac{\delta}{2}\Big)^{\frac{2n+1}{n}}\Big] \tag{5.10a}$$

$$\frac{\partial v_r^*}{\partial z^*} \geq 0, \qquad v_z^* = -\frac{1}{r^*}\Big(\frac{n}{n+1}\Big)\Big(\frac{1}{m_f}\Big)^{\frac{1}{n}}\frac{\partial}{\partial r^*}\Big(r^*\frac{\partial p}{\partial r^*}^{\frac{1}{n}}\Big)$$
$$\Big[\Big(\frac{1}{2n+1}\Big)\Big(z^* - \frac{\delta}{2}\Big)^{\frac{2n+1}{n}} - \Big(\frac{\delta}{2}\Big)^{\frac{n+1}{n}} z^* + \Big(\frac{n}{2n+1}\Big)\Big(\frac{\delta}{2}\Big)^{\frac{2n+1}{n}}\Big] \tag{5.10b}$$

Using the boundary condition $v_z^* = -U_o cos(\alpha)$ at $z^* = \delta$ in Equation 5.10b, an expression for the pressure gradient can be found as shown in Equation 5.11. Equation 5.10b is used since it is the equation that predicts the velocity at the mentioned boundary condition.

$$\frac{\partial v_r^*}{\partial z^*} \geq 0, \qquad \Big(\frac{\partial p}{\partial r^*}\Big)^{\frac{1}{n}} = (-U_o)cos(\alpha)\Big(\frac{1}{m_f}\Big)^{-\frac{1}{n}}\Big(\frac{2n+1}{4n}\Big)\Big(\frac{\delta}{2}\Big)^{-\frac{2n+1}{n}} r^* + \frac{C_4}{r^*} \tag{5.11}$$

Substituting the pressure gradient back into Equation 5.9a and 5.9b, and using the boundary condition $v_r^* = 0$ at $r^* = R_o^*$ the constant C_4 can be found as shown in Equation 5.12.

$$C_4 = (U_o)cos(\alpha)\Big(\frac{1}{m_f}\Big)^{-\frac{1}{n}}\Big(\frac{2n+1}{4n}\Big)\Big(\frac{\delta}{2}\Big)^{-\frac{2n+1}{n}} R_o^{*2} \tag{5.12}$$

Substituting back gives Equation 5.13a and 5.13b.

$$\frac{\partial v_r^*}{\partial z^*} \leq 0, \qquad u_r^* = (-U_o)cos(\alpha)\Big(\frac{2n+1}{4(n+1)}\Big)\Big(\frac{\delta}{2}\Big)^{-\frac{2n+1}{n}}\Big[\Big(-z^* + \frac{\delta}{2}\Big)^{\frac{n+1}{n}} - \Big(\frac{\delta}{2}\Big)^{\frac{n+1}{n}}\Big]\Big(r^* - \frac{R_o^{*2}}{r^*}\Big) \tag{5.13a}$$

$$\frac{\partial v_r^*}{\partial z^*} \geq 0, \qquad u_r^* = (-U_o)cos(\alpha)\Big(\frac{2n+1}{4(n+1)}\Big)\Big(\frac{\delta}{2}\Big)^{-\frac{2n+1}{n}}\Big[\Big(z^* - \frac{\delta}{2}\Big)^{\frac{n+1}{n}} - \Big(\frac{\delta}{2}\Big)^{\frac{n+1}{n}}\Big]\Big(r^* - \frac{R_o^{*2}}{r^*}\Big) \tag{5.13b}$$

Substituting Equation 5.12 into the pressure gradient results in Equation 5.14.

$$\frac{\partial p}{\partial r^*} = \Big[U_o cos(\alpha)(m_f)^{\frac{1}{n}}\Big(\frac{2n+1}{4n}\Big)\Big(\frac{\delta}{2}\Big)^{-\frac{2n+1}{n}}\Big]^n\Big(\frac{R_o^{*2}}{r^*} - r^*\Big)^n \tag{5.14}$$

Integrating Equation 5.14 with respect to r^* using the boundary condition $p = p_i$ at $r^* = R_i^*$ results in the pressure as shown in Equation 5.15.

$$\begin{aligned} p = \Big[U_o cos(\alpha)(m_f)^{\frac{1}{n}}\frac{2n+1}{4n}\Big(\frac{\delta}{2}\Big)^{-\frac{2n+1}{n}}\Big]^n \frac{R_o^{*2n}}{1-n}\Big[r^{*1-n}{}_2F_1[\frac{1-n}{2}, -n, 1+\frac{1-n}{2}, \frac{r^{*2}}{R_o^{*2}}] \\ - R_i^{*1-n}{}_2F_1[\frac{1-n}{2}, -n, 1+\frac{1-n}{2}, \frac{R_i^{*2}}{R_o^{*2}}]\Big] + p_i \end{aligned} \tag{5.15}$$

Where the value of p_i is shown in Equation 5.16. Derivation of p_i is shown in detail in the appendix.

$$p_i = 2m_c L_c\left[\frac{3n+1}{n}\frac{U_o R_o^2}{R_i^{\frac{3n+1}{n}}}\right]^n \tag{5.16}$$

Transforming back the pressure term into the non-tilted domain results in Equation 5.17.

$$\begin{aligned} p = \frac{1}{cos(\alpha)}\Big[U_o\Big(m_f\Big)^{\frac{1}{n}}\frac{2n+1}{4n}\Big(\frac{\delta}{2}\Big)^{-\frac{2n+1}{n}}\Big]^n \frac{R_o^{2n}}{1-n}\Big[r^{1-n}{}_2F_1[\frac{1-n}{2}, -n, 1+\frac{1-n}{2}, \frac{r^2}{R_o^2}] \\ - R_i^{1-n}{}_2F_1[\frac{1-n}{2}, -n, 1+\frac{1-n}{2}, \frac{R_i^2}{R_o^2}]\Big] + p_i \end{aligned} \tag{5.17}$$

Besides the contribution of the pressure on the filament force, the deviatoric stress (τ) at the wall has to be known. Stemming from the order of magnitude analysis and the model assumptions, τ reduces to the shear stress by using the gradient in the upward direction ($\frac{\partial v_r}{\partial z} \geq 0$). The shear stress in the non-tilted coordinates is given by Equation 5.18.

$$\tau_{rz}(z=\delta) = \tau = m_f\Big(U_o\frac{2n+1}{n}\delta^{-2}(\frac{R_o^2}{r} - r)\Big)^n \tag{5.18}$$

By performing a force balance analysis and taking the force component of each stress (pressure and deviatoric) on the filament, the contribution of each stress on the force is calculated using Equation 6.17. Since the filament is axisymmetric, all forces acting in the horizontal direction (in non-tilted coordinates) cancel each other out. A schematic of the force balance is shown in Figure 5.4.

$$F_{sz} = \vec{F_p}\cos\alpha - \vec{F_\tau}\sin\alpha \tag{5.19}$$

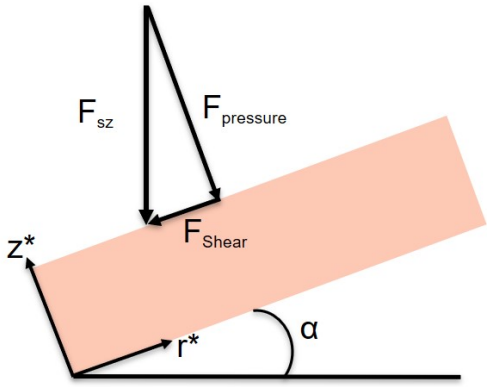

Figure 5.4: Schematic of the force components.

With this equation, it is demonstrated that when the nozzle has an angle of 0^o, the only component of the force is the pressure. As the angle increases, the contribution of the pressure decreases while the contribution of the deviatoric stress increases. Both forces can be calculated by integrating over the cross-section at the melt-solid interface. As a form of simplification, we assumed that in the inlet region ($r < R_i$), the pressure equals the inlet pressure, and the deviatoric stress is zero. With this, the force for the pressure component and the deviatoric stress component is calculated using Equation 5.20a and 5.20b respectively.

$$F_p = 2\pi \int_0^{R_o} prdr \tag{5.20a}$$

$$F_\tau = 2\pi \int_{R_i}^{R_o} \tau rdr \tag{5.20b}$$

A simplified version of the pressure term is shown in Equation 5.21.

$$p = \frac{1}{cos(\alpha)}\Big[U_o\Big(m\Big)^{\frac{1}{n}}\frac{2n+1}{4n}\Big(\frac{\delta}{2}\Big)^{-\frac{2n+1}{n}}\Big]^n \frac{R_o^{2n}}{1-n}\Big(r^{*1-n}{}_2F_1[\frac{1-n}{2}, -n, 1+\frac{1-n}{2}, \frac{r^2}{R_o^2}]- R_i^{*1-n}{}_2F_1[\frac{1-n}{2}, -n, 1+\frac{1-n}{2}, \frac{R_i^2}{R_o^2}]\Big) + 2m_cL_c\left[\frac{3n+1}{n}\frac{U_oR_o^2}{R_i^{\frac{3n+1}{n}}}\right]^n \tag{5.21}$$

Solving each integral individually and substituting back results in Equation 6.18 and Equation 6.19.

$$F_p = \frac{2\pi}{cos(\alpha)}\Big[U_o\Big(m\Big)^{\frac{1}{n}}\Big(\frac{2n+1}{4n}\Big)\Big(\frac{\delta}{2}\Big)^{-\frac{2n+1}{n}}\Big]^n \frac{R_o^{2n}}{1-n}$$
$$\Big(\frac{\Gamma(\frac{3-n}{2})}{2\Gamma(\frac{5-n}{2})}\Big[R_o^{3-n}\frac{\Gamma(\frac{5-n}{2})\Gamma(2+n)}{\Gamma(\frac{5+n}{2})} - R_i^{3-n}{}_2F_1[\frac{1-n}{2}, -n, \frac{5-n}{2}, \frac{R_i^2}{R_o^2}]\Big] - \tag{5.22}$$
$$\frac{1}{2}R_i^{1-n}(R_o^2 - R_i^2){}_2F_1[\frac{1-n}{2}, -n, 1+\frac{1-n}{2}, \frac{R_i^2}{R_o^2}]\Big) + 2\pi m_c L_c R_o^2\left[\frac{3n+1}{n}\frac{U_o R_o^2}{R_i^{\frac{3n+1}{n}}}\right]^n$$

$$F_\tau = 2\pi\frac{m_f}{2-n}\Big(U_o R_o^2\delta^{-2}\frac{2n+1}{n}\Big)^n\Big[R_o^{2-n}\frac{\Gamma(\frac{4-n}{2})\Gamma(1+n)}{\Gamma(\frac{4+n}{2})} - R_i^{2-n}{}_2F_1[\frac{2-n}{2}, -n, \frac{4-n}{2}, \frac{R_i^2}{R_o^2}]\Big] \tag{5.23}$$

5.3.1 Determination of Melt Thickness

The force equation derived in the previous section contains two unknown variables. These are the velocity of the melt at the solid-liquid interface (U_o) and the melt thickness (δ). However, by applying conservation of mass in the solid-melt interface, the velocity U_o can be expressed in terms of the filament velocity (U_{sz}) as shown in Equation 5.24.

$$U_o = U_{sz}\frac{\rho_s}{\rho_m} \tag{5.24}$$

ρ_s is the density of the solid filament, and ρ_m is the density of the molten material. To find an expression for δ, an energy balance can be performed across the melt film as shown in Figure 5.5 and given by Equation 5.25. This expression is known as the Stefan condition [57]. The Stefan condition assumes that the heat transfer mechanism occurs through conduction of the material from the heated wall towards the solid-melt interface as schematically depicted in Figure 5.2a.

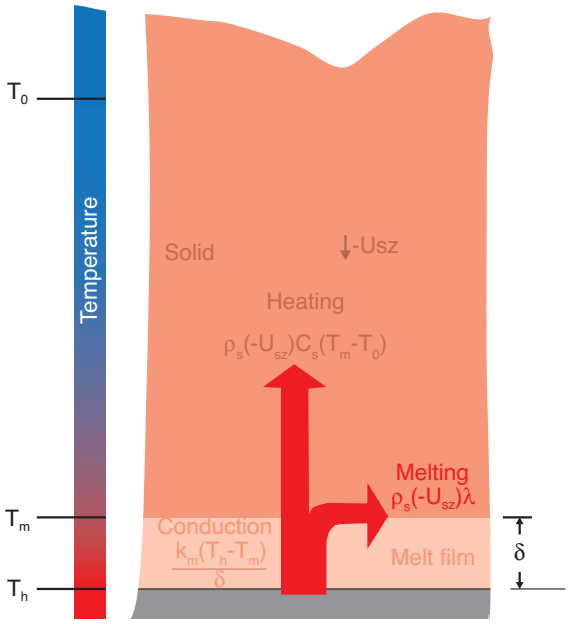

Figure 5.5: Energy Balance within the solid filament and melt film interface.

$$\frac{k_m(T_h - T_m)}{\delta} = \rho_s(U_{sz})[\lambda + C_s(T_m - T_o)] \tag{5.25}$$

where k_m is the thermal conductivity of the melted material, T_m is the melting temperature, T_o is the initial temperature of the filament, T_h is the heater temperature, C_s is the specific heat of the solid filament, and λ is the heat of fusion. Solving for the melt thickness an expression as a function of the filament velocity is obtained as shown in Equation 5.26.

$$\delta = \frac{k_m(T_h - T_m)}{\rho_s(U_{sz})[\lambda + C_s(T_m - T_o)]} \tag{5.26}$$

Substituting Equation 5.26 into Equation 6.17 the filament force can be calculated as a function of the filament velocity. Here, the remaining values are either geometrical or material properties known and shown in the next sections.

5.3.2 Initial Temperature of Filament

The initial temperature of the filament is different than the ambient temperature due to the filament moving downward. This temperature difference results from the heat transfer of the heated nozzle walls to the moving filament material. In this section, the objective is to create a simple analytical solution to calculate the initial temperature of the filament as a result of the heat emitted from the heated nozzle. Radiation is assumed to be the medium of heat transfer because the filament diameter is smaller than the nozzle diameter. Furthermore, it

is assumed that the filament and nozzle contact during the downward movement does not occur. This creates an air gap between the two surfaces, which allows heat to radiate. This mechanism is responsible for raising the temperature of the filament as it moves downwards the printing nozzle.

The melting model proposed by Osswald et al. [1] assumes the filament temperature is constant, equal to the ambient temperature, along the nozzle length. This means that the effect of radiative heating on the filament temperature is not taken into account. In this work, a radiation heat transfer analysis is performed assuming that at any time t the temperature of the film is uniform and the material properties are constant. The filament velocity (U_{sz}) is used to calculate the initial temperature due to radiation, T_{if}, located right before the filament makes contact with the end of the nozzle. An energy balance is performed in a control volume of length L as illustrated in Figure 5.6 and shown in Equation 5.27.

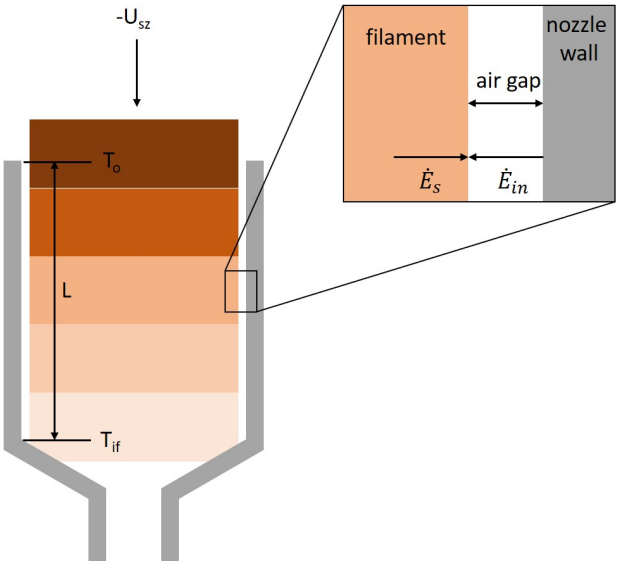

Figure 5.6: Energy balance within the solid filament and melt film interface.

$$\dot{E}_s + \dot{E_{in}} = 0 \tag{5.27}$$

where $\dot{E}_s$ and $\dot{E_{in}}$ are the energy transfer due to radiation and through the solid filament as shown in Equation 5.28 and Equation 5.29, respectively.

$$\dot{E}_s = \frac{d}{dt}(\rho V_o C_s T) \tag{5.28}$$

$$\dot{E_{in}} = \epsilon\sigma A_o(T^4 - T_h^4) \tag{5.29}$$

where ϵ is the emissivity, σ is the Stefan-Boltzmann constant, A_o is the surface area of the filament inside the nozzle, and V_o is the volume of the filament inside the nozzle. The area and volume are defined as $A_o = \pi D_o L$ and $V_o = \pi D_o^2 L/4$ where D_o is the filament diameter

and L is the length of the filament in the straight nozzle section. Substituting Equation 5.28 and Equation 5.29 into Equation 5.27 results in Equation 5.30.

$$\frac{dT}{dt} = K(T^4 - T_h^4) \tag{5.30}$$

where $K = \frac{\epsilon\sigma A_o}{\rho V_o C_s}$. Integrating using the known boundary and initial condition results in Equation 5.31.

$$\int_{T_o}^{T_{if}} \frac{dT}{(T^4 - T_h^4)} = K \int_0^{t_f} dt \tag{5.31}$$

where t_f is the time it takes the filament to travel down the nozzle, T_{if} is the filament initial temperature, and T_o is the ambient temperature. The integration of Equation 5.31 yields the implicit solution for the initial temperature of the filament. Using $t_f = L/(U_{sz})$ results in Equation 5.32.

$$ln\Big(\frac{T_h + T_{if}}{T_h - T_{if}}\Big) + 2tan^{-1}\Big(\frac{T_{if}}{T_h}\Big) = ln\Big(\frac{T_h + T_o}{T_h - T_o}\Big) + 2tan^{-1}\Big(\frac{T_o}{T_h}\Big) + 4T_h^3 K\frac{\Delta L}{(U_{sz})} \tag{5.32}$$

The filament initial temperature T_{if} can be solved in an iterative process to satisfy the equality. Using this process, the initial filament temperature can be calculated for a range of filament velocities, nozzle lengths, and nozzle temperatures. Since the analysis assumes the temperature, it is a good first approximation for calculating this temperature value.

5.4 Experimental

5.4.1 Materials

Acrylonitrile Butadiene Styrene (ABS) and Polylactic Acid (PLA) have been chosen as the materials for the experiments presented in this work. A custom ABS filament has been developed for the FFF process. The reasoning behind this decision was two-fold. First, the use of an off-the-shelf, commercial thermoplastic filament generally does not guarantee consistency between spools of material. Second, the results from Koch et al.[83] show that fluctuations in the filament diameter have an impact on the mechanical properties of FFF parts due to improper volumetric output at the nozzle. The PLA material used is commercially available.

The Cycolac®MG94 material produced by SABIC corporation[84] was chosen for this work. The MG94 was extruded in-house into a filament. The complete procedure can be found in the Appendix B.0.2. The PLA, distributed by Matterhackers (MatterHackers, Lake Forest, CA), is the Natural PLA from the PRO series. ABS is an amorphous material, whereas PLA is a semi-crystalline material. Each material requires different heater temperatures for ideal printing conditions. The supplier often provides suggested values.

5.4.2 Printer Setup and Data Acquisition

For this work, an FFF printer produced by FusedForm (Minilab by FusedForm, Colombia) was equipped with a concentric force sensor (model AUTOF-S115-15kg), an encoder (type GTS06-VE-RA600A-2M), and a thermistor. This setup allowed recording and visualization of the filament force, velocity, and nozzle temperature while extruding. The data was collected, processed, and visualized using an Arduino board connected to MATLAB.

The open-source software Pronterface [85] was utilized to control the machine. The data acquisition, similar to [26], consisted of printing at a determined velocity for two minutes. During this time, the filament force and filament velocity were acquired by the system. For analysis purposes and to achieve steady-state, the data analyzed consisted of 1 min of recording after 30 seconds of inputting the command. A moving average was performed on the data with a local 5-point mean value to cancel out noise. The data were then averaged, and a standard deviation was calculated for each condition. The controlled velocity started at 0.25 mm/s with an increment of 0.25mm/s for the first two terms and 0.5 mm/s for the rest of the terms. Once the measured velocity deviates from the input velocity, the limit velocity was considered for the respective temperature. A wide range of processing temperatures were tested, considering the temperatures suggested by the respective suppliers. For the PLA, the minimum and maximum printing temperatures are 200 ^{o}C and 235 ^{o}C, respectively. For ABS these values are 200 ^{o}C and 245 ^{o}C respectively.

5.4.3 Printing Nozzle

Micro Computed Tomography (μ-CT) of Nozzle and Post-Processing

A ZEISS METROTOM 800 (ZEISS, Germany) was used to find the dimensions of the printing nozzle. A resolution of 30 μm/pixel was used to obtain a high-resolution image. The μ-CT data comprises a 3D reconstruction of the scanned sample, which is exported to 2D image stacks [59]. Fiji [60], an open-source image processing software, was used as the tool to analyze the ZEISS METROTOM 800 output data. The image type was selected to 16-bit unsigned, the width, height, offset to the first image, the number of pictures chosen according to the output file (image dimension), and the little-endian byte order enabled.

Nozzle Geometry

An E3D V6 [86] was used as the printing nozzle for these experiments. The result of the μ-CT scan data is shown in Figure 5.7.

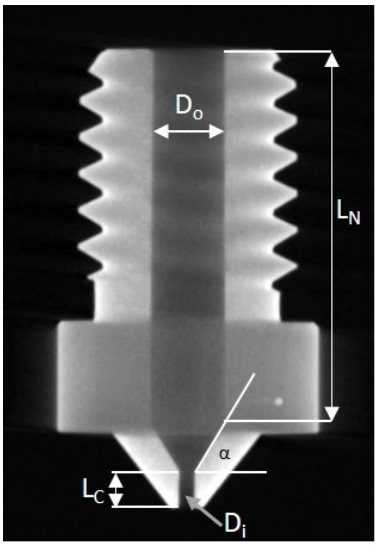

Figure 5.7: CT Scan of printing nozzle.

The nozzle possesses an angle of 56.31^o, a nozzle length (L_N) of 10.20 ± 0.03 mm, a nozzle diameter (D_o) of 1.97 ± 0.03mm, and a capillary length (L_c) and diameter (D_i) of 1 ± 0.03mm and 0.4 ± 0.03mm respectively. These values were used as input parameters for the nozzle geometry in the mathematical model validation.

5.4.4 Differential Scanning Calorimetry (DSC)

A Netzsch DSC 214 Polyma (NETZSCH GmbH & Co. Holding KG, Selb, Germany) was the instrument of choice. To perform a high-quality measurement, the methods presented in the Netzsch DSC Handbook [62] were used. Here, the sample mass, the isothermal phase, heating/cooling rates, crucible type, and test atmosphere are suggested. Since the first glass transition temperature (T_{g1}) of the materials are not relevant, the initial temperature for both materials is 20 ^{o}C. A pierced lid aluminum crucible was used for both materials. Starting at 20 ^{o}C, the temperature was raised to 200 ^{o}C and back to 20 ^{o}C at a rate of 10 K/min. Then, an isothermal phase (7 minutes for the ABS and 5 minutes for the PLA) was given, followed by second heating to 200 ^{o}C at the same rate. Two heating phases were made for each material to eliminate processing influences on the result [63]. The first heating shows the entire history of the sample while the second heating shows the material properties, and it is subsequently used for material characterization [62].

5.4.5 Rheological Properties

The rheological properties of the PLA and ABS material were measured using a AR 2000ex rheometer (TA Instruments, Inc., New Castle, DE) with 25 mm parallel plate geometry. The dynamic viscoelastic properties were determined within the frequency range of 0.1 Hz - 100 Hz (0.0628 - 628.3 rad/s) using a strain value within the viscoelastic region (strain

from 0.2% to 0.4%), which is dependent on the temperature. A frequency sweep test was performed for both materials at temperatures of 170 ^{o}C, 200 ^{o}C, 220 ^{o}C, 230 ^{o}C and 240 ^{o}C for the ABS material and 180 ^{o}C, 200 ^{o}C, 220 ^{o}C, 240 ^{o}C, and 260 ^{o}C for the PLA material. The gap used for the test was 1 mm. Applying the Cox-Merz rule [34], which states that the complex viscosity and steady shear viscosity are equivalent when the angular frequency w is equal to the steady shear rate $\dot{\gamma}$ [65] as shown in Equation 4.3.

Since the instrument used for the viscosity test has a limited shear rate range, the time-temperature-superposition (TTS) principle was performed. Two viscosity models were used to predict the viscosity as a function of shear rate. These are the Carreau-Yasuda (CY) model and the power-law model. These are shown in Equation 4.4 and 5.33 respectively.

$$\eta = m\dot{\gamma}^{n-1} \tag{5.33}$$

where η_o is the zero-shear viscosity, λ is the consistency, b is the rate index, and a is the transition index. m is the consistency index for the power-law model, and n is the power-law index. The CY viscosity model was used to describe the viscosity of the materials fully. Since Osswald et al. [1] derived the model assuming a Newtonian viscosity and correcting it using the power-law model, it is assumed that any viscosity model (that fit the data) can be used to describe the viscosity. The fitting parameters for the CY model and the power-law model were found using the Matlab fitting tool.

5.5 Discussion

5.5.1 DSC Measurements and Determination of Melting Temperature

Experimental data for PLA and ABS materials can be observed in Section B.0.4. As expected from the ABS material, the glass transition temperature can be observed by a step in the baseline of the DSC curve. This transition can be seen for both amorphous and semi-crystalline materials. Here, the mid-T_g is used with a value of 104.5 ^oC. For the PLA material, a step in the baseline data is also found. Similar to what was done for ABS, a mid-T_g with a value of 58.9 ^oC is used. The melting temperature (T_m) corresponds to a peak in the DSC data. In this case, the peak is reached at a temperature of 150.9 ^oC. Due to the amorphous structure of ABS, when T_g is reached, the material can flow.

5.5.2 Linear Viscoelastic Region and Viscosity Model

The polymer materials used in the experiments are shear thinning. A dynamic viscosity test was performed to investigate the linear region for all samples and temperatures as shown in the appendix (Section B.0.5). A master curve was created using the viscosity data shown in Figure B.3 together with the Trios software from TA Instruments (TA Instruments, DE, USA). Here, the Time-Temperature Superposition (TTS) was used to find the shift factor in the x-direction. A reference temperature of 200 ^{o}C was selected for both materials. The

Arrhenius model (Equation 3.2) was used for the PLA, while the Williams-Landel-Ferry (WLF) model (Equation 3.3) was used for the ABS material.

where E_a is the activation energy with a value of 80574.4 J/mol, R is the universal gas constant, and C_1 and C_2 are 3.93791 and 128.563 K respectively. Figure 5.8 shows the horizontal shift factor for all the temperatures. The shift factor can also be expressed as shown in Equation 3.4.

Where $\eta_o(T_{ref})$ is the viscosity at the reference temperature and $\eta_o(T)$ is the temperature at the corresponding processing temperature.

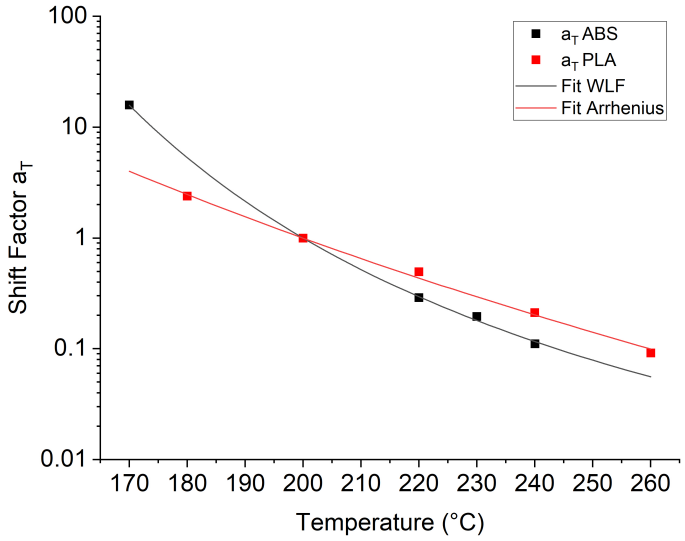

Figure 5.8: Horizontal shift factor for ABS and PLA.

Figure 5.9 shows the master curve of the complex shear viscosity together with the Power Law model and the Carreau-Yasuda model. The fitting parameters for the Carreau-Yasuda model and the Power Law model were calculated using the Matlab curve fitting tool. The parameters for both models are shown in Table 5.1.

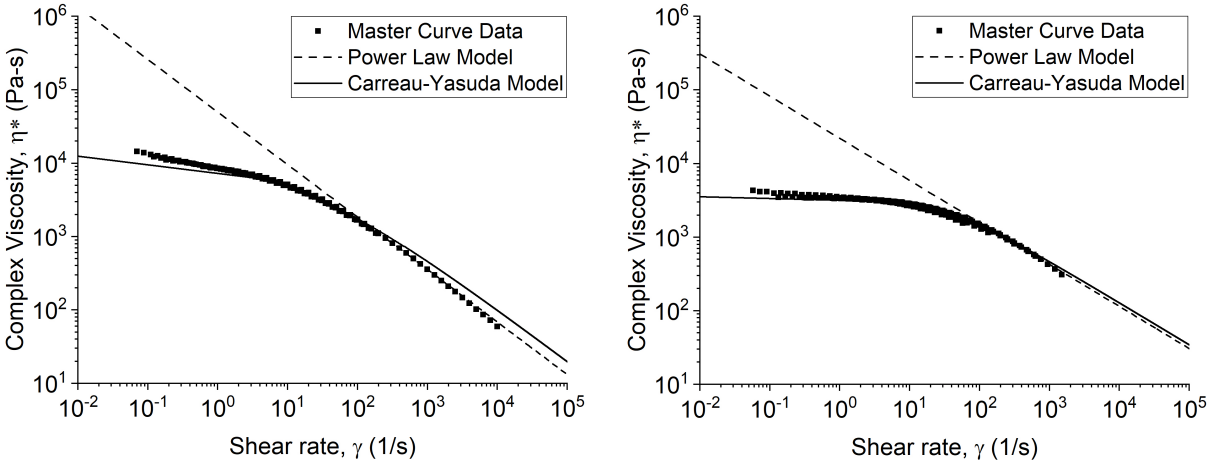

Figure 5.9: Shear rate dependence on complex viscosity as a function of temperature for (a) ABS and (b) PLA.

Table 5.1: Power law and Carreau-Yasuda fitting parameters.

Material	Carreau-Yasuda Model					Power Law Model		
	η_o (Pa-s)	λ (s)	a (-)	b (-)	R^2	m (Pa-s)	n (-)	R^2
ABS	1.325e4	8.675e-2	0.4695	0.2847	0.9978	4.977e4	0.2847	0.9994
PLA	3.546e3	3.333e-2	0.8295	0.4287	0.9914	2.206e4	0.4287	0.995

The Carreau-Yasuda does not fit the ABS properly, but for comparison purposes, this was performed. With this data, it is possible to calculate the viscosity of these materials at higher shear rates and in a range of nozzle heater temperature by using the shift factor described above. In addition, for simplification purposes, a variable is defined which assumes the temperature of the melt film (T_f). This temperature is used to calculate the rheological properties of the melt film.

5.5.3 Determining Filament Initial Temperature

The radiative heat transfer from the nozzle to the filament must be considered to allow a more accurate analytical model for the melting rate determination. The material properties used for both ABS and PLA are shown in Table B.1. A nozzle length of 10.2 mm and an ambient temperature of 25 ^oC were used for the calculations. An emissivity (ϵ) of 0.9 was chosen for both materials [87]. Results of the initial filament temperature (T_{if}) as a function of the filament velocity are shown in Figure 5.10.

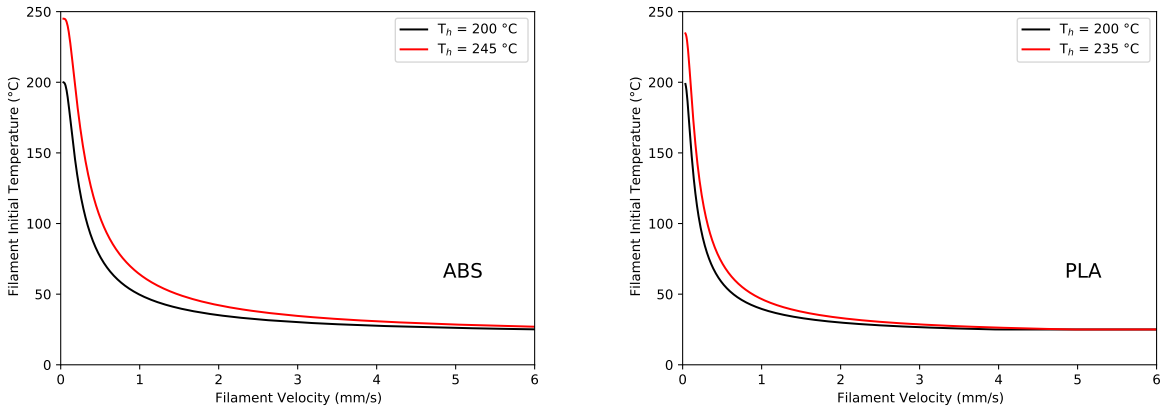

(a) (b)

Figure 5.10: Filament initial temperature as a function of the filament velocity for a range of heater temperatures for (a) ABS and (b) PLA.

As seen for both materials, the lower the filament velocity the closer the initial filament temperature is to the heater temperature ($T_{if} = T_h \rightarrow U_{sz} = 0$). As the filament velocity increases, there is less time to heat up from its ambient temperature. For simplification purposes, an initial filament temperature of 70 ^{o}C and 50 ^{o}C will be used for ABS and PLA, respectively. These values are equivalent to the initial filament temperature at a velocity of 1 mm/s.

The results are shown here corroborate the assumption made by Bellini et al. [18], and Osswald et al. [1]. Bellini et al. assume low filament velocities allow the material to reach the melting temperature and create a material pool inside the nozzle. However, increasing the filament velocity prevents the filament from melting. Since the filament is still in a solid state, a melt film will be created once it makes contact with the heated nozzle, which is the assumption made by Osswald et al. These results demonstrate that it is necessary to have a model that takes into account the presence of both phases (solid and melt state) to make an accurate prediction of the melting rate inside an FFF nozzle. A model like this has been reported recently by Luo et al. [22]. A difference between the model reported by Luo et al. [22] and the experimental data of ABS material was found for values of filament velocity above 1.5 mm/s. Even though the prediction is possible under this velocity, it is necessary to predict the filament velocity at higher rates if high flow rates are desired. In this work, the assumption of the creation of a melt film is used.

5.5.4 Experimental Data

FFF Printer

Following the procedure described above, the measured filament velocity as a function of the input velocity was plotted for both materials as shown in Figure 5.11. Once the measured

speed deviates from the specified rate, it is assumed that slippage in the gears occurs. It can also be observed that the allowable maximum printing velocity, one that does not deviate from the specified speed, increases with increasing printing temperature. This is attributed in part to the amount of melted material inside the nozzle. Higher temperatures guarantee that material will be in a molten state and lead to lower viscosity.

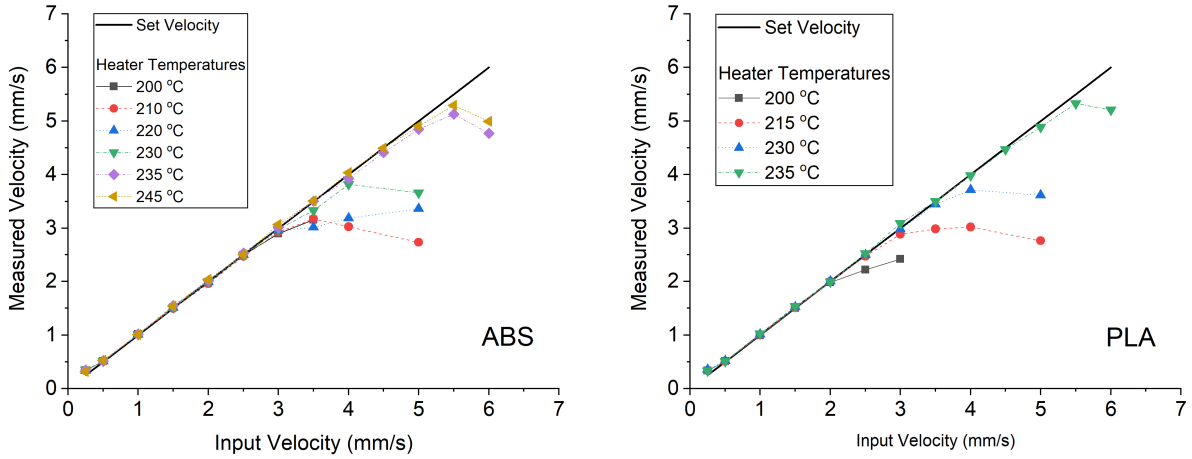

(a) (b)

Figure 5.11: Comparison of measured filament velocity and input filament velocity at various heater temperatures for (a) ABS and (b) PLA.

The measured velocity over the input velocity ($U_{measured}/U_{input}$) as a function of the filament force is shown in Figure 5.12. The line on both graphs indicates the set value of the velocity ratio. Once the ratio deviates from this line, it is expected that slippage in the driving gears occurs. The deviation is observed at low forces due to the sensitivity of the force sensor. At higher pressures, deviation from the theoretical value is also observed. This is also noted by a transition force that predicts the filament from sticking to slippage in the feeder gears. The trend of a transition force can be seen for the PLA material except for the 235 ^{o}C.

Contrary to PLA, ABS shows no clear trend. This is attributed partly to the ABS structure and the unclear threshold between solid and melt material. Since ABS is a co-polymer, complex mixing and de-mixing of the raw material can lead to significant deviations in the microstructure and melting temperature. This in term leads to changes in melting behavior. Others have also observed this behavior [23, 26], some suggesting grinding of the filament. The magnitude in force and velocity coincide with experimental data from literature [25, 26].

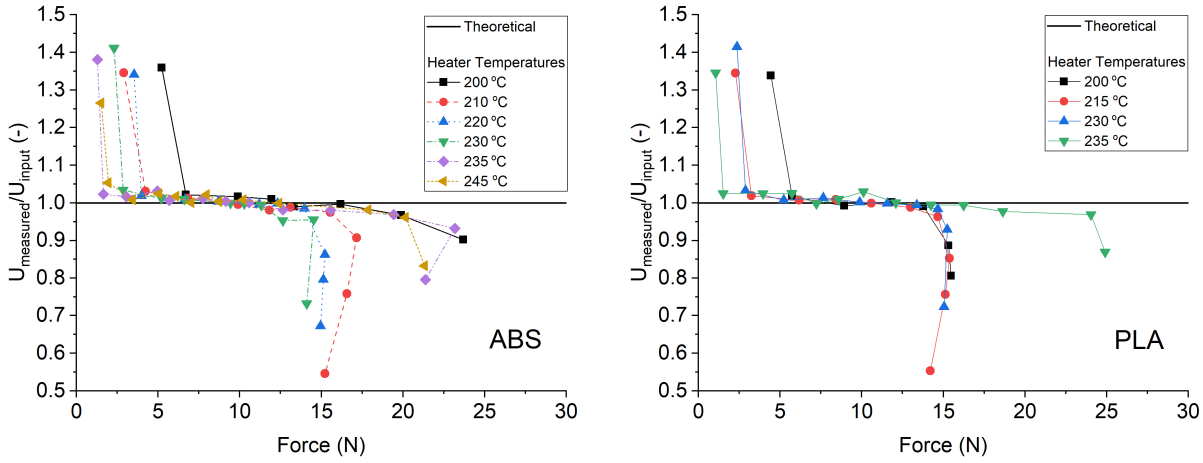

(a) (b)

Figure 5.12: Measured velocity over input velocity ($U_{measured}/U_{input}$) as a function of filament force for (a) ABS and (b) PLA.

FFF Model Comparison

For ease of visualization, only two temperatures are plotted for each material. The material properties and the values used for the theoretical model were taken from literature and can be found in Appendix B.0.3. Here, two theoretical models are also included and compared. These are Bellini et al. [18], and Phan et al. [49]. First, the model derived in this work was compared with the model proposed by Osswald et al. [1]. Here, the viscosity was modeled using the Carreau-Yasuda (CY) viscosity model to predict the viscosity over a wide range of shear rates. Compared to the power-law model used by the authors, the CY does not over-predict the viscosity at low shear rates. Three assumptions were made in Figure 5.13 and Figure 5.14. First, the melting temperature was assumed to be the glass transition temperature. Second, the melt film temperature was assumed to be homogeneous using the heater temperature. Third, the initial temperature of the filament used is 70 ^{o}C and 50 ^{o}C for ABS and PLA, respectively. This takes into account the influences of heated components above the heating nozzle. Others have researched this topic [52, 88].

By applying these assumptions, the models (pressure component only and pressure/shear components) are in good agreement at the lower printing temperature for both materials and the higher printing temperature of the PLA material as shown in Figure 5.13 and Figure 5.14. However, at the higher temperature of the ABS, the models deviate from the experimental data. It is essential to mention that the model presented here agrees with the PLA data under the conditions used. Since the energy balance is done under the assumption of a melt film and a defined melting temperature, the model was expected to work for semicrystalline materials.

It is interesting to see that both the model proposed by Bellini et al. and Phan et al. overestimate the filament force at low temperatures. At higher printing temperatures, the models from Phan et al. [49] tend to trend the experimental data having similar behavior.

However, there is a shift in filament force. This is expected since, in their assumptions, they model the material as a melted fluid. The results here suggest that both sets of models occur during the FFF process. At low processing temperatures, there is a melt film formation where our proposed model works. As the temperature increases, there is a shift in force, meaning over-prediction. At higher temperatures, the creation of a pool of material is more likely. Here, the models from Bellini et al. and Phan et al. approach the experimental data behavior. At this point, it is difficult to specify the temperature range where these models deviate. However, this is an open problem where more research is needed.

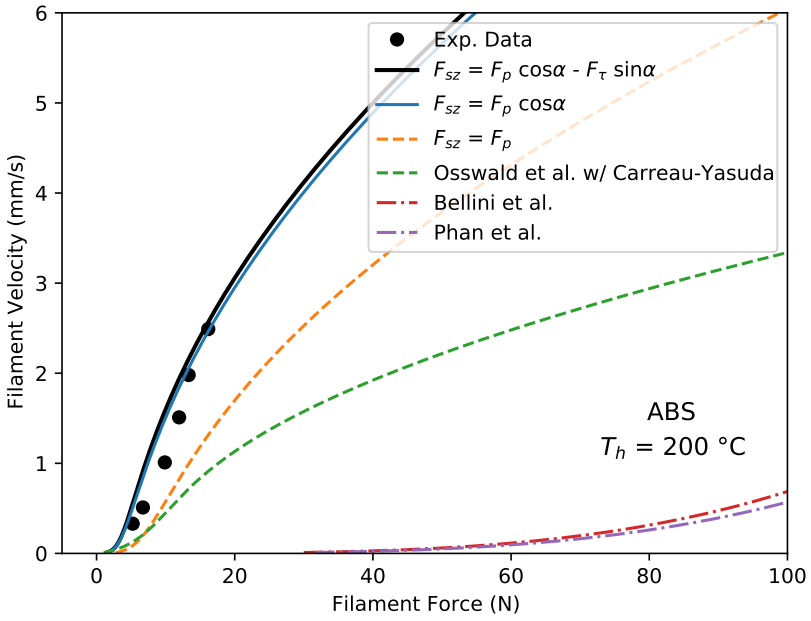

(a)

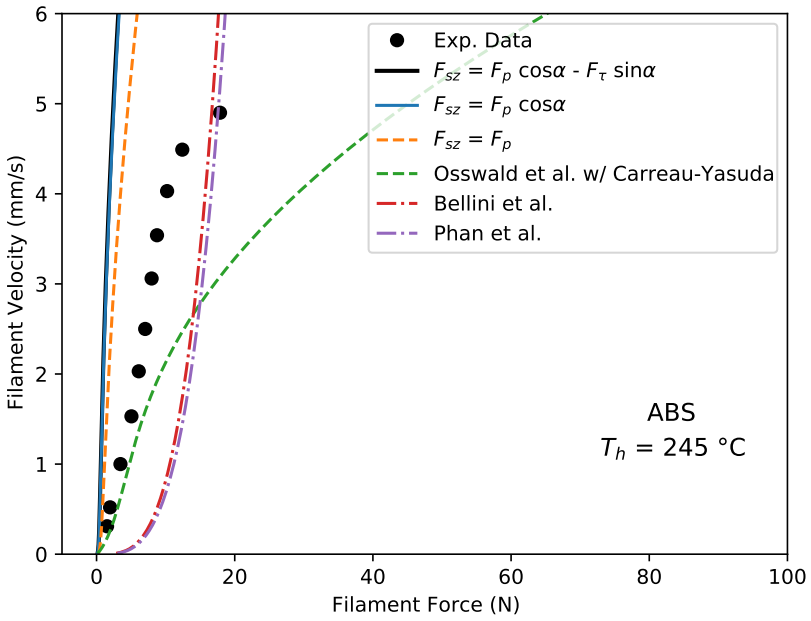

(b)

Figure 5.13: Comparison of experimental data with analytical models of ABS at (a) 200 ^oC and (b) 245 ^oC using $T_f = T_h$, $T_m = T_g$, and $T_o = 70$ ^oC.

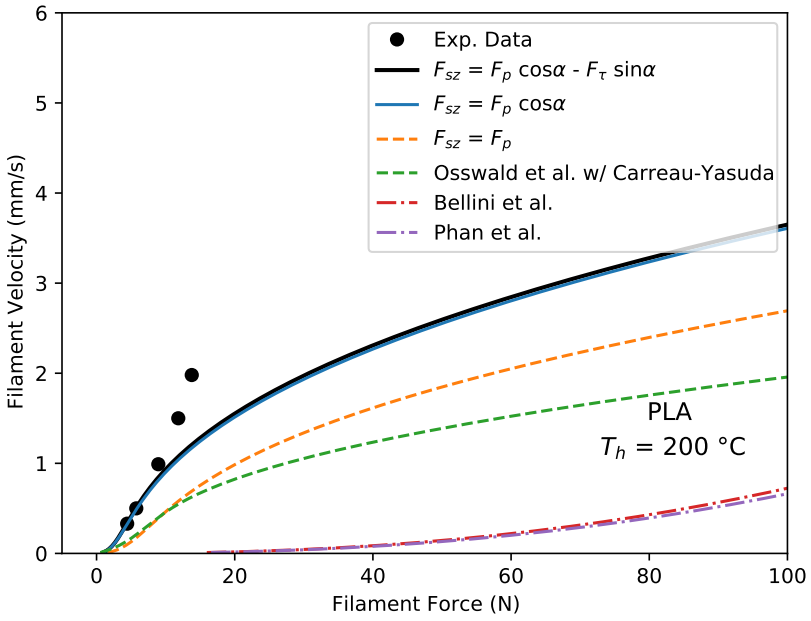

(a)

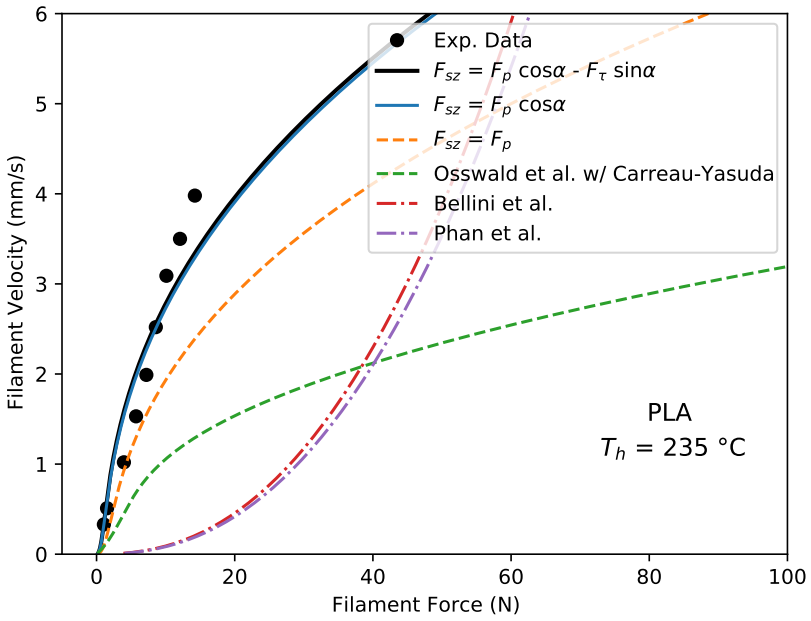

(b)

Figure 5.14: Comparison of experimental data with analytical models of PLA at (a) 200 ^oC and (b) 235^oC using $T_f = T_h$, $T_m = T_g$, and $T_o = 50^oC$.

Because the assumption used in the model is that the material can flow once it reaches the glass transition temperature, the effect of T_m is studied for ABS since for semi-crystalline materials, the flow transition temperature is well defined. Figure 5.15 show the influence of T_m over a temperature range. The film temperature and the initial temperature are kept the same for ease of comparison. It can be seen that the increase in T_m increases filament force. The model can capture a change in slope similar to the experimental data attributed to the material's shear thinning. The force does not have a constant relationship with the velocity. Since viscosity is related to the shear rate, as the filament velocity increases, the force necessary to extrude the material decreases, it is important to point out that our model fails to predict the filament velocity at higher temperatures (Figure 5.15b). This could be attributed partly to the material being in a melt state before reaching the bottom of the nozzle.

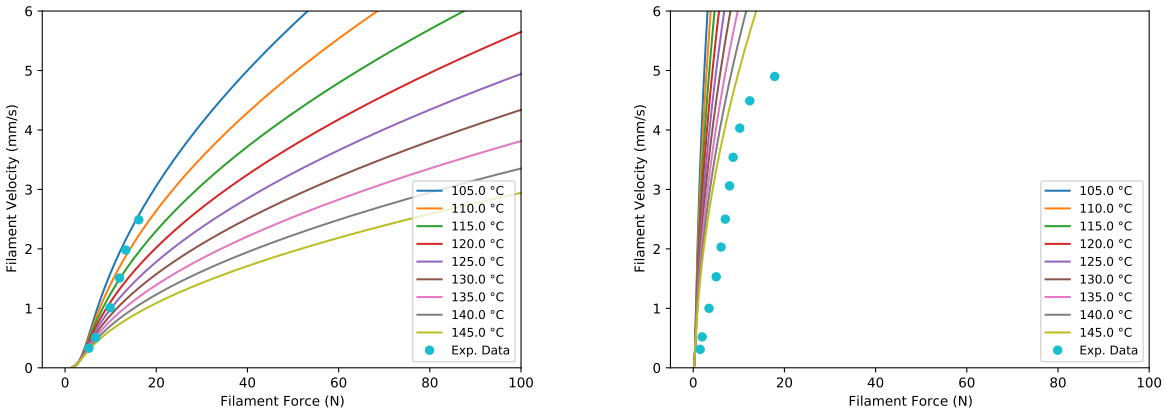

Figure 5.15: Effect of T_m for ABS at (a) 200 ^oC and (b) 245 ^oC using $T_f = T_h$ and $T_o = 70^oC$.

As the deviatoric stress and pressure component are included in the force calculation, it is essential to know the magnitude of both terms in the force. The model presented here is plotted over a range of nozzle angles as shown in Figure B.6 and Figure B.7 from Appendix B.0.8. The film temperature, initial temperature, and melting temperature are kept the same. The influence of nozzle angle is studied at a filament velocity of 2 mm/s because at this velocity; there is no observed slippage in the acquired experimental data (Figure 5.12). From the plots, it can be seen that at a nozzle angle of 0^o, there is not an influence of the deviatoric stress. As the angle increases, the impact of deviatoric stress increases while the pressure decreases. Even though there is an influence of angle, the magnitude of the force due to the deviatoric stress is much less than the force due to pressure ($F_\tau \ll F_p$).

This work assumes that the material will flow once it reaches the glass transition temperature. In literature, it is suggested to use a softening temperature instead of T_g, which is estimated to be 40 - 50 ^oC above T_g. For the case of the effective temperature of the viscosity in the melt film, it is known that a temperature gradient is present between the nozzle wall

and the solid-melt interface. This means that a viscosity gradient will be present in the melt film. Since our model is isothermal, the temperature to use is unknown. A straightforward method would be to take the average temperature between the heater temperature at the wall and the material's melting temperature. Still, at this point, there is no way to predict this temperature physically. Instead, an effective temperature was introduced to make the model adaptable to the data if desired. The effective temperature is used as the film temperature ($T_{eff} = T_f$), which is needed to calculate the rheological properties of the melt film. For this study we used $T_f = T_h$. Ideally, the effective temperature should include the effects of heat transfer mechanisms present in the process. As shown in Figure B.4 and Figure B.5, using the mentioned assumptions, the models proposed in this work over-estimate the filament force. The effect of these temperatures can be seen in the value of the melt thickness. The latest conditions decrease the melt thickness value while the initial conditions (shown in Figure 5.13 and 5.14) increase the melt thickness value. When substituting these into Equation 6.17, one increases the filament force while the other decreases it.

The model's accuracy relies on knowing the material's mechanical properties and the measured parameters such as temperature and filament velocity. As demonstrated, slippage could occur during the process, producing inconsistency and differences in the measured data. At the same time, understanding the heating mechanisms is vital to calculate an adequate temperature for the melt film. This model can monitor the FFF printing process by predicting and optimizing maximum allowable velocity while minimizing failure scenarios. Optimizing the speed will ensure a decrease in process time.

Implementation of the model requires knowledge of a coding language. For this work, Python [89] was the language used to perform the calculations. It only requires the availability of a computer since it is open-source. Since it is an analytical model, the computational time is minimal.

5.6 Conclusion

The model presented in this paper builds upon previous work from Osswald et al. [1] by incorporating the shear thinning behavior in the derivation of the model. From these improvements, key points can be concluded:

- An analytical model was successfully derived by using the inclusion of the power-law fluid.

- The model presented here was able to model the experimental data of a semi-crystalline material at different processing conditions using the heating temperature as the film effective temperature.

- The radiative heat transfer approach allowed estimating the initial filament temperature over a range of filament velocities.

- It is suggested that two models are necessary to predict the melting behavior in an FFF printer both at low and high-temperature range using a consistent, effective temperature $T_{eff} = T_f$.
- Our experimental data corroborates the findings from other authors. The force and velocity are comparable in magnitude using similar printing nozzles. Also, a transition force during the FFF process was found.
- The magnitude of the deviatoric stress component under our current assumptions was found to be much less than that of the pressure component.
- It is suggested that it is necessary to increase the nozzle temperature to print at higher filament velocities. However, other effects such as degradation have to be considered.

5.7 Acknowledgement

The unique collaboration was performed with Nancy Granda and Stefan Heimer. They performed review and correctness of mathematical model and derivation.

6. Effect of Radiation Heat Transfer and Nozzle Diameter on the Fused Filament Fabrication Melting Model

The effect of radiation heat transfer and nozzle diameter was studied for the FFF process. Filament velocity and filament force were acquired using a customized FFF printer with a concentric force sensor and an encoder. Data was collected for ABS and PLA materials, three nozzle capillary diameters, and four heater temperatures. Afterward, the data was compared with five analytical melting models. The radiation effect on the filament's initial temperature and melt film thickness was studied. As expected, it was found that the initial filament temperature decreased as the filament velocity increased. This is attributed to the radiation heat transfer occurring at low filament velocities, which increases the filament temperature. As the filament temperature was increased, the melt film thickness also increased. By incorporating the radiation effect, it was possible to observe the non-linear behavior of the melt film thickness over a range of filament velocities. Plotting the ratio of measured and input speed, it was found that there exists a critical force where slippage occurs. It was found that this critical force will be the same no matter the nozzle geometry and processing temperature and will be dependent on material mechanical properties. An analytical approach was suggested, which coincides with the critical force value found experimentally. When comparing the different melting models, it was found that the model by Colon et al. [90] describes best the process for ABS material. For the PLA material, it was found that the models by Bellini et al. [18] and Luo et al. [22] best describe the process up to a filament force of 15 N for some conditions. The results give insight into what models best describe the FFF process for each material, nozzle capillary diameter, and process temperature.

6.1 Introduction

The fused filament fabrication (FFF) process is an additive manufacturing process that has been on the forefront due to the low cost of machines and materials, availability of machines and parts in the market, and the ability to manufacture with ease complex geometries. During the manufacture of a part, the material is melted and extruded using a heated nozzle and fed using gears. The extruded material is then placed bead-by-bead, and layer-by-layer

through a diffusion dominant welding process [2, 83] until the part is finished. As a result of the layer-by-layer process, the printing speed will be a function of many parameters [3]. Some of them have been infill percentage, layer thickness, printing speed, and print temperature, to mention a few [91, 92].

As a result of the long printing times, understanding the melting behavior of the FFF process has been of interest in the past years [18–22, 26, 49, 90]. The models have different approaches to understand the melting kinetic and behavior during printing. The model presented by Bellini et al. [18] and Phan et al. [49] assumes that melting of the filament material takes place while it is fed towards the printing nozzle. The melting process occurs due to the heat transfer from the filament channel walls to the filament material. Other authors like Heller et al. [21], model the FFF process by including the viscoelastic effects of the materials. Numerical approaches have also been implemented to understand the melting behavior during the FFF process [26]. Luo et al. [22] take a heat transfer approach by solving a Graetz-Nusselt problem focusing on the boundary between the solid and molten polymer in the heated portion of the tube. A new method was presented by Osswald et al. [1] which incorporates the formation of a melt film that varies as a function of the filament force and filament velocity.

Moreover, Colon et al. [90] improved the model presented by Osswald et al. by including the effects of shear-thinning behavior within the momentum equations and proposed an equation to calculate the filament temperature as a result of the radiation effects. The heat transfer, in this case, occurs while the filament moves toward the printing nozzle from the heated walls to the filament material. A similar approach has been made by other [22] to incorporate the heat transfer effects in the melting model. Colon et al. in their work presented the radiation approach but did not implement the radiation model on the melting model. Instead, a constant filament temperature was used for all the filament velocities for validation of the model.

The work presented here is based on the approach suggested by Colon et al. [90]. The radiation effects will be implemented to calculate the initial filament temperature as a function of the filament velocity. Moreover, the impact of nozzle diameter will be studied for model validation. An FFF printer produced by FusedForm Corp. (Bogotá, Colombia) was modified to incorporate a concentric force sensor, an encoder, and a thermistor to capture real-time data. The equipment will allow for the acquisition of filament velocity and filament force while controlling the nozzle temperature. Results will be compared with models found in the literature using different printing temperatures, materials, and nozzle diameters.

6.2 Experimental

6.2.1 Materials

Acrylonitrile Butadiene Styrene (ABS) and Polylactic Acid (PLA) were used for the experiments. The reason behind this decision is that these are the most commonly used 3D printing plastics [93]. A custom ABS filament has been developed for the FFF process.

The Cycolac®MG94 material produced by SABIC corporation[84] was chosen for this work. The MG94 was extruded in-house into a filament. The complete procedure can be found in [90, 94] where the methods ensured that the filament geometry caused minimal variation of results. The PLA, distributed by Matterhackers (MatterHackers, Lake Forest, CA), is the Natural PLA from the PRO series. ABS is an amorphous material, whereas PLA is a semi-crystalline material. Each material requires different heater temperatures for ideal printing conditions. The supplier often provides suggested values. Both filaments possess a nominal diameter of 1.75 mm.

6.2.2 Nozzle Geometry

Three nozzle geometries were used to study the effect of the nozzle diameter on the melting models. The nozzles selected for the study were V6 nozzles with nominal nozzle diameters of 0.25 mm, 0.4 mm, and 0.6 mm. A ZEISS METROTOM 800 (ZEISS, Germany) was used to find the dimensions of the printing nozzle. Fiji [60], an open-source image processing software, was used as the tool to analyze the ZEISS METROTOM 800 output data. A schematic of the nozzle can be seen in Figure 6.1.

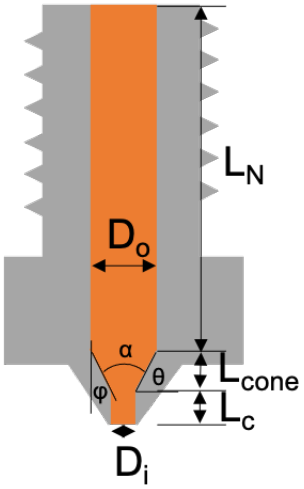

Figure 6.1: Schematic of V6 nozzle dimensions.

The nozzle dimension for all the nozzle diameters is shown in Table 6.1. These values are required for the prediction of the melting behavior for all the models.

Table 6.1: Dimensions of printing nozzle.

Nozzle	D_o (mm)	D_i (mm)	L_N (mm)	L_{cone} (mm)	L_c (mm)	θ
0.25 mm	2.03	0.26	11.02	0.97	0.62	52.14^o
0.40 mm	2.01	0.42	10.2	1.59	0.75	54.76^o
0.60 mm	2.04	0.59	10.34	1.16	0.91	56.04^o

The nozzle angle for the Bellini et. al [18], Phan et. al [49], and Luo et. al [22] can be calculated using $\alpha = 2(90 - \theta)$ and $\phi = (90 - \theta)$.

6.2.3 Print Setup and Procedure

A commercial FFF printer, produced by FusedForm (Minilab by FusedForm, Colombia), was used for the experiments. The printer was equipped with a concentric force sensor (model AUTOF-S115-15kg), an encoder (type GTS06-VE-RA600A-2M), and a thermistor, as shown in Figure 6.2. The setup allowed recording and visualization of the filament force, filament velocity, and nozzle temperature while extruding the filament material. The data was collected, processed, and visualized using an Arduino board connected to MATLAB.

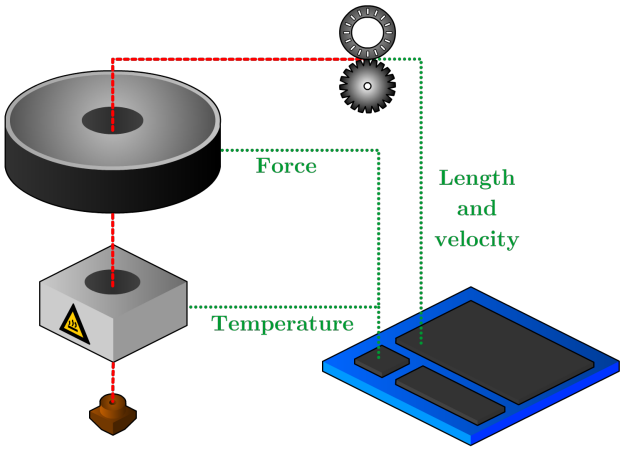

Figure 6.2: Printer setup with force sensor, encoder, and thermistor.

The open-source software Pronterface [85] was utilized to control the machine. The data acquisition, similar to [26, 90], consisted of printing at a determined velocity for two minutes. During this time, the filament force and filament velocity were recorded by the system. A moving average was performed on the data with a local 5-point mean value to cancel out noise. The data were then averaged, and a standard deviation was calculated for each condition. The controlled velocity started at 0.25 mm/s with an increment of 0.25mm/s for the

first two terms and 0.5 mm/s for the rest of the terms. Once the measured velocity deviates from the input velocity, it was considered the limit velocity for the respective temperature. A wide range of processing temperatures were tested, considering the temperatures suggested by the respective suppliers. The temperatures used for both materials were 200 ^{o}C, 210 ^{o}C, 220 ^{o}C, and 230 ^{o}C.

6.2.4 Melting Models

To study the effects of nozzle diameter, five commonly used models were used and compared the experimental data. These are the model developed by Bellini et al. [18], Phan et al. [49], Luo et al. [22], Osswald et al. [1], and Colon et al. [90]. The models are described in detail below.

Bellini et. al Model

The FFF model proposed by Bellini et al. [18] assumes that the material inside the nozzle is in a melt state. In the analytical model, the feeding force F relates the pressure drop ΔP through the hot-end as shown in equation 6.1.

$$F = \Delta P A_F \tag{6.1}$$

Where A_F is the cross-sectional areal of the filament material, the pressure drop through the hot end is approximated by the sum of the pressure drops through the different sections of the nozzle. For the Bellini et al. model, the total pressure drop is described by equation 6.2.

$$\Delta P = \Delta P_{barrel} + \Delta P_{cone} + \Delta P_{capillary} \tag{6.2}$$

where ΔP_{barrel}, ΔP_{cone}, and $\Delta P_{capillary}$ are the pressure drop in the barrel, contraction, and capillary region respectively and are shown in Equation 6.3 - 6.5.

$$\Delta P_{barrel} = K(T)\Big[\frac{1+3n}{4n}\frac{32Q}{\pi D_B^3}\Big]^n \frac{4L_B}{D_B} \tag{6.3}$$

$$\Delta P_{contraction} = K(T)\Big[\frac{1+3n}{4n}\frac{32Q}{\pi}\Big]^n \Big(\frac{1}{D_C^{3n}} - \frac{1}{D_B^{3n}}\Big)\frac{2}{3n * tan(\frac{\alpha}{2})} \tag{6.4}$$

$$\Delta P_{capillary} = K(T)\Big[\frac{1+3n}{4n}\frac{32Q}{\pi D_C^3}\Big]^n \frac{4L_C}{D_C} \tag{6.5}$$

where $Q = VA_F$. Here, V is the filament velocity, L_B is the barrel length, D_B is the barrel diameter, L_C is the capillary length, D_C is the capillary diameter, $K(T)$ is the consistency index as a function of the temperature, n is the power-law index of the material, and α is the angle of the nozzle.

Phan et al. Model

Phan et al. [49] use a similar approach as Bellini et al. [18]. However, Phan et al. model the pressure drop in the conical region by modifying the Cogswell model [50]. The model uses both shear viscosity (η) and elongational viscosity (η_e). Power-law relations govern both viscosities under the generalized Newtonian fluid (GNF) framework. Here, m and L are the consistency index for the shear and elongational viscosity. For the Phan et al. model, the total pressure drop is described by equation 6.6.

$$\Delta P = \Delta P_\alpha + \Delta P_o + \Delta P_{capillary} \tag{6.6}$$

Where ΔP_α, ΔP_o, and $\Delta P_{capillary}$ are the pressure drop in the truncated cone region, reorganization of the melt from the converging area into the capillary, and capillary respectively and are shown in Equation 6.7 - 6.8. The $\Delta P_{capillary}$ has the same expression as in the Bellini et al. model.

$$\Delta P_\alpha = K(T)\Big[\frac{1+3n}{4n}\frac{32Q}{\pi D_C^3}\Big]^n \frac{2}{3n * tan(\frac{\alpha}{2})} + L\frac{2^{1-m}}{3m} tan\Big(\frac{\alpha}{2}\Big)^m \Big(\frac{32Q}{\pi D_C^3}\Big)^m \tag{6.7}$$

$$\Delta P_o = K(T)\Big[\frac{1+3n}{4n}\frac{32Q}{\pi D_C^3}\Big]^n \frac{1.18}{n^{0.7}} \tag{6.8}$$

Both Bellini et al. and Phan et al. models assume a fully developed laminar flow inside the hot end channel with a uniform Temperature T equal to the heater temperature. Equation 6.7 includes both the shear and extensional consistency indexes. Here, it is assumed that both power-law indexes are equal, and the Trouton ratio (ratio of extensional viscosity to shear viscosity) is $Tr = L/K = 5$, similar as Phan et al. [49]. Phan et al. also neglect the wall shear stress contribution in the barrel section due to its supposedly low shear rates.

Luo et al. Model

The model proposed by Luo et al. [22] is an upper-bound estimate and takes a heat transfer approach by solving a Graetz-Nusselt problem. Their work focuses on the boundary between the solid and molten polymer in the heated portion of the tube. Here, the solution is an upper bound estimate and also a semi-empirical model as the threshold temperature is measured. For Luo et al. model, the total force is described by equation 6.9.

$$F = (\pi R_B^2)(\Delta P_1 + \Delta P_2 + \Delta P_3 + \Delta P_4 + \Delta P_5) \tag{6.9}$$

where ΔP_1 is the pressure drop of the solid portion of the filament, ΔP_2 is the pressure drop of the melt inside the cylindrical tube, ΔP_3 is the pressure drop of the melt inside the conical tube, and ΔP_5 is the pressure drop of the melt inside the print nozzle. ΔP_4 is used to represent the pressure drop from the conical tube to the print nozzle. The pressure drop for each section are shown in equation 6.10 - 6.13.

$$\Delta P_2 = 2\mu_c\Big[(L_B - Z_s L)\Big(\frac{(N+2)U}{R_B^N}\Big)^n\Big] \tag{6.10}$$

$$\Delta P_3 = \frac{2\mu_c}{3n * sin\phi}\Big[\frac{3(3n+1)UR_B^2 sin\phi}{4n(1-cos\phi)^2(1+2cos\phi)}\Big]^n\Big(\frac{1}{R_B^{3n}} - \frac{1}{R_C^{3n}}\Big) \tag{6.11}$$

$$\Delta P_4 = \mu_c\Big(\frac{3n+1}{n}\frac{UR_B^2}{R_C^3}\Big)^n\frac{1.18}{n^{0.7}} \tag{6.12}$$

$$\Delta P_5 = 2\mu_c L_C\Big(\frac{(N+2)U}{R_C^N}\Big)^n \tag{6.13}$$

where $N = (1 + \frac{1}{n})$, n is the power-law index, Z_s is the percentage of the solid portion in the filament, $L = L_B + L_{cone}$, μ_c is the constant viscosity, and U is the filament velocity. In this work, we assumed that the viscosity varies with temperature and will be equal to $\mu_c = K(T)$ where $K(T)$ is the consistency index as a function of temperature. According to Luo et al., for small Z_s, it implies that only a small portion of the filament is solid inside the nozzle. Subsequently, ΔP_1 and $Z_s L$ can be neglected. Regrouping the terms, the expression for the force results in equation 6.14.

$$\begin{aligned} F = \pi R_B^2\Big[2K(T)L_B\Big(\frac{N+2}{R_B^N}\Big)^n + \frac{2K(T)}{3n * sin\phi}\Big(\frac{3(3n+1)R_B^2 sin\phi}{4n(1-cos\phi)^2(1+2cos\phi)}\Big)^n * \\ \Big(\frac{1}{R_C^{3n}} - \frac{1}{R_B^{3n}}\Big) + K(T)\Big(\frac{3n+1}{n}\frac{R_B^2}{R_C^3}\Big)^n\frac{1.18}{n^{0.7}} + 2K(T)L_C\Big(\frac{N+2}{R_C^N}\Big)^n\Big]U^N \end{aligned} \tag{6.14}$$

Osswald et al. Model

The model proposed by Osswald et al. [1], also known as the fused filament fabrication melting model, assumes that a melt film is created at the contraction surface and flows parallel to the conic surface towards the capillary region. Here the authors used the pressure-induced melt removal process as the baseline for their model. The melt film thickness is assumed to be uniform and is calculated using the Stefan Condition as shown in equation 6.15.

$$\delta = \frac{k(T_h - T_m)}{\rho_s U_{sz}[\lambda + C_s(T_m - T_o)]} \tag{6.15}$$

Where T_h is the heater temperature, T_m is the melting temperature of the filament, T_o is the initial temperature of the filament, k is the thermal conductivity of the filament, ρ_s is the density of the solid filament, λ is the heat of fusion of the filament, C_s is the specific heat of the filament, and U_{sz} is the filament velocity. Thus, the model relates the feeding force and the filament velocity as shown in equation 6.16.

$$\begin{aligned} F = -\frac{6\pi\mu_f U_{sz}\frac{\rho_s}{\rho_m}R_B^4}{\delta^3 cos\theta}\Big[ln(\frac{R_C}{R_B}) + \frac{3}{4} + \frac{1}{4}(\frac{R_C}{R_B})^4 - (\frac{R_C}{R_B})^2\Big] \\ +8\pi\mu_c U_{sz}\frac{\rho_s}{\rho_m}L_C\Big[(\frac{R_B}{R_C})^4 - (\frac{R_B}{R_C})^2\Big] \end{aligned} \tag{6.16}$$

μ_f is the viscosity in the melt film area, μ_c is the viscosity in the capillary region, ρ_m is the molten filament density α is the nozzle angle. For this work, the temperature of the melt film area is assumed to be equal to the heater temperature.

Osswald-Colon Model

Lastly, the Osswald-Colon model [90] is an improvement to the Osswald et al. model. Here the authors incorporate the effect of shear-thinning behavior within the momentum equations. As performed by Osswald et al., the authors also used the Stefan condition to calculate the melt film thickness within the printing nozzle. The model relates the feeding force and the filament velocity as shown in equations 6.17 - 6.19. Here, both the effects of pressure and shear on the force are incorporated.

$$F_{sz} = \vec{F_p}\cos\alpha - \vec{F_\tau}\sin\alpha \tag{6.17}$$

$$\begin{aligned} F_p =& \frac{2\pi}{cos(\alpha)}\Big[U_o\Big(m\Big)^{\frac{1}{n}}\Big(\frac{2n+1}{4n}\Big)\Big(\frac{\delta}{2}\Big)^{-\frac{2n+1}{n}}\Big]^n\frac{R_o^{2n}}{1-n} \\ & \Big(\frac{\Gamma(\frac{3-n}{2})}{2\Gamma(\frac{5-n}{2})}\Big[R_o^{3-n}\frac{\Gamma(\frac{5-n}{2})\Gamma(2+n)}{\Gamma(\frac{5+n}{2})} - R_i^{3-n}{}_2F_1[\frac{1-n}{2},-n,\frac{5-n}{2},\frac{R_i^2}{R_o^2}]\Big]- \\ & \frac{1}{2}R_i^{1-n}(R_o^2-R_i^2){}_2F_1[\frac{1-n}{2},-n,1+\frac{1-n}{2},\frac{R_i^2}{R_o^2}]\Big) + 2\pi m_c L_c R_o^2\left[\frac{3n+1}{n}\frac{U_o R_o^2}{R_i^{\frac{3n+1}{n}}}\right]^n \end{aligned} \tag{6.18}$$

$$F_\tau = 2\pi\frac{m_f}{2-n}\Big(U_o R_o^2\delta^{-2}\frac{2n+1}{n}\Big)^n\Big[R_o^{2-n}\frac{\Gamma(\frac{4-n}{2})\Gamma(1+n)}{\Gamma(\frac{4+n}{2})} - R_i^{2-n}{}_2F_1[\frac{2-n}{2},-n,\frac{4-n}{2},\frac{R_i^2}{R_o^2}]\Big] \tag{6.19}$$

6.2.5 Radiation Analysis

As described by Colon et al. [90], a radiation heat transfer analysis was performed in the barrel section of the nozzle. The study takes into account the heat transfer from the nozzle walls to the filament material. The heat transfer increases the temperature of the filament as it moves towards the hot end resulting in a temperature greater than the room temperature T_{room}. The analysis yields an implicit solution for the initial temperature of the filament as shown in Equation 6.20.

$$ln\Big(\frac{T_h+T_{if}}{T_h-T_{if}}\Big) + 2tan^{-1}\Big(\frac{T_{if}}{T_h}\Big) = ln\Big(\frac{T_h+T_{room}}{T_h-T_{room}}\Big) + 2tan^{-1}\Big(\frac{T_{room}}{T_h}\Big) + 4T_h^3K\frac{L_N}{(U_{sz})} \tag{6.20}$$

where $K = \frac{\epsilon\sigma A_o}{\rho V_o C_s}$, $A_o = \pi D_o L$ and $V_o = \pi D_o^2 L/4$. Here ϵ is the emissivity, σ is the Stefan-Boltzmann constant, A_o is the surface area of the filament inside the nozzle, V_o is

the volume of the filament inside the nozzle, T_{if} is the initial filament temperature, T_{room} is the room temperature, T_h is the heater temperature, U_{sz} is the filament velocity, and L_N is the nozzle length. The initial temperature of the filament was calculated numerically and implemented within the melting model to calculate the initial filament temperature as a function of the filament velocity. This implementation is different from Colon et al. as he used a constant temperature for all the filament velocities. The goal is to improve the prediction accuracy of various nozzle diameters, processing temperatures, and materials.

6.2.6 Thermal and Mechanical Properties

The thermal and rheological properties of the ABS and PLA materials were obtained from work presented by Colon et al. [90]. The glass transition temperature T_g of the ABS material is 104.5 ^{o}C. For the PLA material, T_g is 58.9 ^{o}C while the melting temperature T_m is 150.9 ^{o}C.

The material properties are shown in Table B.1 [90]. It was assumed that the melt density is 90% of the solid density for an amorphous material and 80% for a semi-crystalline material [95, 96].

Table 6.2: Physical and mechanical properties of PLA and ABS.

Material Properties	PLA MatterHackers	ABS MG94
Melt density (ρ_m) $[kg/m^3]$	1000	954
Solid density (ρ_s) $[kg/m^3]$	1250 [97, 98]	1060 [99]
Specific heat (C_s) $[J/kg-K]$	1800 [97]	1850 [100]
Thermal conductivity (k_m) $[W/m-K]$	0.163 [101]	0.17 [99]
Heat of fusion (λ) $[J/kg]$	93600 [102]	-

6.2.7 Rheological Model

A time-temperature-superposition (TTS) was performed for both materials to find the shift factor at a reference temperature of 200 ^{o}C. The Arrhenius model was used for the PLA material, while the Williams-Landel-Ferry (WLF) model was used for the ABS material. The activation energy E_a for PLA is 80574.4 J/mol. The WLF constants for ABS are C_1=3.93791 and C_2=128.563 K. The Carreau-Yasuda, and the Power Law models were chosen for this work. The fitting parameters for the experimental values are shown in Table 6.3.

Table 6.3: Power law and Carreau-Yasuda fitting parameters. Values were taken from [90].

Material	Carreau-Yasuda Model					Power Law Model		
	η_o (Pa-s)	λ (s)	a (-)	b (-)	R^2	m (Pa-s)	n (-)	R^2
ABS	$1.325*10^4$	$8.675*10^{-2}$	0.4695	0.2847	0.9978	$4.977*10^4$	0.2847	0.9994
PLA	$3.546*10^3$	$3.333*10^{-2}$	0.8295	0.4287	0.9914	$2.206*10^4$	0.4287	0.995

where m is the consistency index, n is the power-law index, η_o is the zero-shear viscosity, and λ is the consistency. The power-law index is expressed as $(b-1)$ and a represents the width of the transition region between the zero-shear viscosity and the power-law region. These models were used to calculate the viscosity of the Osswald et al. model.

6.3 Results and Discussion

6.3.1 Experimental Data

Repeatability of Data

To verify the repeatability of the data, three runs were performed for a range of conditions. The ABS material was extruded using a nozzle diameter of 0.25 mm and 0.4 mm at a temperature of 200 ^{o}C and 230 ^{o}C. Figure 6.3 shows the experimental results for all the repetitions. Moreover, the standard deviation for both the filament velocity and filament force were also plotted. It can be observed from the figure that the results are consistent within the three runs. Repeatability of data was also found by another [103]. It can be noted that the standard deviation increased once the filament force exceeds a critical value for all the conditions. It is assumed that at this critical force, slippage between the feeder gears and the filament occurs. The higher the standard deviation, the more slippage occurs during extrusion of the filament.

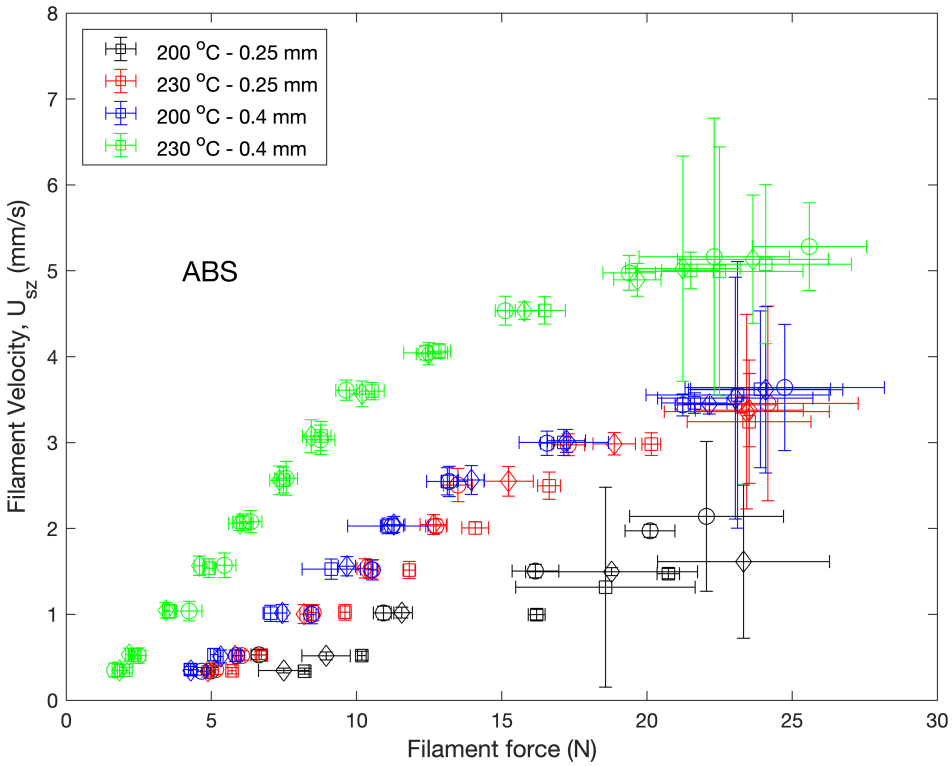

Figure 6.3: Repeatability of experimental data of ABS for a nozzle diameter of 0.25 mm and 0.4 mm at a heater temperature of 200 ^{o}C and 230 ^{o}C.

Measured velocity vs. Input Velocity

The measured filament velocity over the input velocity ($\frac{V_{measured}}{V_{input}}$) as a function of the filament force are shown in Figure 6.4 for ABS and Figure 6.5 for PLA. The line on both plots indicates the theoretical velocity ratio ($\frac{V_{measured}}{V_{input}} = 1$). When the ratio is lower than the theoretical value, it is expected that slippage in the driving gears occurs.

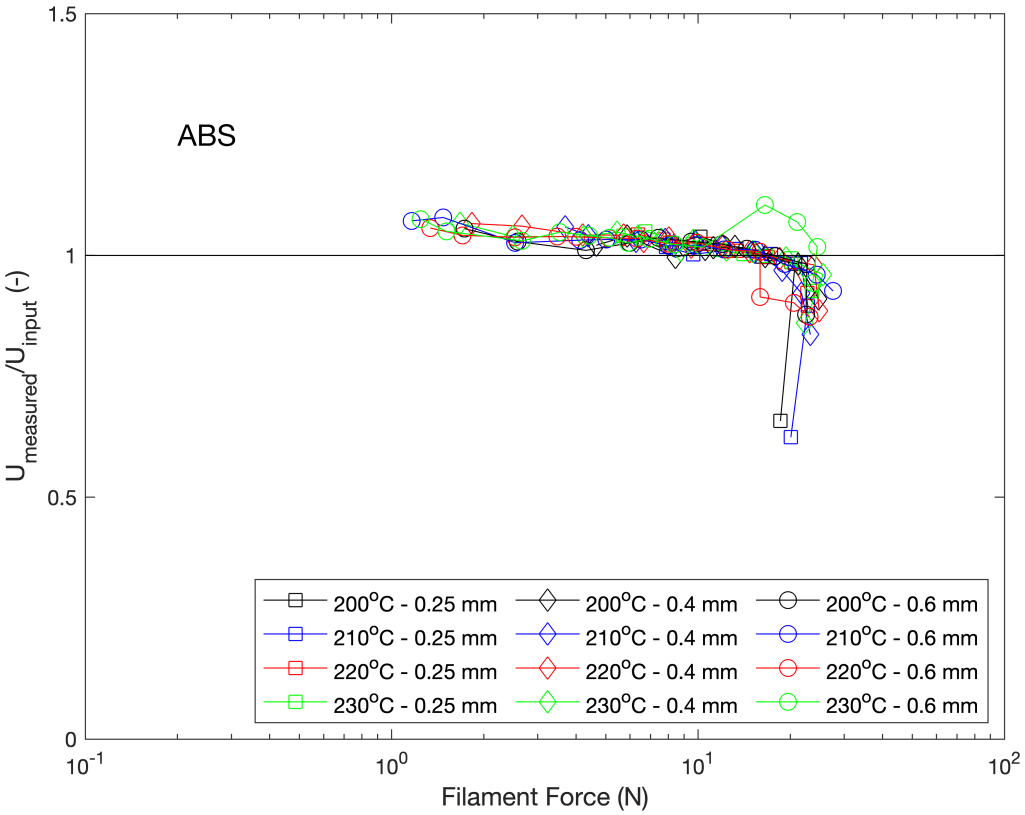

Figure 6.4: Ratio of measured filament velocity and input filament velocity for a range of heater temperatures and nozzle diameters for ABS material.

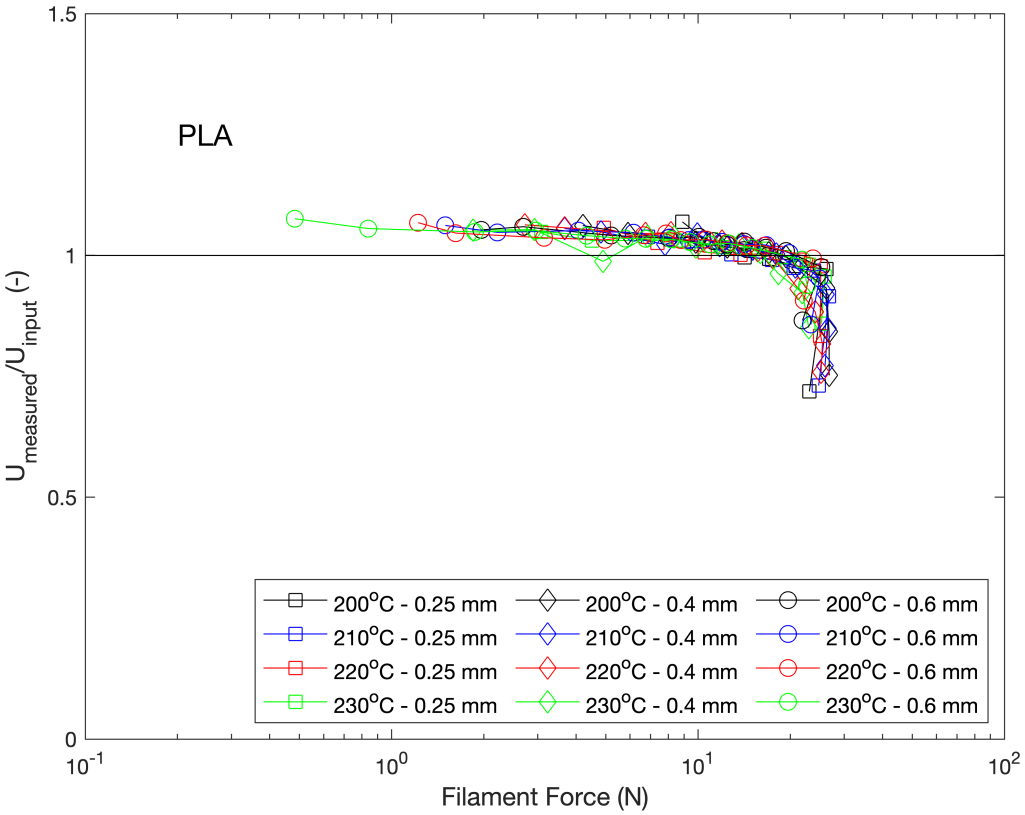

Figure 6.5: Ratio of measured filament velocity and input filament velocity for a range of heater temperatures and nozzle diameters for PLA material.

The deviation is observed at low forces due to the sensitivity of the force sensor [90]. A trend can be seen for both materials. It can be observed that when combining both the processing temperature and nozzle diameters, a transition in the ratio occurs. The decrease in ratio corresponds to slippage between the feeder gears and the filament material. It can be noted that for both materials that there is a critical force where the velocity ratio decrease. The experimental critical force is 16.8 N for ABS and 19 N for PLA. These forces were measured at the point where the velocity ratio reaches a value of 1. Others have also observed the slippage behavior [23, 26, 104, 105], some suggesting grinding of the filament material. The magnitude in force and velocity coincide with experimental data from literature [25, 26].

It can be observed that the critical force will be the same regarding the processing temperature and geometric parameters (nozzle diameters). The results also demonstrate that the critical force is material-dependent and is affected by the mechanical properties of the filament material. Following the process of Go et al. [25], the theoretical, critical force is calculated using Equation 6.21.

$$F_{filament} > \tau_{UT} A_{contact} \tag{6.21}$$

Where $F_{filament}$ is the filament force, τ_{UT} is the ultimate shear strength and $A_{contact}$ is the contact area between the filament and the feeder gear.

Go et. al [25] uses the ultimate tensile strength of the material to calculate the shear strength. The shear strength is approximated using the distortion energy theory for ductile materials where $\tau_{UT} = \sigma_{uts}/\sqrt{3}$. Using [100], the σ_{uts} for ABS is 20 MPa. Using [106], the σ_{uts} for PLA is 26.4 MPa. Using the distortion energy theory, the ultimate shear strength is 11.54 MPa for ABS and 15.23 MPa for PLA.

A bench experiment was performed to qualitatively determined the number of teeth in contact with the filament materials while extruding. The procedure consisted of marking the gear with ink and then place it in touch with the filament material. It was observed after several repetitions that 3 to 4 gear teeth were in contact with the filament. Later, the gear surface was photographed and scaled using Fiji [60], an open-source image processing software. Afterward, the area of the teeth in contact with the filament was calculated. On average, the area of the filament was 0.38 mm^2. Thus, the region corresponding to three teeth would be 1.14 mm^2 while the area for four teeth would be 1.52 mm^2. Using Equation 6.21, the critical force is calculated, resulting in the range of 13.15 N - 17.54 N for ABS and the range of 17.36 N - 23.14 N for PLA. The error percentage is between 4.2 % to 27.7 % for ABS and 9.4 % to 17.8 % for PLA, close to the value obtained experimentally.

When compared to Go et al., the surface area between the gear and the filament is $2.8mm^2$. Using this value, the critical filament force is calculated, resulting in 32.3 N for ABS and 42.6 N for PLA. When comparing the experimental critical force with the theoretical force, these are different in values. This difference can be in part to the area calculation performed by Go et al. The area is taken once the filament causes wear to the material. This means that the area is over the circumference of the filament material. This is true once the gear is under slippage for a time. However, when extrusion of the filament occurs, there is contact between a few teeth of the gear. For this reason, it is expected that the surface is smaller than the one calculated by Go et al. [25] as demonstrated previously.

Using the procedure described here is possible to calculate the critical force during the FFF process. This critical force indicates when slippage during extrusion will occur. This, in part, will be the critical parameter determining the maximum printing rate during extrusion.

6.3.2 Radiation Effects and Filament Temperature

The radiation effects on the filament temperature are discussed here. Figure 6.6 shows the filament initial temperature as a function of filament velocity for a range of heater temperatures. Notice that the data is graphed on a logarithmic scale. The material and nozzle diameter selected were ABS and 0.4 mm. The corresponding parameters were chosen to show the trend as the other conditions have similar behavior. It is observed that at a heater temperature of 230 ^{o}C, the filament temperature is 90 ^{o}C at low filament velocities. As the filament velocity increases, the filament temperature decreases to a temperature similar to the room temperature. At the same time, this behavior also occurs in the other heater temperatures. The only difference is that the filament temperature at low filament velocities decreases, which affects the heater temperature. This trend can be explained in the following

way. When the filament velocity is small, the radiation effects are higher as more time for the heat transfer occurs from the nozzle walls to the filament material. As the filament velocity increases, less time for the heat transfer occurs, resulting in a filament temperature closer to the room temperature.

Moreover, at a filament velocity of 10 mm/s, the material travels through the nozzle for approximately 1 second as the nozzle length is 10.2 mm. This time is not enough to raise the temperature significantly above the room temperature. The effect of the initial filament temperature can be observed when calculating the melt film thickness. The results will be discussed in the proceeding section.

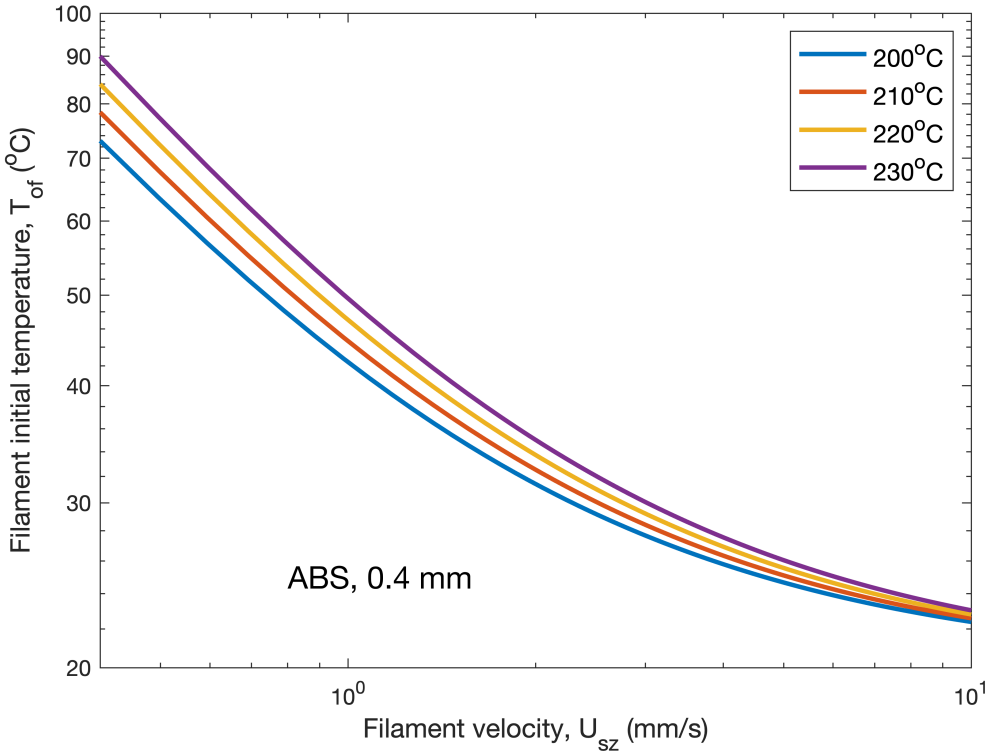

Figure 6.6: Filament initial temperature as a function of filament velocity for heater temperatures of (a) 200 ^{o}C, (b) 210 ^{o}C, (c) 220 ^{o}C, and (d) 230 ^{o}C. The material and nozzle capillary diameter are ABS and 0.4 mm. Calculations were made using $T_o = T_{room} = 21.1$ ^{o}C and $T_m = T_g = 104.5^o$C.

6.3.3 Melt Film Thickness

The effect of the filament velocity and temperature on the melt film thickness are discussed here. Figure 6.7 shows the melt film thickness using a constant filament initial temperature and using the radiation effects for the ABS material. For the comparison, a nozzle capillary diameter of 0.4 mm was used. The same trend happens for the rest of the materials and

nozzle diameters. Referring to equation 6.15, it can be noted that the material properties are constant. Subsequently, the terms that affect the melt film thickness are the initial filament temperature and the filament velocity. Using a constant filament temperature, the melt film thickness has a linear behavior as the only changing variable is the filament velocity. However, when incorporating the radiation effects, the filament temperature has a non-linear behavior. As a result, the melt film thickness is higher at lower filament velocities when introducing the radiation effects than at constant filament temperature. This, in part, results from the increase of heat transfer at low filament velocities. Therefore, higher filament initial temperature will result in higher melt film thickness.

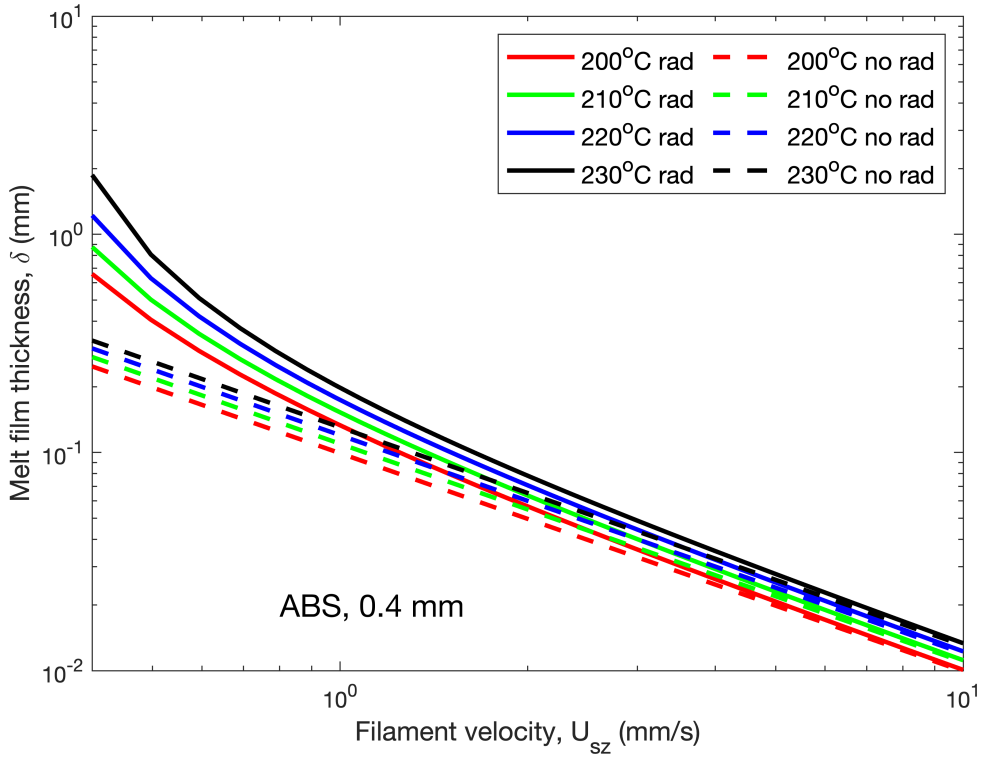

Figure 6.7: Melt film thickness as a function of filament velocity for heater temperatures of (a) 200 ^{o}C, (b) 210 ^{o}C, (c) 220 ^{o}C, and (d) 230 ^{o}C. The effect of radiation (rad) and without radiation (no rad) was studied. The material and nozzle capillary diameter are ABS and 0.4 mm. Calculations were made using $T_o = T_{room} = 21.1$ ^{o}C and $T_m = T_g = 104.5^o$C.

It is also be observed that at a filament velocity of 2 mm/s, both melt film thicknesses are similar in value. This means that at higher filament velocities, the radiation effect is not as significant. However, it is vital to consider this effect to predict the process of low filament velocities accurately.

6.3.4 Model Comparison: ABS

This section compares the acquired experimental data of ABS with the different FFF models. Figure 6.8 to Figure 6.10 shows the model comparison using a nozzle diameter of 0.25 mm, 0.4 mm, and 0.6mm respectively. The melting temperature used was the glass transition temperature ($T_m = T_g$) since it is the theoretical temperature at which an amorphous material flows. It is worth mentioning that the radiation effect was incorporated on both Colon et al. and Osswald et al. models. It can be noted that when comparing the Colon et al. model, with and without radiation effects, the filament force is smaller when incorporating the effect at the same filament velocity. During the comparison of the melting models, the viscosity of the Oswald et al. model was calculated using the Power Law model (Osswald w/ PL) and the Carreau-Yasuda model (Osswald w/ CY).

Looking at Figure 6.8, for a nozzle diameter of 0.25 mm, it can be seen that the model that fits the data better is the Osswald-Colon model. At a heater temperature of 200 ^{o}C and 210 ^{o}C, the model predicts well the filament force up to 20 N. At a heater temperature of 220 ^{o}C and 230 ^{o}C the model underestimate the filament force. The model is also able to predict the trend of the experimental data. The model proposed by Osswald et al. has a similar tendency when compared with the data. However, the filament force is overestimated for most of the heater temperatures. When comparing the rest of the models, these do not predict the data under the tested conditions.

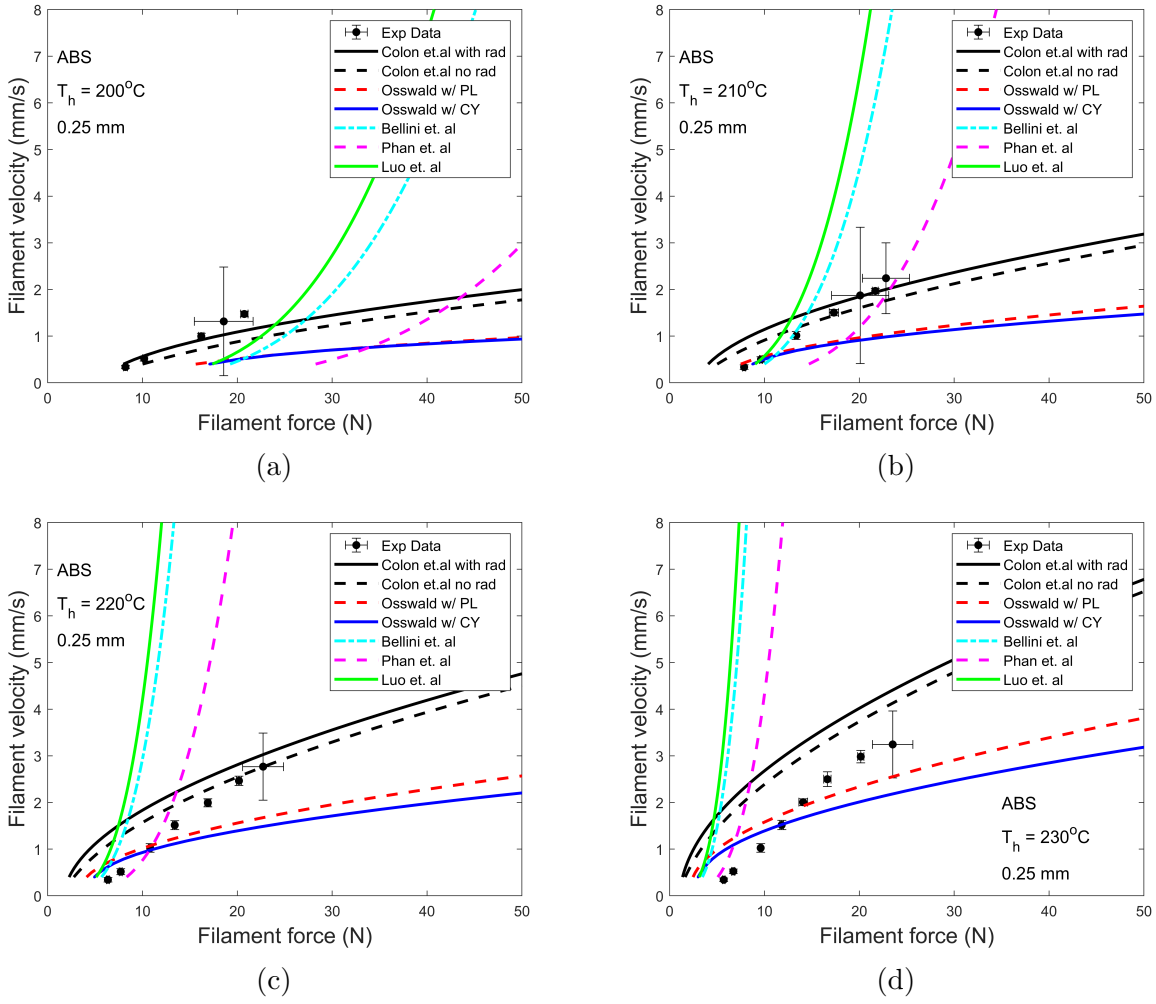

Figure 6.8: Comparison of experimental data and analytical models for ABS using a heater temperature of (a) 200 ^{o}C, (b) 210 ^{o}C, (c) 220 ^{o}C, and (d) 230 ^{o}C. The nozzle used has a capillary diameter of 0.25 mm. Calculations were made using $T_o = T_{room} = 21.1$ ^{o}C and $T_m = T_g = 104.5^o$C.

Figure 6.9 shows the data for a nozzle diameter of 0.4 mm. The Osswald-Colon is able to predict up to a filament force of approximately 10 N for a heater temperature of 200 ^{o}C , 210 ^{o}C , and 220 ^{o}C. Looking at a heater temperature of 230 ^{o}C the Osswald-Colon model predicts the filament force up to a value of 25 N. The models by Bellini et. al and Luo et. al are able to predict the filament force up to a value of 10 N for $T_h = 210^o$C and up to 5 N for both $T_h = 220^o$C and $T_h = 230^o$C. Phan et. al model is able to predict the filament force up to a value of 5 N for $T_h = 230^o$C.

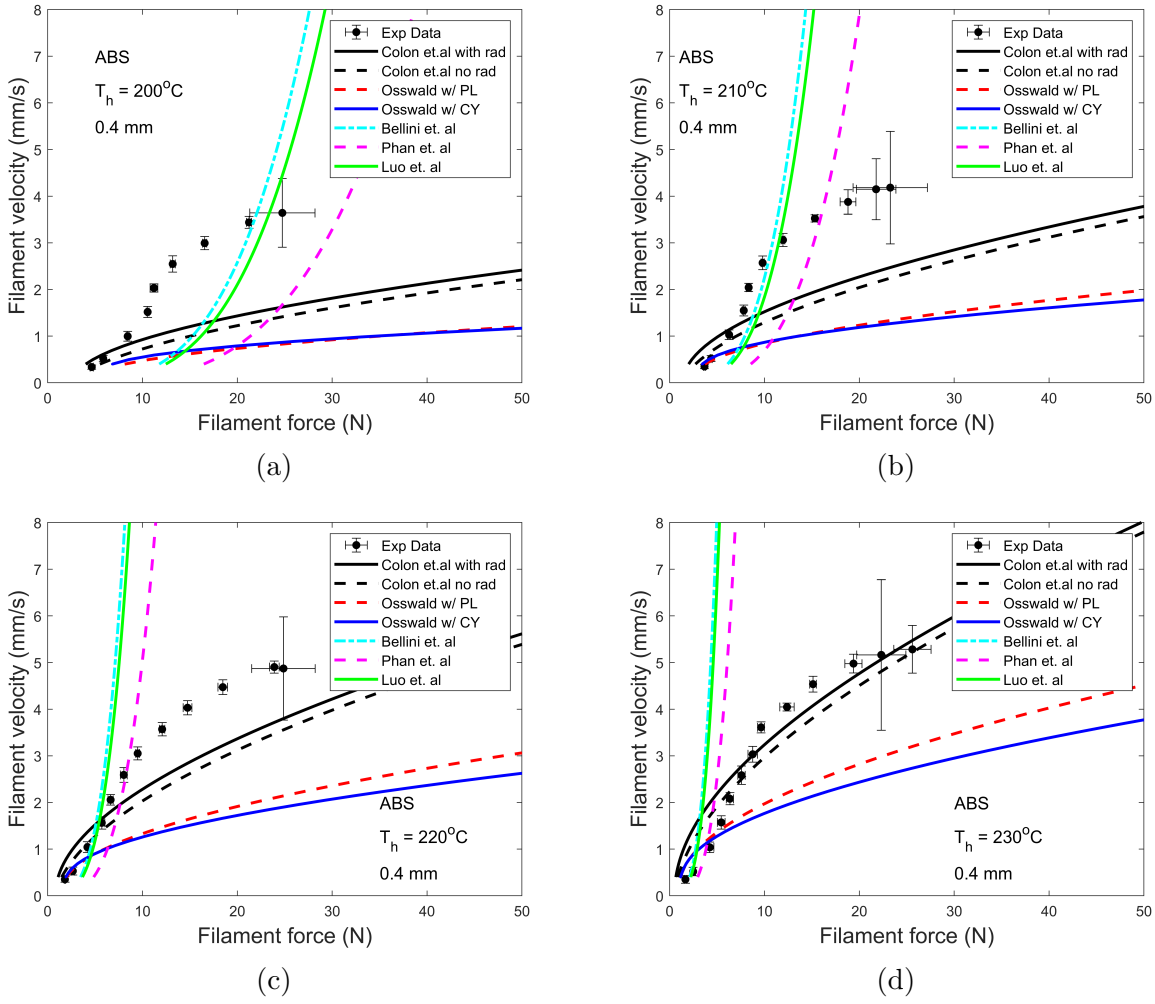

Figure 6.9: Comparison of experimental data and analytical models for ABS using a heater temperature of (a) 200 ^{o}C, (b) 210 ^{o}C, (c) 220 ^{o}C, and (d) 230 ^{o}C. The nozzle used has a capillary diameter of 0.4 mm. Calculations were made using $T_o = T_{room} = 21.1$ ^{o}C and $T_m = T_g = 104.5^o$C.

Figure 6.10 shows the data for a nozzle diameter of 0.6 mm. At a temperature of 200 ^{o}C, the models are not able to predict the same behavior as the experimental data. Even though the Osswald-Colon and Osswald et al. models have the same trend, they can predict up to a filament force of 3 N. At a heater temperature of 230 ^{o}C, most of the models can predict the filament force up to 7 N. At a temperature of 230 ^{o}C the Osswald-Colon can predict the data up to 25 N.

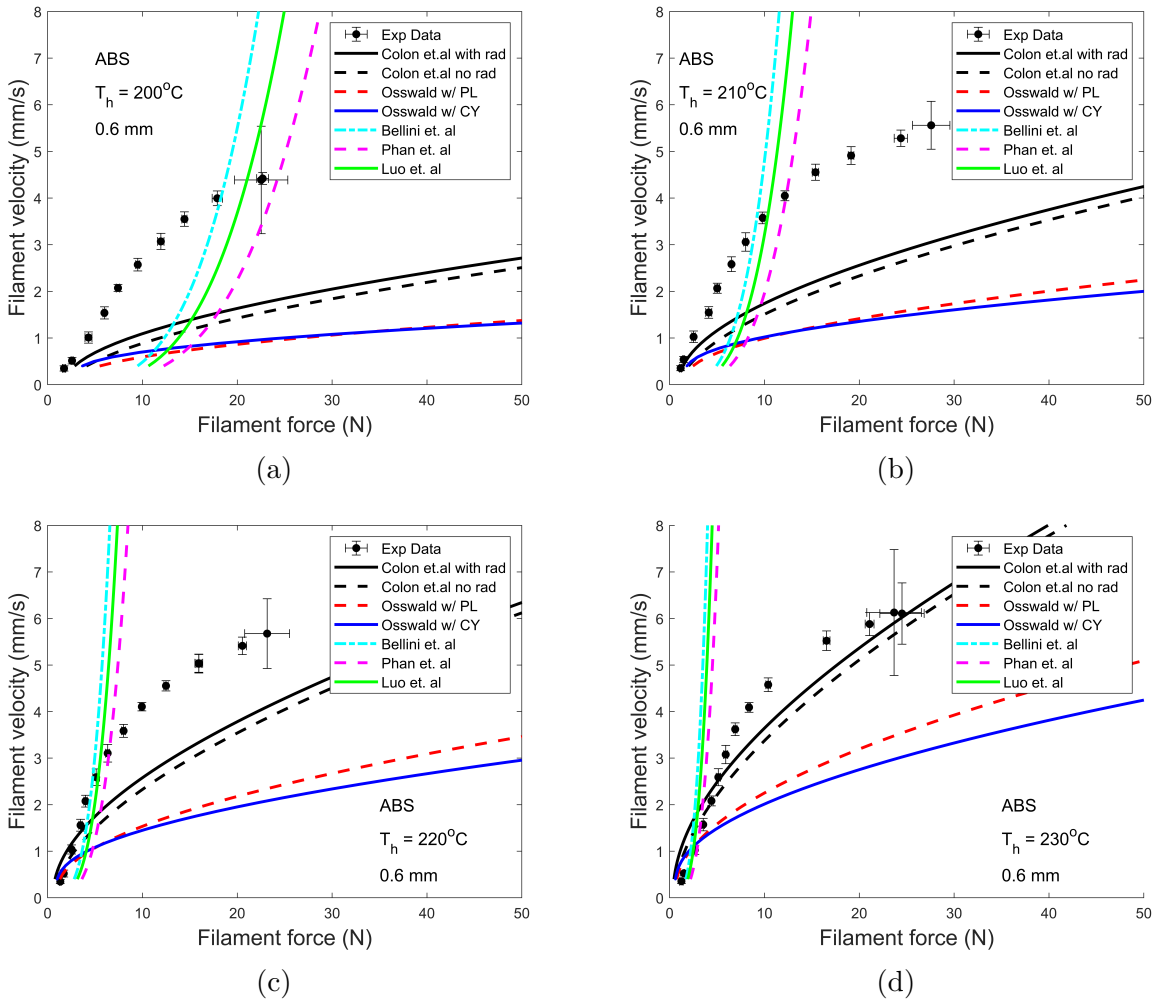

Figure 6.10: Comparison of experimental data and analytical models for ABS using a heater temperature of (a) 200 ^{o}C, (b) 210 ^{o}C, (c) 220 ^{o}C, and (d) 230 ^{o}C. The nozzle used has a capillary diameter of 0.6 mm. Calculations were made using $T_o = T_{room} = 21.1$ ^{o}C and $T_m = T_g = 104.5^o$C.

It was observed that the models proposed by Bellini et al., Phan et al., and Luo et al. are best suited for predicting the filament force at higher temperatures. One reason for this is that these models assumed a melt pool of material in the nozzle. This melt pool is likely to present inside the nozzle at high temperatures and low filament velocities. The assumption of a melt pool allows explaining why Bellini et al., Phan et al., and Luo et al. require a smaller force to print at higher printing rates. As the temperature increases, the viscosity of the materials decreases. This, in part, produces that the material flow under less applied forces. As observed for the lower temperatures, the force required for extrusion is higher than at higher printing temperatures. Therefore, at lower temperatures is less likely that a melt pool is present inside the printing nozzle. The optimal parameters for this to occur

happens at high printing temperatures and low filament velocities.

As the Osswald-Colon model used radiation heat transfer within the nozzle, predicting the process within a broader range of conditions is possible. Expected experimental data was acquired overall. At higher heater temperature, the filament requires significantly less force to extrude at the corresponding filament velocity.

6.3.5 Model Comparison: PLA

This section compares the acquired experimental data of PLA with the different FFF models. Figure 6.11 to Figure 6.13 shows the model comparison using a nozzle diameter of 0.25 mm, 0.4 mm, and 0.6mm respectively. Since PLA is a semi-crystalline material, the melting temperature used was $T_m = 150.9\ ^oC$. Compared to ABS, the melting temperature is significantly higher. This means that the temperature differences in the Stefan condition equation (Equation 6.15) are smaller. Smaller temperature differences will result in a small/thin melt film thickness.

In Figure 6.11 it can be seen that the model from Luo et al. and Bellini et al. best described the data at lower heater temperatures. On the other hand, Phan et al. model best represent the data at a heater temperature of 230^oC. Thus, even though Osswald et al. and Osswald-Colon models have a similar trend, they fail to predict the data by overestimating the filament force at all the heater temperatures.

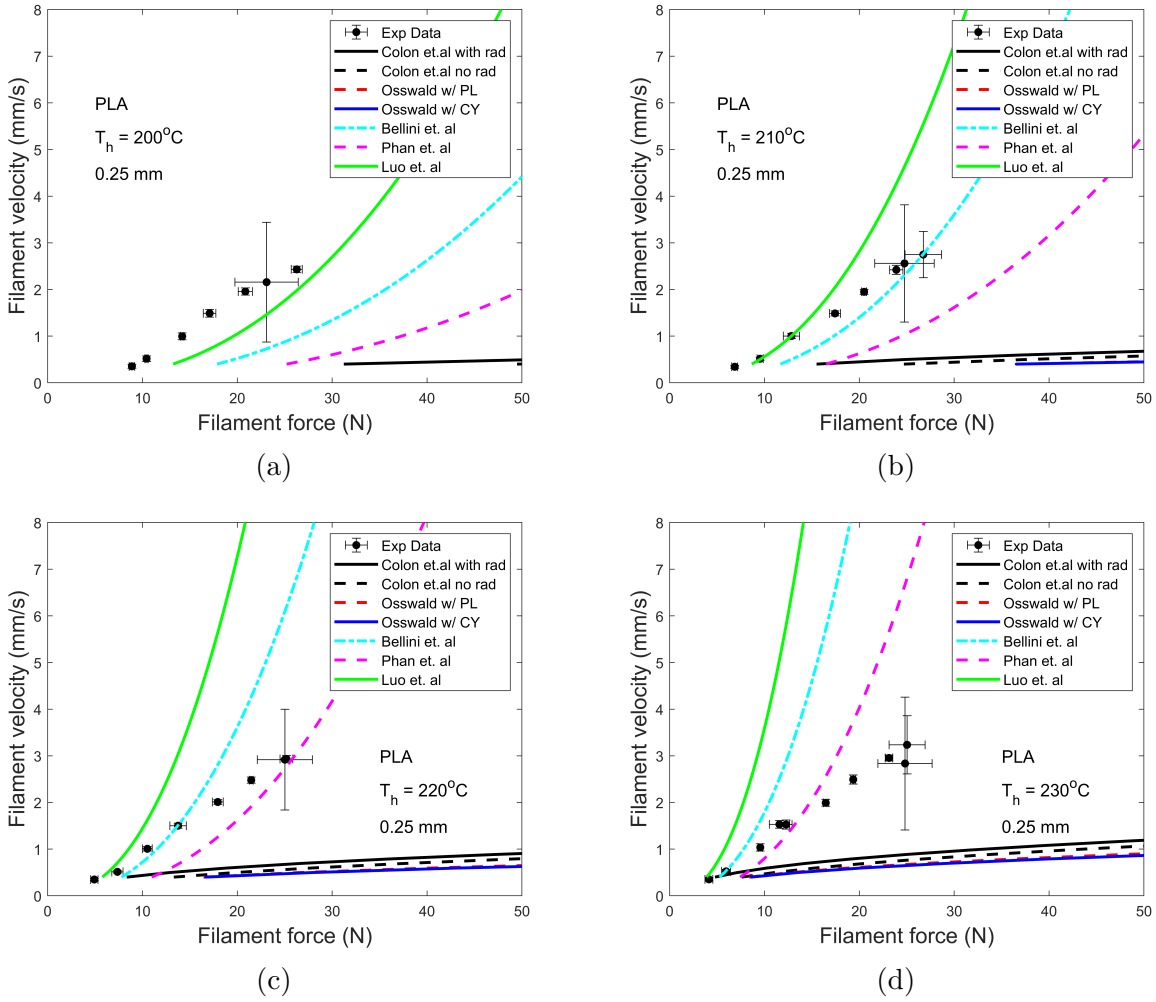

Figure 6.11: Comparison of experimental data and analytical models for PLA using a heater temperature of (a) 200 ^{o}C, (b) 210 ^{o}C, (c) 220 ^{o}C, and (d) 230 ^{o}C. The nozzle used has a capillary diameter of 0.25 mm. Calculations were made using $T_o = T_{room} = 21.1$ ^{o}C and $T_m = 150.9^o$C.

Figure 6.12 shows the results for a nozzle diameter of 0.4 mm. For a heater temperature of 200 ^{o}C and 210 ^{o}C, Bellini et al. and Luo et al. models described up to 20 N and 10 N, respectively. At a temperature of 220 ^{o}C, Bellini et al. best described the process. At a temperature of 230 ^{o}C, the only model that predicts the process is Bellini et al. up to a filament force of 5 N. Again, the models by Osswald-Colon and Osswald et al. fail to predict the process by overestimating the filament force.

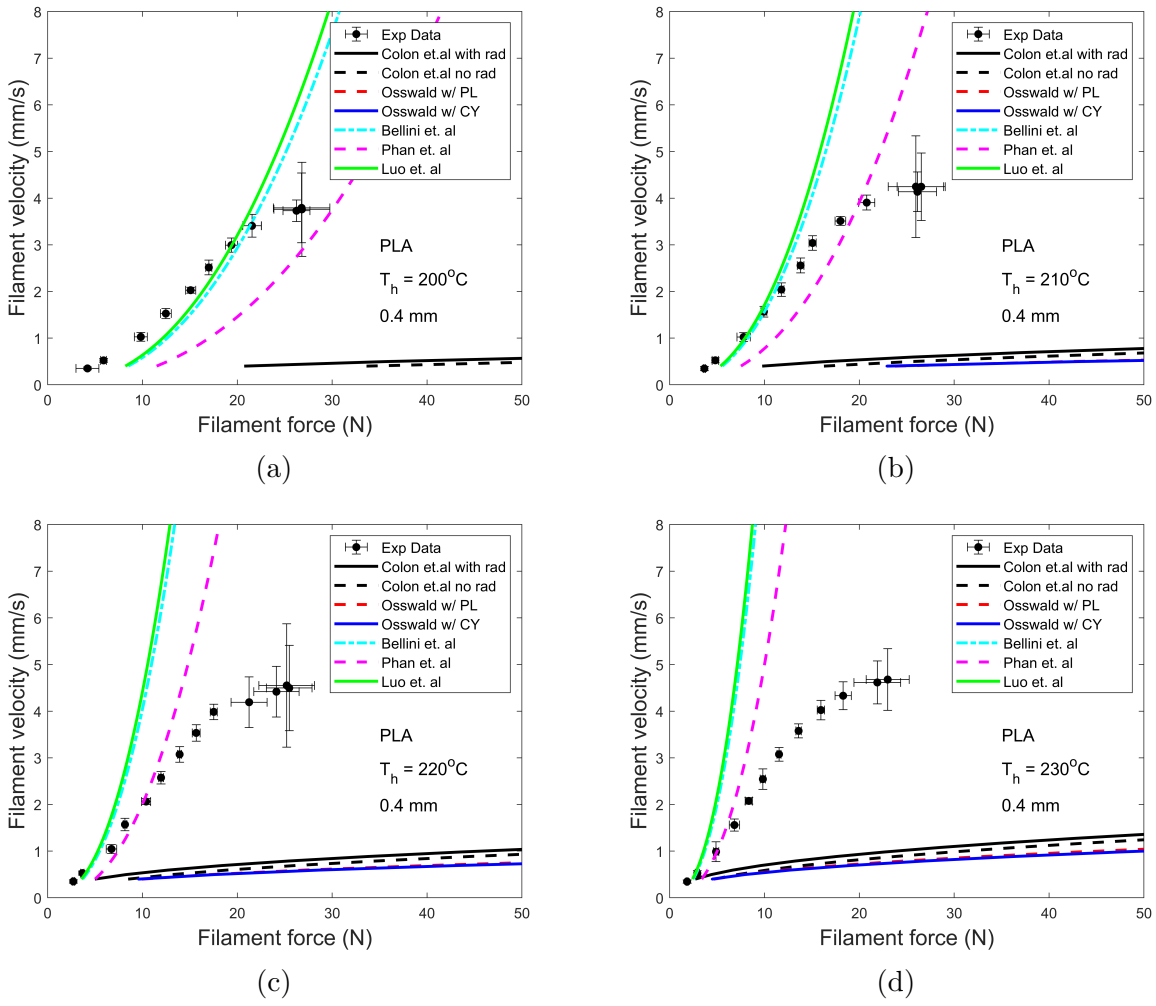

Figure 6.12: Comparison of experimental data and analytical models for PLA using a heater temperature of (a) 200 ^{o}C, (b) 210 ^{o}C, (c) 220 ^{o}C, and (d) 230 ^{o}C. The nozzle used has a capillary diameter of 0.4 mm. Calculations were made using $T_o = T_{room} = 21.1$ ^{o}C and $T_m = 150.9^o$C.

Figure 6.13 shows the results for a nozzle diameter of 0.6 mm. Again, the models by Bellini et al., Phan et al., and Luo et al. best describe the process. The models can predict up to 15 N and 10 N for a heater temperature of 200 ^{o}C and 210 ^{o}C. At a temperature of 220 ^{o}C and 230 ^{o}C the models can predict up to a filament force of 5 N. Similar to the other nozzle diameters, the models by Osswald-Colon and Osswald et al. fail to predict the filament force for all the heater temperatures.

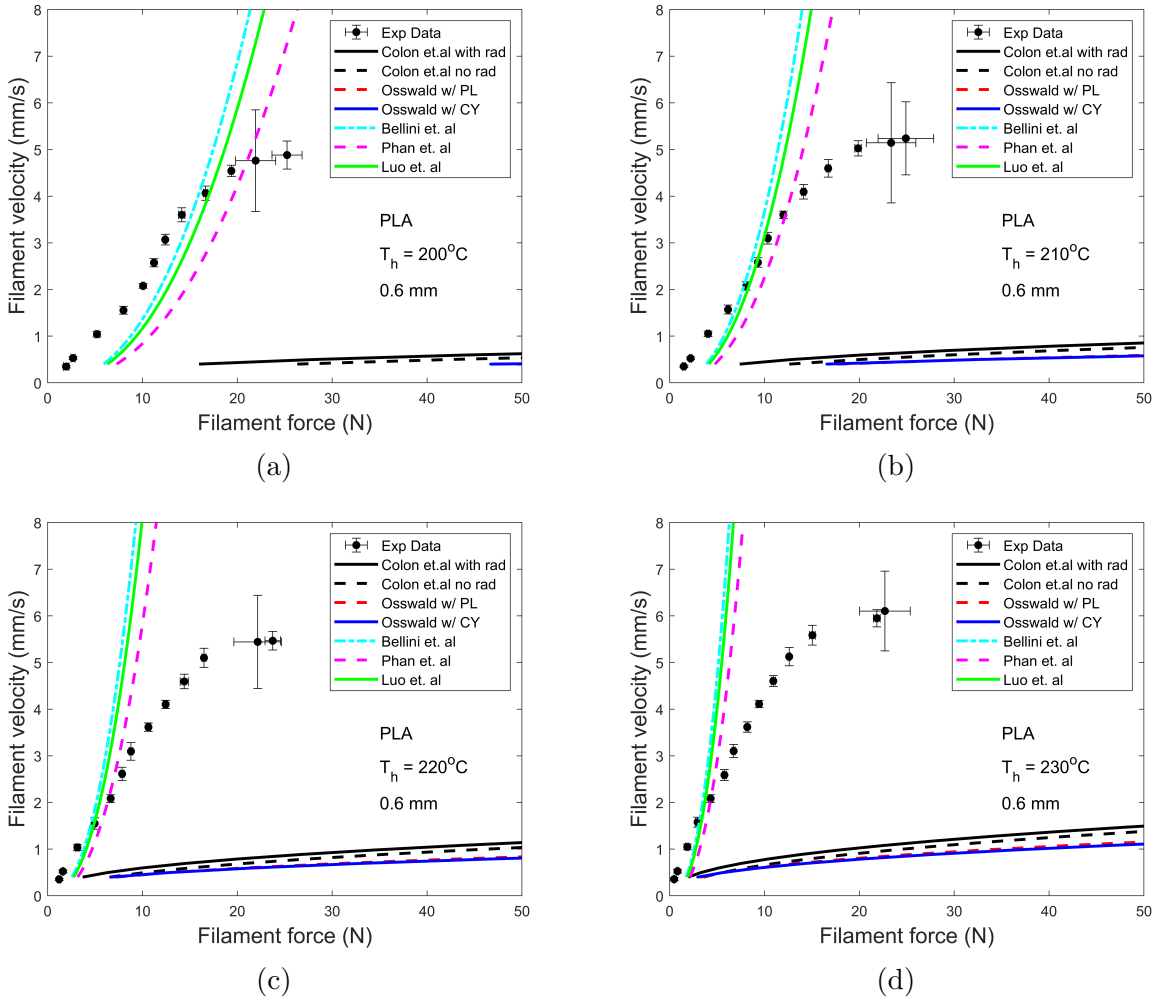

Figure 6.13: Comparison of experimental data and analytical models for PLA using a heater temperature of (a) 200 ^{o}C, (b) 210 ^{o}C, (c) 220 ^{o}C, and (d) 230 ^{o}C. The nozzle used has a capillary diameter of 0.6 mm. Calculations were made using $T_o = T_{room} = 21.1$ ^{o}C and $T_m = 150.9^o$C.

Compared to the ABS material, the model proposed by Osswald-Colon fails to predict the process for the given conditions. Many factors can cause the model not to predict the filament force. One factor can be the mechanical properties used for the model. As some of the properties were taken from literature, this may have affected the results. A more detailed analysis is required to obtain the mechanical properties of the PLA material. At the same time, it is suggested to performed additional rheological analysis to have a broader range of temperatures for the shift factor determination [90]. It has to be taken into account that the PLA has a non-zero heat of fusion which also affects the melt film thickness value.

It was observed that when using $T_m = T_g$ for the PLA material, the model had a good fit with the experimental data similar to ABS. This condition was not used to compare the

data since PLA has a defined melting temperature instead of ABS. Even though the non-linked molecules can flow once the material reaches T_g, this is not enough to break the links entirely. Breakage occurs once the material reaches its T_m. Using a smaller T_m will result in a smaller temperature difference when calculating the melt film thickness for the respective filament velocity. This change will increase the melt film thickness value and subsequently will decrease the analytical filament force. Nonetheless, it is essential to understand how varying the parameters affect the final analytical result.

6.4 Conclusion

Filament velocity and filament force data were acquired using a customized FFF printer. Data were collected for two materials, three nozzle diameters, and four heater temperatures. The data coincide in magnitude with data found in the literature. Moreover, five melting models were used to compare with the experimental data. Repeatability between test conditions was observed for the materials. When plotting the standard deviations is was clear that there is a critical force where the standard deviation increased.

Furthermore, the critical force value was found when plotting the ratio between the measured velocity and the input velocity as a function of filament force. From the data, it can be deduced that the critical force will be the same no matter the nozzle geometry and processing temperature. Instead, it will be dependent on the contact area of the fed gear and the shear strength of the material. When calculating the critical force analytically, the value was close in magnitude to the one found experimentally.

The radiation effects on the filament temperature were successfully implemented in both the Osswald et al. model and the improved Osswald model introduced by Colon et al. The radiation effects influence the filament temperature, subsequently affecting the melt film thickness value. Therefore, temperature values for the filament were expected. At low filament velocities, the filament temperature was higher than at higher filament velocity. When comparing the melt film thickness with radiation and without radiation effects, values were similar in magnitude after exceeding a filament velocity of 2 mm/s. After a filament velocity of 2 mm/s, both temperatures were very close.

The Osswald-Colon model, including the radiation effects, approximated best the ABS data for most of the conditions from all the melting models used. As the nozzle diameter increased, the model was able to predict the process for lower filament forces. The models by Bellini et al., Phan et al., and Luo et al. were able to predict the process for higher heater temperatures up to a filament force of 5 N. For PLA, the model by Osswald-Colon failed to predict the process for all the conditions overestimating the filament force. Here, the models by Luo et al. and Bellini et al. were able to predict the process more accurately. Suggestions were given to verify the accuracy of the PLA material using the model described by Colon et. al.

6.5 Acknowledgement

The authors gratefully acknowledge George Halunen for the data acquisition. The authors would also like to acknowledge John Estela for this technical input on the materials.

7. Future Work

It is suggested that a study to understand the in-situ melting and printing during the FFF process should be done. This can be achieved by using the phase-contrast imaging equipment located at different national laboratories. Submission of an Advanced Photon Source (APS) proposal is recommended to study the process's melting kinetics. As the FFF nozzle is made out of aluminum and other dense materials, laboratory-size computed tomography equipment does not possess the energy needed to observe the density change through the metal nozzle. As the printing nozzles vary in size and shape, a parametric study should be performed to understand the melting behavior over a range of printing conditions.

Improvement of the fused filament fabrication melting model is suggested. It is suggested that the following boundary condition: $u_r^* = (-U_o) * sin(\alpha)$ at $z = \delta$ should be used. This improvement would account for the velocity component in the r-direction resulting from the filament velocity due to the nozzle angle. It is suggested to first derived the solution assuming the material is a Newtonian fluid. This assumption will ease the mathematical derivation and help understand how the change of boundary conditions will affect the result of the analytical model. It is suggested that afterward, the implementation of shear-thinning behavior should be addressed.

It is suggested that more experiments should be center on accurately determined the contact area between the feeding gear and the filament material. Moreover, an analysis should be performed using different feeding geometries (gears or pulleys) to understand how the critical force changes as a function of the contact area and gear geometry. To accurately predict the critical force during the FFF process, it is suggested that experiments should be centered on determining the contact area between the feeding gear and the filament material.

7.1 Publication Overview

The following publications have resulted during the process of this work.

1. J. L. Colon Quintana et al. "Application of the stress interaction failure criterion in platelet composite compression molded parts". In: *Polymer Composites* (2021), pp. 1–12. DOI: .https://doi.org/10.1002/pc.26084

2. J. L. Colon Quintana et al. "Implementation of Shear Thinning Behavior in the Fused Filament Fabrication Melting Model: Analytical Solution and Experimental Valida-

tion". In: *Additive Manufacturing* 37 (2021). DOI: https://doi.org/10.1016/j.addma.2020.101687

3. J. L. Colon Quintana et al. "Viscoelastic properties of fused filament fabrication parts". In: *Additive Manufacturing* 28 (2019), pp. 704–710

4. J. Puentes et al. "Moduli development of epoxy adhesives during cure". In: *Polymer Testing* 77 (2019), pp. 54–61. DOI: https://doi.org/10.1016/j.polymertesting.2019.04.010

5. J. L. Colon Quintana et al. "Experimental Study of Particle Migration in Polymer Processing". In: *Polymer Composites* (2019). DOI: DOI10.1002/pc.25018

6. J. L. Colon Quintana et al. "Observed Particle Migration During Processing of Polypropylene with Glass Beads". In: *Antec 2018* (2018)

Relevant Publications:

1. J. L. Colon Quintana et al. "Study of Thermomechanical Properties of an Al-Zn-Based Composite Reinforced with Dodecaboride Particles". In: *Advances in Materials Science and Engineering* (2016). DOI: {https://doi.org/10.1155/2018/2975234}

2. S. L. Zelinka et al. "Cell Wall Domain and Moisture Content Influence Southern Pine Electrical Conductivity". In: *Wood and Fiber Science* (2015), pp. 54–61. URL: {https://www.fs.usda.gov/treesearch/pubs/52590}

As part of this work, the author has been working together and supervising visiting scholars. These were:

- Friederike Burke, University of Wisconsin, Madison: Melting Mechanisms during Fused Filament Fabrication - Effects of Nozzle Angle and Material Properties

- Nils Kroschel, Friedrich-Alexander Universitat Erlangen-Nurnberg: Analysis of the Fused Filament Fabrication Melting Model using X-ray Computed Tomography

The unique collaboration was performed with Nancy Granda and Stefan Heimer. They performed review and correctness of mathematical model and derivation.

Bibliography

[1] Tim A. Osswald, John Puentes, and Julian Kattinger. "Modelling Material Extrusion for Additive Manufacturing Applications". In: 22 (2018), pp. 51–59.

[2] J. F. Rodríguez, J. P. Thomas, and J. E. Renaud. "Mechanical behavior of acrylonitrile butadiene styrene fused deposition materials modeling". In: *Rapid Prototyping Journal* 9.4 (2003), pp. 219–230.

[3] *Mastering Cura*. Ultimaker. URL: `https://ultimaker.com/en/resources/21932-mastering-cura`.

[4] T. Mulholland, S. Goris, J. Boxleitner, T. A. Osswald, and N. Rudolph. "Fiber orientation effects in Fused Filament Fabrication of air-cooled heat exchangers". In: *Additive Manufacturing of Composites and Complex Materials* 70 (2018).

[5] T. Mulholland, S. Goris, J. Boxleitner, T. A. Osswald, and N. Rudolph. "Process-Induced Fiber Orientation in Fused Filament Fabrication". In: *Journal of Composite Science* 2 (2018).

[6] P. Geng, J. Zhao, W. Wu, W. Ye, Y. Wang, S. Wang, and S. Zhang. "Effects of extrusion speed and printing speed on the 3D printing stability of extruded PEEK filament". In: *Journal of Manufacturing Processes* 37 (2019), pp. 266–273.

[7] H. Xia, J. Lu, and G. Tryggavason. "Fully Resolved Numerical Simulations of Fused Deposition Modeling. Part IISolidification, Residual Stresses, and Modeling of the Nozzle". In: *Rapid Prototyping Journal* 24 (2018).

[8] Gerardo A Mazzei Capote. "Defining a failure surface for Fused Filament Fabrication parts using a novel failure criterion". Master thesis. Madison, WI: University of Wisconsin- Madison, 2018.

[9] B. Rankouhi, S. Javadpour, F. Delfanian, and T. Letcher. "Failure Analysis and Mechanical Characterization of 3D Printed ABS With Respect to Layer Thickness and Orientation". In: *Journal of Failure Analysis and Prevention* 16 (2016).

[10] E. Stammers and W. J. Beek. "The Melting of a Polymer on a Hot Surface". In: *Polymer Engineering and Science* 9.1 (1967).

[11] M. Mansour Mbow, P. Rene Marin, and F. Pourroy. "Extruded diameter dependence on temperature and velocity in the fused deposition modeling process". In: *Progress in Additive Manufacturing* (2020).

[12] Z. Quan, Z. Larimore, X. Qin, J. Yu, M. Mirotznik, J-H. Byun, Y. Oh, and T-W Chou. "Microstructural characterization of additively manufactured multi-directional preforms and composites via X-ray micro-computed tomography". In: *Composites Science and Technology* 131 (2016).

[13] J. Y. Wang, D. D. Xu, W. Sun, S. M. Du, J. J. Guo, and G. J. Xu. "Effects of nozzle-bed distance on the surface quality and mechanical properties of fused filament fabrication parts". In: *IOP Conference Series: Materials Science and Engineering* 479 (2019).

[14] A. Du Plessis, S. G. Le Roux, and F. Steyn. "Quality Investigation of 3D Printer Filament Using Laboratory X-Ray Tomography". In: *3D Printing and Additive Manufacturing* 3 (2016).

[15] B. B. Shahriar, C. France, N. Valerie, C. Arthur, and G. Christian. "Toward improvement of the properties of parts manufactured by FFF (Fused Filament Fabrication) through understanding the influence of temperature and rheological behaviour on the coalescence phenomenon Bakrani". In: *AIP Conference Proceedings* (2017).

[16] S. B. Balani, F. Chabert, V. Nassiet, and A. Cantarel. "Influence of printing parameters on the stability of deposited beads in fused filament fabrication of poly(lactic) acid". In: *Additive Manufacturing* 25 (2018), pp. 112–121.

[17] Lukas J. L. Duddleston, Kaitlyn Woznick, Carsten Koch, Gerardo Mazzei Capote, Natalie Rudolph, and Tim A. Osswald. "Extrudate Mass Flow Rate Analysis in Fused Filament Fabrication (FFF): A Cursory Investigation of the Effects of Printer Parameters". In: *ANTEC 2017* (2017), pp. 43–48.

[18] Anna Bellini, Selcuk Guceri, and Maurizio Bertoldi. "Liquefier Dynamics in Fused Deposition". In: *Journal of Manufacturing Science and Engineering* 126.2 (2004), p. 237.

[19] H. S. Ramanath, C. K. Chua, K. F. Leong, and K. D. Shah. "Melt flow behaviour of poly-ϵ-caprolactone in fused deposition modelling". In: *Journal of Materials Science: Materials in Medicine* 19.7 (2008), pp. 2541–2550.

[20] Brian N. Turner and Scott A. Gold. "A review of melt extrusion additive manufacturing processes: II. Materials, dimensional accuracy, and surface roughness". In: *Rapid Prototyping Journal* 21.3 (2015), pp. 250–261.

[21] Blake P. Heller, Douglas E. Smith, and David A. Jack. "Effects of extrudate swell and nozzle geometry on fiber orientation in Fused Filament Fabrication nozzle flow". In: *Additive Manufacturing* 12 (2016), pp. 252–264.

[22] C. Luo, X. Wang, K. B. Migler, and J. E. Seppala. "Upper bound of feed rates in thermoplastic material extrusion additive manufacturing". In: *Additive Manufacturing* (2019).

[23] V. Nienhaus, K. Smith, D. Spiehl, and E. Dorsam. "Investigation on nozzle geometry in fused filament fabrication". In: *Additive Manufacturing* 28 (2019), pp. 711–718.

[24] T. J. Coogan and D. O. Kazmer. “In-line rheological monitoring of fused deposition modeling”. In: *Journal of Rheology* 63 (2019), pp. 141–155.

[25] J. Go, S. N. Schiffres, A. G. Stevens, and A. J. Hart. “Rate limits of additive manufacturing by fused filament fabrication and guidelines for high-throughput systems design”. In: *Additive Manufacturing* 16 (2017), pp. 1–11.

[26] M. P. Serdeczny, R. Comminal, D. B. Pedersen, and J. Spangenberg. “Experimental and anlaytical study of thepolymer melt flow through the hot-end in material extrusion additive manufacturing”. In: *Additive Manufacturing* 32 (2020).

[27] N. W. Hale and R. Viskanta. “Photographic observation of the solid-liquid interface motion during melting of a solid heated from an isothermal vertical wall”. In: *Letters in Heat and Mass Transfer* 5 (1978).

[28] E. M. Mount and C. I. Chung. “Melting Behavior of Solid Polymer on a Metal Surface at Processing Conditions”. In: *Polymer Engineering and Science* 18 (1978).

[29] W. C. Bushko and V. K. Stokes. “Solidification of Thermoviscoelastic Melts. Part I: Formulation of Model Problem”. In: *Polymer Engineering and Science* 35 (1995).

[30] Tim A. Osswald. *Understanding Polymer Processing, Processes and Governing Equations*. Hanser Publishers, 2011. ISBN: 9781569904725.

[31] *Semi-Crystalline Polymers*. RTP Co. URL: {https://www.rtpcompany.com/products/high-temperature/semi-crystalline-polymers/}.

[32] Tim A. Osswald and Georg Menges. *Materials Science of Polymers for Engineering, Third Edition*. Hanser Publishers, Munich and Hansen Publications, Cincinnati, 2012. ISBN: 9781569905142.

[33] Tim A. Osswald and N. Rudolph. *Polymer Rheology, Fundamentals and Applications*. Hanser Publishers, Munich and Hanser Publications, Cincinnati, 2015. ISBN: 9781569905173.

[34] W. P. Cox and E. H. Merz. “Correlation of dynamic and steady flow viscosities”. In: *Journal of Polymer Science* 28 (1958), pp. 619–622.

[35] V. W. Ostwald. “Ueber die Geschwindigkeitsfunktion der Viskosität disperser Systeme. I.” In: 36.99 (1925).

[36] A. de Waale. In: *Oir and Color Chem. Assoc. Journal* 6.33 (1923).

[37] T. A. Osswald and J. P. Hernandez-Ortiz. *Polymer Processing Modelling and Simulation*. Hanser, 2006. ISBN: 9783446403819.

[38] P. Cebe, D. Thomas, J. Merfeld, B. P. Partlow, D. L. Kaplan, R. G. Alamo, A. Wurm, E. Zhuravlev, and C. Schick. “Heat of fusion of polymer crystals by fast scacnning calorimetry”. In: *Polymer* 126 (2017).

[39] *Molar Volume and Density of Polymers*. Polymer Properties Database. URL: {https://polymerdatabase.com/polymer\%20physics/MolarVolume.html}.

[40] V. Cholodovych and W. J. Welsh. *Densities of Amorphous and Crystalline Polymers*. Springer, New Youk, NY, 2007. ISBN: 9780387312354.

[41] *Solid Density vs. Melt Density*. Beaumont. URL: {https://www.beaumontinc.com/solid-density-vs-melt-density/}.

[42] Zehev Tadmor and Costas G. Gogos. *Principles of Polymer Processing, Second Edition*. John Wiley & Sons. Inc., Publication, 2006. ISBN: 0471387703.

[43] D. G. Baird and D. I. Collias. *Polymer Processing Principles and Design, Second Edition*. John Wiley $ Sons, Inc., 2014. ISBN: 9780470930588.

[44] R. Ketcham. *X-ray Computed Tomography*. Geochemical Instrumentation and Analysis. URL: {https://serc.carleton.edu/research_education/geochemsheets/techniques/CT.html}.

[45] Committee on the Mathematics and National Reserach Council Physics of Emerging Dynamic Biomedical Imaging. *Mathematics and Physics of Emerging Biomedical Imaging*. 1996. ISBN: 0309552923.

[46] In: ().

[47] Nils Kroschel. "Analysis of the Fused Filament Fabrication Melting Model using X-ray Computed Tomography". 2019.

[48] A. Murphy. *Beam hardening*. Radiopaedia. URL: {https://radiopaedia.org/articles/beam-hardening?lang=us}.

[49] D. D. Phan, Z. R. Swain, and M. E. Mackay. "Rheological and heat transfer effects in fused filament fabrication". In: *Journal of Rheology* 62 (2018).

[50] F. N. Cogswell. "Converging flow of polymer melts in extrusion dies". In: *Polymer Engineering and Science* 12.1 (1972).

[51] Gerardo A Mazzei Capote, Natalie M Rudolph, Paul V Osswald, and Tim A Osswald. "Failure surface development for ABS fused filament fabrication parts". In: *Additive Manufacturing* 28.April (2019), pp. 169–175. ISSN: 2214-8604. DOI: 10.1016/j.addma.2019.05.005. URL: {https://doi.org/10.1016/j.addma.2019.05.005}.

[52] D. D. Phan, J. S. Horner, Z. R. Swain, A. N. Beris, and M. E. Mackay. "Computational fluid dynamics simulation of the melting process in the fused filament fabrication additive manufacturing technique". In: *Additive Manufacturing* 33 (2020).

[53] E. Stammers and W. J. Beek. "The Melting of a Polymer on a Hot Surface". In: *Polymer Engineering and Science* 9 (1969).

[54] O. M. Griffin. "Heat Transfer to Molten Polymers". In: *Polymer Engineering and Science* 12 (1972).

[55] Z. Tadmor and C. G. Gogos. *Principles of Polymer Processing, Second Edition*. John Wiley & Sons, Inc., 2006. ISBN: 0471387703.

[56] H. Liu, Y. Luo, G. Zhang, J. Chen, Z. Yang, and J. Qu. "Modeling of Pressure-Induced Melt Removal Melting in Vane Extruder for Polymer Processing". In: *Advances in Polymer Technology* 33 (2014).

[57] A. J. Poslinski and V. K. Stokes. "Steady melting of rectangular thermoplastic bars induced by hot contacting surfaces". In: *Polymer Engineering and Science* 32 (1992), pp. 1147–1162.

[58] Netzsch GmbH. *Thermal Properties of Polymers*. 2019.

[59] J. L. Colon Quintana, T. Heckner, A. Chrupala, J. Pollock, S. Goris, and T. Osswald. "Experimental Study of Particle Migration in Polymer Processing". In: *Polymer Composites* 40 (2019), pp. 2165–2177.

[60] J. Schindelin, I. Arganda-Carreras, E. Frise, and et al. "Fiji: an open-source platform for biological image analysis". In: *Nature methods* 9 (2012).

[61] V. Alexiades. *Mathematical modeling of melting and freezing processes*. Taylor & Francis, 1993. ISBN: 1-56032-125-3.

[62] *Handbook DSC*. Netzsch GmbH & Co. URL: {https://www.netzsch-thermal-analysis.com/us/landing-pages/handbook-dsc/}.

[63] J. E. K. Schawe. "Influence of processing conditions on polymer crystallization measured by fast scanning DSC". In: *J Therm Anal Calorim* 116 (2014), pp. 1165–1173.

[64] *Two-Phase Flow Modeling Guidelines*. COMSOL. URL: {https://www.comsol.com/support/knowledgebase/1239}.

[65] W. Gleissle and B. Hochstein. "Validity of the Cox-Merz rule for concentrated suspensions". In: *Journal of Rheology* 47 (2003), pp. 897–910.

[66] K. Malkappa and S. Sinha Ray. "Thermal stability, pyrolysis behavior, and fire-retardant performance fo melamine cyanurate@poly (cyclotriphosphazene-co-6, 4'-sulfonyl diphenol) hybrid nanosheet-contaiting polyamide 6 composites". In: *ACS Omega* 4 (2019), pp. 9615–9628.

[67] G. Yuan, B. Yang, Y. Chen, and Y. Jia. "Preparation fo novel phosphorus-nitrogen-silicone grafted graphene oxide and its synergistic effect on intumescent flame-retardant polypropylene composites". In: *RSC Advances* 8 (2018), p. 36286.

[68] B. N. Jang and C. A. Wilkie. "The termal degradation of bisphenol A polycarbonate in air". In: *thermochimica acta* 426 (2005), pp. 73–84.

[69] Li X. G. and M. R. Huang. "Therma degradation of bisphenol A polycarbonate by high-resolution thermogravimetry". In: *Polymer International* 48 (1999), pp. 387–391.

[70] K. L. Erickson. "Thermal decomposition of polymers in nitrogen and in air". In: *Sandia National Laboratories* SAND2007-5405C (2007). URL: {osti.gov/servlets/purl/1147465}.

[71] Rami M. Saeed, J. P. Schlegel, C. Castano, and R. Sawafta. "Uncertainty of Thermal Characterization of Phase Change Material by Differential Scanning Calorimetry Analysis". In: *International Journal of Engineering Research and Technology* 5.1 (2016).

[72] Y. Ma, T. Zhou, G. Su, Y. Li, and A. Zhang. "Understanding the crystallization behavior of polyamide 6/polyamide 66 alloys from the perspective of hydrogen bonds: projection movingwindow 2D correlation FTIR spectroscopy and the enthalpy". In: *Royal Society of Chemistry* 6 (2016), p. 87405. DOI: 10.1039/c6ra09611e.

[73] S.-P. Rwei, P. Ranganathan, and Y.-H. Lee. "Isothermal Crystallization Kinetics Study of Fully Aliphatic PA6 Copolyamides: Effect of Novel Long-Chain Polyamide Salt as a Comonomer". In: *Polymers* 11.472 (2016). DOI: https://doi.org/10.3390/polym11030472.

[74] *Unusual Sample Properties as an Origin of Artifacts*. Mettler Toledo. URL: {https://www.mt.com/us/en/home/supportive_content/matchar_apps/MatChar_UC236.html}.

[75] P. Gramann, J. Cruz, and B. Ralston. *Using differential scanning calorimetry to determine the quality of a PVC part*. The Madison Group. URL: {https://www.madisongroup.com/publications/UsingDSCtoDeterminetheQualityofPVC1.pdf}.

[76] M. Fujiyama and M. Kondou. "Effect of Degree of Polymerization on Gelation and Flow Processability of Poly(vinyl chloride)". In: *Journal of Applied Polymer Science* 92 (2003), pp. 1915–1938.

[77] S. Zajchowski. "Mechanical properties of poly(vinyl chloride) of defined gelation degree". In: *Polimery* 50.11/12 (2005), pp. 890–893.

[78] P. Gill, T. T. Moghadam, and B. Ranjbar. "Differential Scanning Calorimetry Techniques: Applications in Biology and Nanoscience". In: *J Biomol Tech* 21.4 (2010), pp. 167–193.

[79] *Dynamic Mechanical Analysis (DMA)*. PerkinElmer. URL: {https://www.perkinelmer.com/CMSResources/Images/44-74546GDE_IntroductionToDMA.pdf}.

[80] *A Closer Look: Techniques for Obtaining Glass Transition Temperature of Polymeric Materials*. intertek. URL: {https://www.intertek.com/blog/2013-04-15-glass-transition-temperature/#:~:text=DMA\%20measures\%20the\%20response\%20of,temperature\%2C\%20frequency\%2C\%20or\%20both.&text=Compared\%20to\%20DSC\%2C\%20DMA\%20can,changes\%20occurring\%20at\%20the\%20Tg.}.

[81] *A visual Ultimaker troubleshooting guide*. 3DVERKSTAN. URL: {https://support.3dverkstan.se/article/23-a-visual-ultimaker-troubleshooting-guide#underextrusion}.

[82] M. P. Serdeczny, R. Comminal, Md. T. Mollah, D. B. Pedersen, and J. Spangenberg. "Numerical modeling of the polymer flow through the hot-end in filament-based material extrusion additive manufacturing". In: *Additive Manufacturing* (2020). DOI: https://doi.org/10.1016/j.addma.2020.101454.

[83] C. Koch, L. Van Hulle, and N. Rudolph. "Investigation of mechanical anisotropy of the fused filament fabrication process via customized tool path generation". In: *Additive Manufacturing* 16 (2017), pp. 138–145.

[84] *CYCOLAC RESIN MG94*. SABIC. URL: {https://www.sabic.com/en/products/popup.html?q=MG94&grades=113eaad7-e0d8-e611-819b-06b69393ae39}.

[85] Printrun. URL: {https://www.pronterface.com/}.

[86] E3D-Online. URL: {https://e3d-online.dozuki.com/Document/aXLaddMXUlgfEN4b}.

[87] R. V. Morgan, R. S. Reid, A. M. Baker, B. Lucero, and J. D. Bernardin. *Emissivity Measurements of Additively Manufactured Materials*. 2017. URL: {https://permalink.lanl.gov/object/tr?what=info:lanl-repo/lareport/LA-UR-17-20513#:~:text=The\%20emissivity\%20values\%20of\%20common,measured\%20value\%20of\%20approximately\%200.92.}.

[88] F. Pigeonneau, D. Xu, M. Vincent, and J.-F. Agassant. "Heating and flow computations of an amorphous polymer in the liquefier of a material extrusion 3D printer". In: *Additive Manufacturing* 32 (2020).

[89] Guido Van Rossum and Fred L. Drake. *Python 3 Reference Manual*. Scotts Valley, CA: CreateSpace, 2009. ISBN: 1441412697.

[90] J. L. Colon Quintana, S. Heimer, N. Granda Duarte, and T. Osswald. "Implementation of Shear Thinning Behavior in the Fused Filament Fabrication Melting Model: Analytical Solution and Experimental Validation". In: *Additive Manufacturing* 37 (2021). DOI: https://doi.org/10.1016/j.addma.2020.101687.

[91] A. Elkaseer, S. Schneider, and S. G. Scholz. "Experiment-Based Process Modeling and Optimization for High-Quality and Resource-Efficient FFF 3D Printing". In: *Applied Sciences* 10 (2020), p. 2899. DOI: doi:10.3390/app10082899.

[92] P. J. Garcia Plaza E. Nuñez Lopez, M. A. Caminero Torija, and J. M. Chacon Muñoz. "Analysis of PLA Geometric Properties Processed by FFF Additive Manufacturing: Effects of Process Parameters and Plate-Extruder Precision Motion". In: *Polymers* 11 (2019), p. 1581. DOI: {https://doi.org/10.3390/polym11101581}.

[93] *3D Printing Materials Guide: Plastics*. 3D natives. URL: {https://www.3dnatives.com/en/plastics-used-3d-printing110420174/#!}.

[94] G. A. Mazzei Capote, A. Redmann, C. Koch, and N. Rudolph. "Towards a Robust Production of FFF End-User Parts with Improved Tensile Properties". In: *Solid Freeform Fabrication* (2017).

[95] *Solid Density vs. Melt Density*. Beaumont. URL: {https://www.beaumontinc.com/solid-density-vs-melt-density/}.

[96] Y. Sato, K. Inohara, S. Takishima, H. Masuoka, M. Imaizumi, H. Yamamoto, and M. Takasugi. “Pressure-Volume-Temperature Behavior of Polylactide, Poly (butylene succinate), and Poly (butylene succinate-co-adipate)”. In: *Polymer Engineering and Science* 40.12 (2000).

[97] N. Rudolph, J. Chen, and T. Dick. “Understanding the Temperature Field in Fused Filament Fabrication for Enhanced Mechanical Part Performance”. In: *AIP Conf. Proc.* 2055 (2019), pp. 140003–1 –140003–5.

[98] M. Alssabbagh, A. A. Tajuddin, M. Abdulmanap, and R. Zainon. “Evaluation of 3D printing materials for fabrication of a novel multi-functional 3D thyroid phantom for medical dosimetry and image quality”. In: *Radiation Physics and Chemistry* 135 (2017), pp. 106–112.

[99] T. J. Quill, M. K. Smith, T. Zhou, M. G. Shafik Baioumy, J. P. Berenguer, B. A. Cola, K. Kalaitzidou, and T. L. Bougher. “Thermal and mechanical properties of 3D printed boron nitride-ABS composties”. In: *Appl Compos Mater* 25 (2018), pp. 1205–1217.

[100] *Overview of materials for Acrylonitrile Butadiene Styrene (ABS), Molded*. MatWeb. URL: http://www.matweb.com/search/DataSheet.aspx?MatGUID=eb7a78f5948d481c9493a67f0d&ckck=1.

[101] I. U. Perera, N. Narendran, and V. Terentyeva. “Thermal characterization of threedimensional printed components for light-emitting diode lighting system applications”. In: *Opt. Eng.* 57 (2018).

[102] R. Z. Khoo, H. Ismail, and W. S. Chow. “Thermal and Morphological Properties of Poly (lactic acid)/Nanocellulose Nanocomposites”. In: *Procedia Chemistry* 19 (2016), pp. 788–794.

[103] G. A. Mazzei Capote, P. E. V. Oehlmann, J. C. Blanco Campos, G. R. Hegge, and T. A. Osswald. “Trends in force and print speed in Material Extrusion”. In: *Additive Manufacturing: Under Review* (2021).

[104] D. Notzel, R. Eickhoff, and T. Hanemann. “Fused Filament Fabrication of Small Ceramic Components”. In: *Materials* 11 (2018), p. 1463. DOI: 10.3390/ma11081463.

[105] G. P. Greeff and M. Schilling. “Closed loop control of slippage during filament transport in molten material extrusion”. In: *Additive Manufacturing* 14 (2017), pp. 31–38. DOI: 10.1016/j.addma.2016.12.005.

[106] *PLA Technical Data Sheet*. SD3D. URL: {https://www.sd3d.com/wp-content/uploads/2017/06/MaterialTDS-PLA_01.pdf}.

[107] J. L. Colon Quintana, J. Teuwsen, G. Mazzei Capote, and T. Osswald. “Application of the stress interaction failure criterion in platelet composite compression molded parts”. In: *Polymer Composites* (2021), pp. 1–12. DOI: .https://doi.org/10.1002/pc.26084.

[108] J. L. Colon Quintana, A. Redmann, G. A. Mazzei Capote, A. Pérez-Irizarry, A. Bechara, T. A. Osswald, and R. Lakes. "Viscoelastic properties of fused filament fabrication parts". In: *Additive Manufacturing* 28 (2019), pp. 704–710.

[109] J. Puentes, J. L. Colon Quintana, A. Chaloupka, N. Rudolph, and T. A. Osswald. "Moduli development of epoxy adhesives during cure". In: *Polymer Testing* 77 (2019), pp. 54–61. DOI: https://doi.org/10.1016/j.polymertesting.2019.04.010.

[110] J. L. Colon Quintana, T. Heckner, A. Chrupala, J. Pollock, S. Goris, and T. Osswald. "Experimental Study of Particle Migration in Polymer Processing". In: *Polymer Composites* (2019). DOI: DOI10.1002/pc.25018.

[111] J. L. Colon Quintana, T. Heckner, A. Chrupala, S. Goris, J. Pollock, and T. A. Osswald. "Observed Particle Migration During Processing of Polypropylene with Glass Beads". In: *Antec 2018* (2018).

[112] J. L. Colon Quintana, S. Soto Medina, M. Hernandez, and O. M. Suarez. "Study of Thermomechanical Properties of an Al-Zn-Based Composite Reinforced with Dodecaboride Particles". In: *Advances in Materials Science and Engineering* (2016). DOI: {https://doi.org/10.1155/2018/2975234}.

[113] S. L. Zelinka, L. Passarini, J. L. Colon Quintana, S. V. Glass, J. E. Jakes, and A. C. Wiedenhoeft. "Cell Wall Domain and Moisture Content Influence Southern Pine Electrical Conductivity". In: *Wood and Fiber Science* (2015), pp. 54–61. URL: {https://www.fs.usda.gov/treesearch/pubs/52590}.

[114] D. G. Baird and D. I. Collias. *Polymer Processing: Principles and Design, 2nd Edition*. John Wiley & Sons, Inc., 2014. ISBN: 9780470930588.

[115] Amparo Gil, Javier Segura, and Nico M Temme. *Numerical methods for special functions*. Vol. 99. Siam, 2007.

[116] *Gaussian Hypergeometric Function*. MathWorks. URL: {https://www.mathworks.com/matlabcentral/fileexchange/1844-gaussian-hypergeometric-function}.

A. Appendix: Understanding Melting

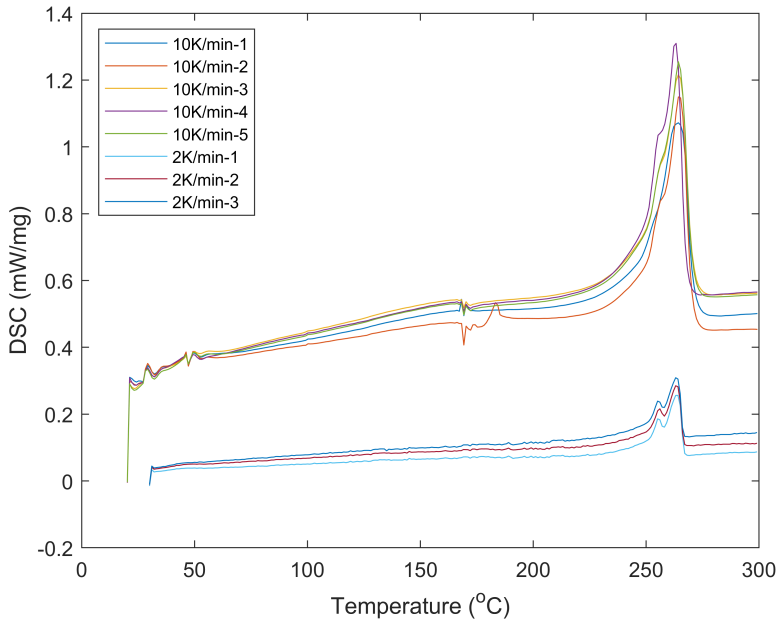

Figure A.1: Comparison of DSC results of PA6 at different heating rate.

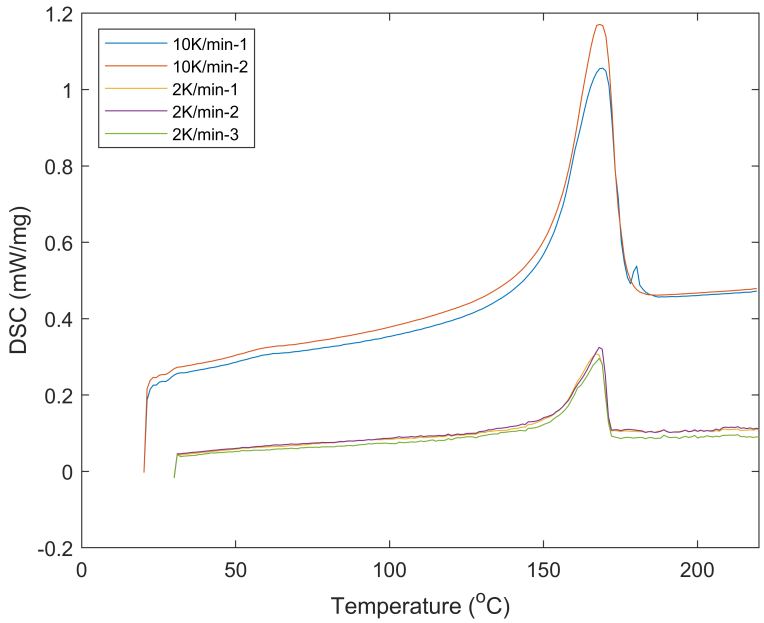

Figure A.2: Comparison of DSC results of PP at different heating rate.

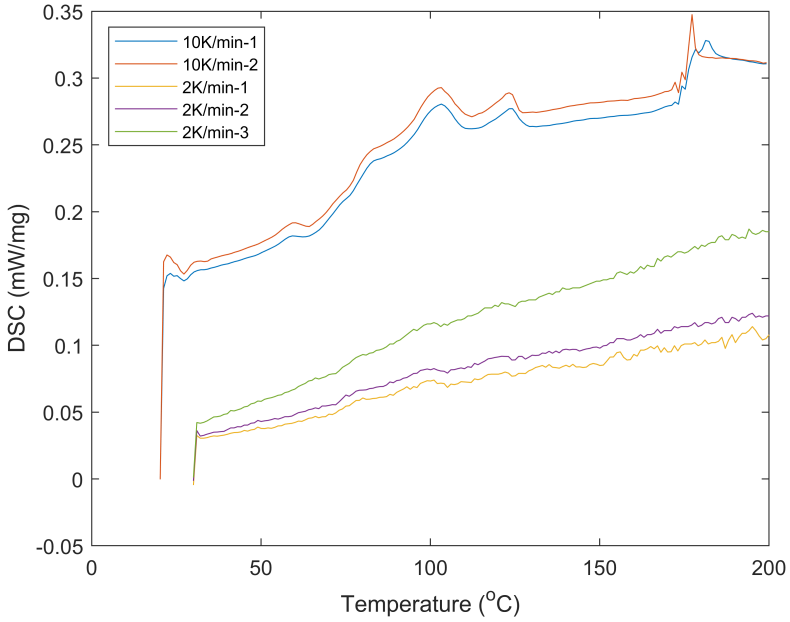

Figure A.3: Comparison of DSC results of PVC at different heating rate.

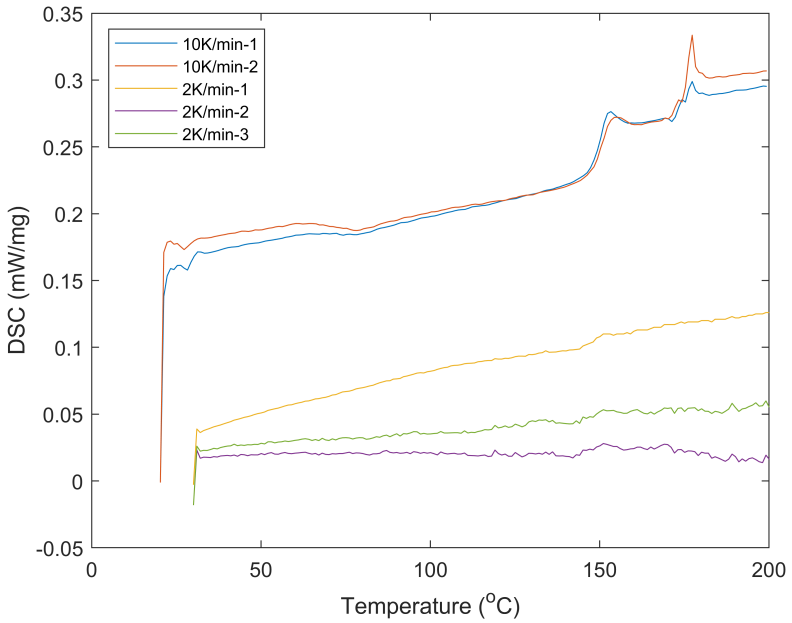

Figure A.4: Comparison of DSC results of PC at different heating rate.

B. Appendix: Shear thinning

B.0.1 Derivation of p_i

The pressure at the capillary entrance, p_i, can be found by using the volumetric flow rate of the circular tube pressure-flow according to [114]. The volumetric flow rate is shown in Equation B.1.

$$Q_{cap} = \frac{\pi R_i^3}{\frac{1}{n}+3}\Big(\frac{R_i}{2m_c}\frac{\Delta P}{L_c}\Big)^{\frac{1}{n}} \tag{B.1}$$

Were $\Delta P = P_i - P_{atm}$ according to the convention of [114]. Equation B.1 is reduced to Equation B.2.

$$Q_{cap} = \frac{\pi R_i^3}{\frac{1}{n}+3}\Big(\frac{R_i}{2m_c}\frac{p_i}{L_c}\Big)^{\frac{1}{n}} \tag{B.2}$$

The volumetric flow rate of the filament material in the molten state is given by Equation B.3.

$$Q_{filament} = \pi R^2(-U_o) \tag{B.3}$$

By applying conservation of mass, the flow rate at the molten state is equal to the flow rate in the capillary zone as shown in Equation B.4.

$$Q_{filament} = Q_{cap} \tag{B.4}$$

Afterward, the equation can be solved to find the pressure at the entrance of the capillary zone (p_i) as shown in Equation B.5.

$$p_i = 2m_c L_c \left[\frac{3n+1}{n}\frac{U_o R_o^2}{R_i^{\frac{3n+1}{n}}}\right]^n \tag{B.5}$$

B.0.2 Materials

The Cycolac®MG94 material produced by SABIC corporation[84] was chosen for this work. This is an ABS-based material traditionally used for injection molding thin-walled parts and extrusion of FFF filament. With a reported Melt Flow Index (MFI) of 11.7 g/10 min, it is an

ideal material for both the FFF and extrusion processes [84]. High MFI allows more material to be printed, which results in faster printing time. The MG94 material was extruded in a setup that consisted of a single screw extruder (Extrudex EDN 45X30D, Germany) with a 45 mm screw diameter and a screw length to screw diameter ratio (L/D) of 30. The hot melt was extruded at 205 ^{o}C through a circular die with a 5.8 mm diameter and then guided through a pre-skinner into a vacuum-assisted, heated water bath (Conair, USA) to cool the extrudate while minimizing void formation. The solidified filament was then passed through a three-axis laser micrometer (LaserLinc, USA) and a belt puller (Conair, USA) configured in a control loop. The filament dimensions were controlled by automatically adjusting the speed of the puller if the readings from the micrometer were out of specification, in this case, a diameter of 1.75 mm with a tolerance of ± 0.02 mm. Finally, the product was wound onto spools using a filament winder. A schematic of the extrusion setup can be seen in Figure B.1.

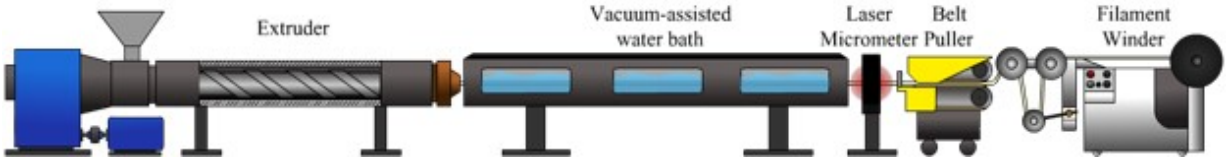

Figure B.1: Schematic of ABS extrusion line. Taken from [94, 108].

B.0.3 Remaining Physical and Mechanical Properties

The material properties and values used for the theoretical model are shown in Table B.1. It was assumed that the melt density is 90% of the solid density for an amorphous material and 80% for a semi-crystalline material [95, 96].

Table B.1: Physical and mechanical properties of PLA and ABS.

Material Properties	PLA MatterHackers	ABS MG94
Melt density (ρ_m) $[kg/m^3]$	1000	954
Solid density (ρ_s) $[kg/m^3]$	1250 [97, 98]	1060 [99]
Specific heat (C_s) $[J/kg - K]$	1800 [97]	1381 [99]
Thermal conductivity (k_m) $[W/m - K]$	0.163 [101]	0.17 [99]
Heat of fusion (λ) $[J/kg]$	93600 [102]	0

B.0.4 DSC Measurements

Determination of the glass transition temperature and the melting temperature was achieved by using a DSC machine (Section 5.4.4). Figure B.2 shows the experimental data for PLA and

ABS. As expected from the ABS material (Figure B.2b), the glass transition temperature can be observed by a step in the baseline of the DSC curve, and it is characteristic for amorphous materials. Here, the mid-T_g is used with a value of 104.5 ^oC. For the PLA material, a step in the baseline data is also found. As done for the ABS, the mid-T_g is also used with a value of 58.9 ^oC. The melting temperature (T_m) corresponds to a peak in the DSC data. In this case, the peak is reached at a temperature of 150.9 ^oC.

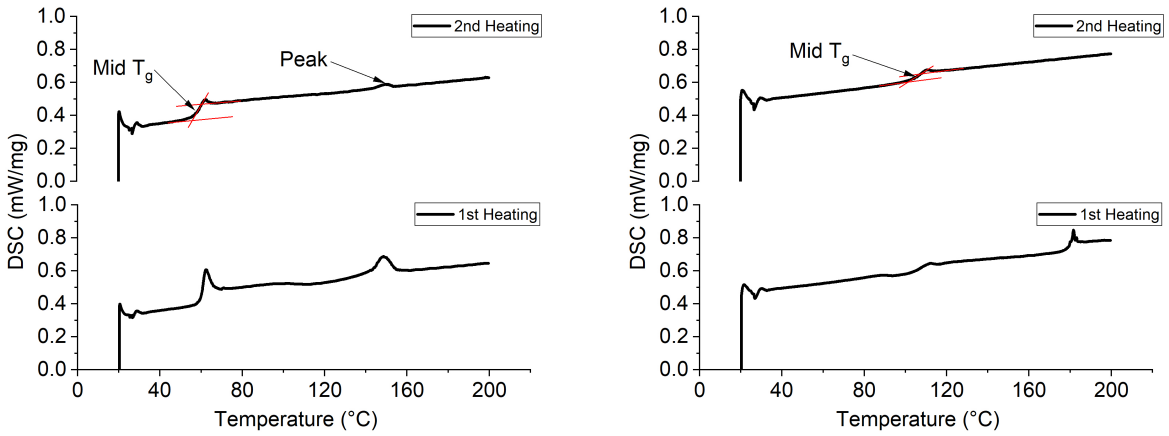

(a) (b)

Figure B.2: Shear rate dependence on complex viscosity as a function of temperature for (a) PLA and (b) ABS.

B.0.5 Rheometric Data

The polymer materials used in the experiments are non-Newtonians which means their viscosity decreased with increasing shear rate. Therefore, a dynamic viscosity test was performed to investigate the linear region for all samples and temperatures as shown in Figure B.3.

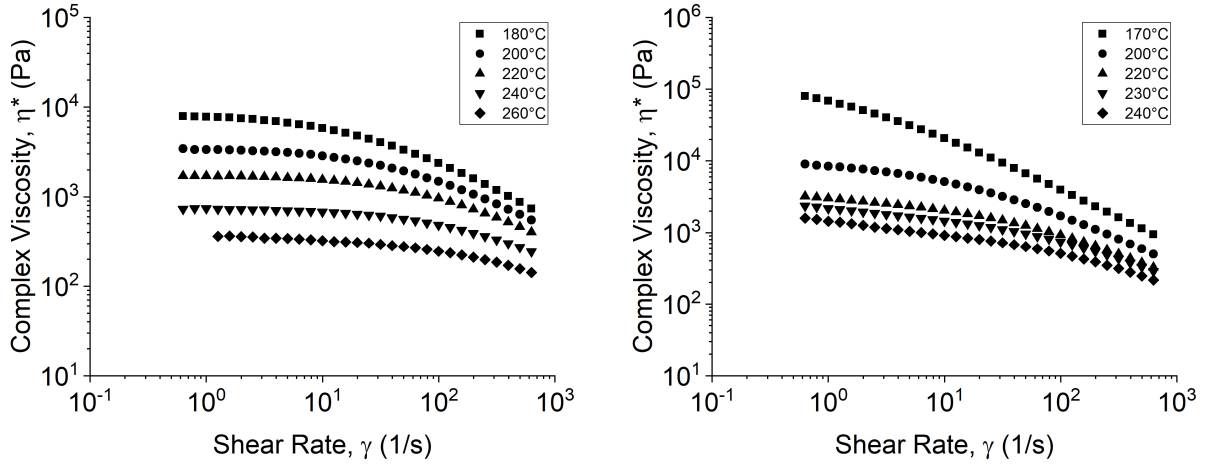

(a) (b)

Figure B.3: Shear rate dependence on complex viscosity as a function of temperature for (a) PLA and (b) ABS.

B.0.6 The Gaussian Hypergeometric function $({}_2F_1(a;b,c;x))$

The Gaussian hypergeometric function is defined by a series within the bound $|x| < 1$

$$ {}_2F_1(a;b,c;x) = \sum_{n=0}^{\infty} \frac{(a)_n (b)_n}{(c_n) n!} x^n $$

where $(q)_n$ is the Pochhammer Symbol

$$ (q)_n = q(q+1)(q+2)...(q+n-1). $$

Beyond this bound, the function is evaluated by analytic continuation schemes. For the interested reader, we refer to [115].

B.0.7 FFF Model Comparison

FFF model comparison using $T_f = Tavg$ and $T_o = 25\ ^oC$. For ABS a melting temperature of $T_m = T_g + 40$ was used. For PLA, the melting temperature used was $T_m = T_m = 150.9\ ^oC$.

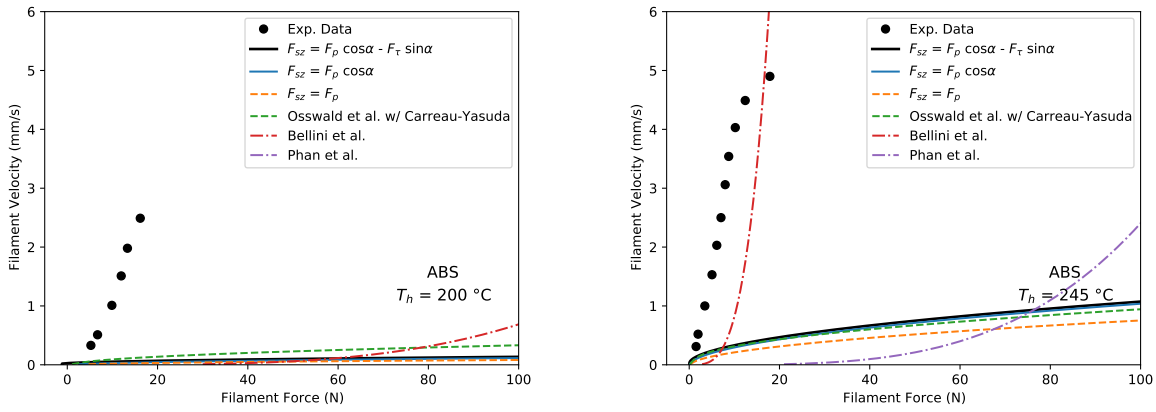

(a) (b)

Figure B.4: Comparison of experimental data with analytical models of ABS at (a) 200 ^oC and (b) 245^oC using $T_f = (T_h + T_g)/2$, $T_m = T_g + 40$, and $T_o = 25^oC$.

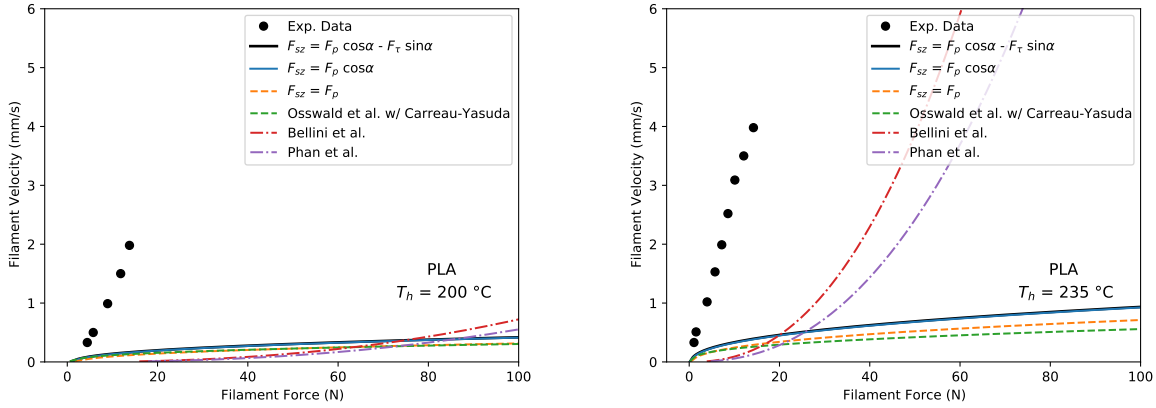

(a) (b)

Figure B.5: Comparison of experimental data with analytical models of PLA at (a) 200 ^oC and (b) 235^oC using $T_f = (T_h + T_m)/2$, $T_m = T_m$, and $T_o = 25^oC$.

B.0.8 Influence of Nozzle Angle

The influence of the nozzle angle in the pressure and deviatoric stress components can be observed in Figure B.6 and Figure B.7.

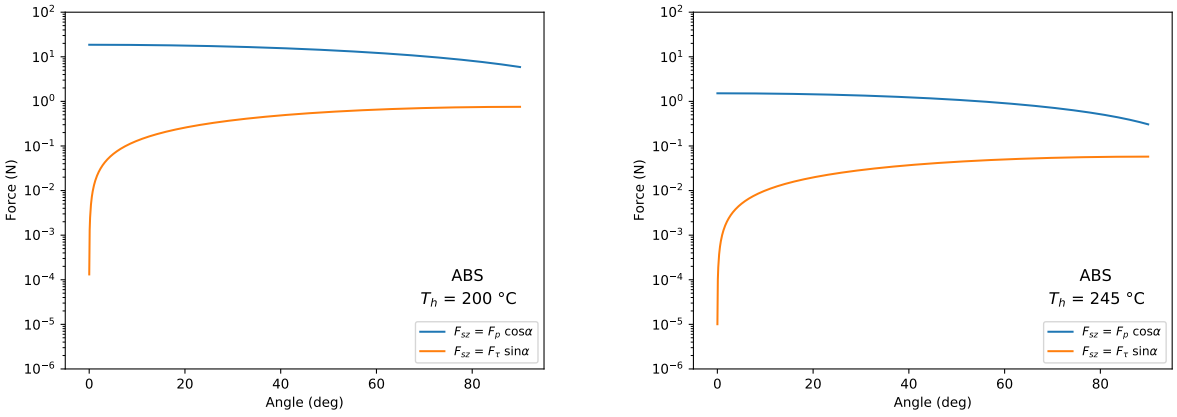

(a) (b)

Figure B.6: Effect of nozzle angle for ABS at (a) 200 ^oC and (b) 245 ^oC using $T_f = T_h$, $T_m = T_g$, $T_o = 70$ ^oC, and $U_{sz} = 2$ mm/s.

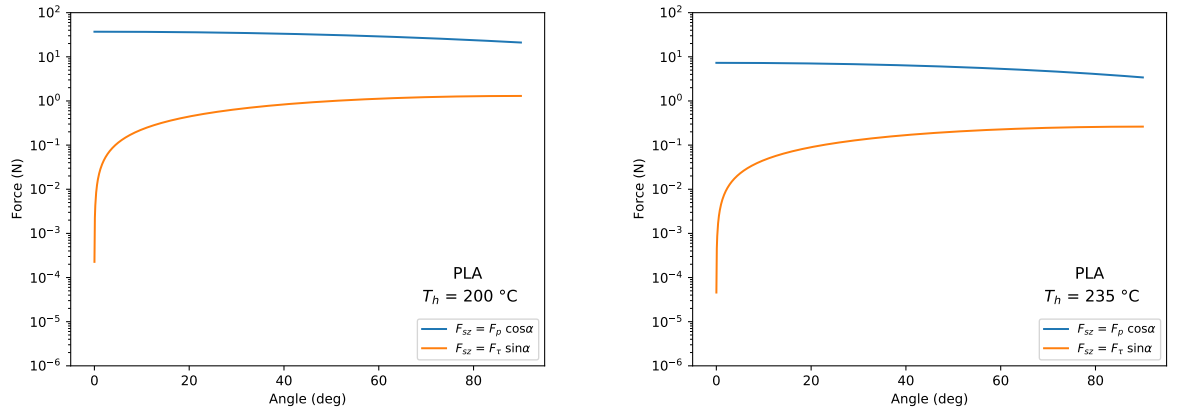

(a) (b)

Figure B.7: Effect of nozzle angle for PLA at (a) 200 ^oC and (b) 235 ^oC using $T_f = T_h$, $T_m = T_g$, $T_o = 50$ ^oC, and $U_{sz} = 2$ mm/s.

C. Appendix: Effect of Radiation and Nozzle Diameter

C.1 Matlab Code: Melting Model

```
clear; %Clean Workspace
clc;    %clean command window

%%
%Geometrical Parameters
R_i = .21e-3;  %Capillary radius
R_o = 1.005e-3;   %Nozzle radius
L_c = .75e-3 ;     %Capillary length
L_N = 10.2e-3;   %Nozzle length
D_B = 2*R_o   ;   %Nozzle diameter
D_C = 2*R_i ;   %Capillary diameter
D_F = 2*R_o ;    %Filament diameter
L_B = L_N    ;   %Barrel length
angle = 54.76;
alpha = deg2rad(angle)  ;   %Nozzle angle for Osswald and Colon
beta = deg2rad(2*(90 - angle));     %Nozzle angle for Bellini and Phan
theta = deg2rad(90 - angle);    %Luo's angle
L1 = L_N;   %Luo's parameter
L3 = L_c;   %Luo's parameter

%Material Properties
rho_s = 1060 ;   %Solid density
rho_m = 0.9*rho_s;     %Melt density for amorphous material. For semicrystalline use (0.8*rho_s)
rho_hat = rho_s/rho_m ;  %Solid to melt density ratio
C_S = 1850 ;     %Specific heat = 1381
k_m = .17  ;             %Thermal conductivity = 0.17
lambd = 0 ;  %heat of fusion

epsilon = 0.916; %emisivity 0.9
sigma = 5.67e-8; %Stefan-Boltzmann constant (W/m^2K^4)

%%%%%%%%%%%%%%%%%%%%%%%%%%%%%%%%
%%%%Processing Conditions %%%
%%%%%%%%%%%%%%%%%%%%%%%%%%%%%%%%

Th = [200 + 273.15 , 210 + 273.15, 220 + 273.15, 230 + 273.15]   ;   %Heater temperatures
Tm = 104.5 + 273.15 ; %Melting temperature
To = 21.1+ 273.15 ;  %Filament at Ambient temperature
T_ref = 200 + 273.15   ;    %Reference temperature for viscosity model
Tf = Th      ;   %Film temperature

%Tilted Parameters
Ri_new = R_i/cos(alpha); %Tilted capillary radius
```

```
Ro_new = R_o/cos(alpha);    %Tilted filament radius

%Velocity Vector
U_sz = linspace(4e-4,1e-2,100); %meters per second
u=1000*U_sz   ;  %milimeters per second

Ao = pi*2*R_o*L_N; %Area of filament inside nozzle
Vo = pi*(R_o^2)*L_N; %Volume of filament inside nozzle
K = (epsilon*sigma*Ao)/(rho_s*Vo*C_S); %Simplification parameter for radiation analysis
%% Radiation effects on initial filament temperature

%Array Creation
A = zeros(length(Th),length(U_sz));
B = zeros(1,length(Th));
C = zeros(length(Th),length(U_sz));
D = zeros(length(Th),length(U_sz));
Tof = zeros(length(Th),length(U_sz));

%Finds filament temperature as a function of filament velocity
for i=1:1:length(Th)
B(i) = log((Th(i) + To)/(Th(i) - To)) + 2*atan(To/Th(i));

    for j = 1:1:length(U_sz)
    Toin = To;
    error = 5;
    A(i,j) = 4* (Th(i)^3)*K*L_N/U_sz(j);
    D(i,j) = A(i,j) + B(i);

    while error > .01
        C(i,j) = log((Th(i) + Toin)/(Th(i) - Toin)) + 2*atan(Toin/Th(i));
        error = abs(D(i,j) - C(i,j));
        Toin = Toin + 1e-5;
    Tof(i,j) = Toin;
    end
    end
end

%%
%%%%%%%%%%%%%%%%%%%%%%%%%%%%%%%%%%%%%%%%%%%%%%%%%%%%%%%%%%%%
%%%% Viscosity Model Parameters of master curve %%%%%
%%%%%%%%%%%%%%%%%%%%%%%%%%%%%%%%%%%%%%%%%%%%%%%%%%%%%%%%%%%%

%Carreau-Yasuda fitting parameters
eta_o = 1.325e4;    %Zero-shear viscosity
lambdcy = 8.675e-2; % consistency index
b = 0.2847; %power law index CY
a = 0.4695; %Dimensionless parameter

%Power law fitting parameters
n = 0.2847    ;  %Power Law i
moo = 4.977e4  ; %Consistency i
N = 1 + (1/n); %Value for Luo's model

%Array Creation
delta = zeros(length(Th),length(U_sz));
gammaf = zeros(length(Th),length(U_sz));
gammac = zeros(1, length(U_sz));

delta_nr = zeros(length(Th),length(U_sz)); %nr = no radiation
gammaf_nr = zeros(length(Th),length(U_sz));

%Calculates melt film thickness and shear rate with and without radiation effect.
for i=1:1:length(Th)
    for j=1:1:length(U_sz)
        delta(i,j)=(k_m*(Th(i)-Tm))/(rho_s*U_sz(j)*(lambd+C_S*(Tm-Tof(i,j))));
```

```
109         gammaf(i,j)=abs(((rho_hat*U_sz(j)*(cos(alpha)))/(delta(i,j)^2))*((Ri_new-Ro_new)*(Ri_new+2*Ro_new)/(Ri_new+
                Ro_new))); %Shear rate used in original paper
110         gammac(j) = abs(((8/3)*(R_o^2)*U_sz(j)*rho_hat)/(R_i^3));
111
112         delta_nr(i,j)=(k_m*(Th(i)-Tm))/(rho_s*U_sz(j)*(lambd+C_S*(Tm-To)));
113         gammaf_nr(i,j)=abs(((rho_hat*U_sz(j)*(cos(alpha)))/(delta_nr(i,j)^2))*((Ri_new-Ro_new)*(Ri_new+2*Ro_new)/(
                Ri_new+Ro_new))); %Shear rate used in original paper
114
115     end
116 end
117
118 %%
119 %%%%%%%%%%%%%%%%%%%%%%%%%%%%%%%%%%
120 %%% Shift factor calculations %%%
121 %%%%%%%%%%%%%%%%%%%%%%%%%%%%%%%%%%
122
123 %Shift factor Parameters
124 %WLF - Parameters
125 C1 = 3.93791;
126 C2 = 128.563;
127
128 %Arrhenious Parameters
129 Ea = 80574.4;   %Activation energy
130 R = 8.3145;     %Gas constant
131
132 %Array Creation
133 aT_cap = zeros(1, length(Th));
134 aT_film = zeros(1, length(Th));
135
136 %Calculation of shift factor
137 for ii = 1:1:length(Th)
138 aT_cap(ii) = 10^((-C1*(Th(ii)-T_ref))/(C2+Th(ii)-T_ref)); %Shift factor for ABS
139 aT_film(ii) = 10^((-C1*(Tf(ii)-T_ref))/(C2+Tf(ii)-T_ref)); %Shift factor for ABS
140 %aT_cap(ii) = exp((-Ea/R)*((1/T_ref)-(1/Th(ii)))); %Shift factor for PLA
141 %aT_film(ii) = exp((-Ea/R)*((1/T_ref)-(1/Tf(ii)))); %Shift factor for PLA
142 end
143
144 %Consistency index Calculation
145 m = zeros(1, length(Th)); %Nozzle
146 K = zeros(1, length(Th)); %Capillary
147
148 %Consistency index with shift
149 for i = 1:1:length(Th)
150 m(i)=aT_film(i)*moo ;%calculate m value for heater temperature for force calculation
151 K(i) = aT_cap(i)*moo; %consistency index of capillary
152 end
153
154 %% Calculate reduce shear rate
155
156 %Array Creation
157 gammac_red = zeros(length(Th),length(U_sz));
158 gammaf_red = zeros(length(Th),length(U_sz));
159
160 %Calculates reduced shear rate
161 for i = 1:1:length(Th)
162     for j = 1:1:length(U_sz)
163             gammac_red(i,j)=aT_cap(i)*gammac(j);
164             gammaf_red(i,j) =aT_film(i)*gammaf(i,j);
165     end
166 end
167
168 %Array Creation
169 eta_film_master_cy = zeros(1,length(U_sz));
170 eta_film_master_pl = zeros(1,length(U_sz));
171 eta_cap_master_pl = zeros(1,length(U_sz));
```

```
eta_cap_master_cy = zeros(1,length(U_sz));

%Calculate viscosity with CY
for j = 1:1:length(U_sz)
    eta_film_master_cy(j) = ((eta_o)*(1+(lambdcy*gammaf_red(1,j))^a)^((b-1)/a));
    eta_film_master_pl(j) = (moo*gammaf_red(1,j)^(n-1));
    eta_cap_master_pl(j)=(moo*gammac_red(1,j)^(n-1));
    eta_cap_master_cy(j)=((eta_o)*(1+(lambdcy*gammac_red(1,j))^a)^((b-1)/a));
end

%Array Creation
etafilm_sf_cy = zeros(length(Th),length(U_sz));
etacap_sf_cy = zeros(length(Th),length(U_sz));
etafilm_sf_pl = zeros(length(Th),length(U_sz));
etacap_sf_pl = zeros(length(Th),length(U_sz));

%Calculation of viscosity for each temperature

for i=1:1:length(Th)
        for j = 1:1:length(U_sz)
        etafilm_sf_cy(i,j) = aT_film(i) * eta_film_master_cy(j);
        etacap_sf_cy(i,j) = aT_cap(i) * eta_cap_master_cy(j);
        etafilm_sf_pl(i,j) = aT_film(i) * eta_film_master_pl(j);
        etacap_sf_pl(i,j) = aT_cap(i) * eta_cap_master_pl(j);
        end
end

Th_c = Th - 273;  %Heater temperature in Celsius

%%
%Calculate Hypergeometric functions
h_1 = (1-n)/2;
h_2 = -n;
h_3 = (5-n)/2;
h_4 = 1+((1-n)/2);
h_5 = (R_i/R_o)^2;
h_6 = 1 - (n/2);
h_7 = 1 + n;
h_8 = 2 + (n/2);
h_9 = (4 +n)/2;
h_10 = 2 - (n/2);
h_11 = 2+n;
h_12 = (5+n)/2;

%Calculate Hypergeometric function
nn = 100;
hyp1=hypergeometric2f1(h_1,h_2,h_3,1,nn);
hyp2=hypergeometric2f1(h_1,h_2,h_3,h_5,nn);
hyp3=hypergeometric2f1(h_1,h_2,h_4,h_5,nn);
hyp4=hypergeometric2f1(h_6,h_2,h_10,h_5,nn);

%Array Creation
F_pressure = zeros(length(Th),length(U_sz));
F_tau = zeros(length(Th),length(U_sz));
F_pi = zeros(length(Th),length(U_sz));
F_sz = zeros(length(Th),length(U_sz));
F_FFF_PL = zeros(length(Th),length(U_sz));
F_FFF_CY = zeros(length(Th),length(U_sz));

F_pressure_nr = zeros(length(Th),length(U_sz));
F_tau_nr = zeros(length(Th),length(U_sz));
F_sz_nr = zeros(length(Th),length(U_sz));

Q = zeros(length(U_sz));
DP_Barrel_Bell= zeros(length(Th),length(U_sz));
```

```
DP_Cont_Bell= zeros(length(Th),length(U_sz));
DP_cap_Bell= zeros(length(Th),length(U_sz));
DP_Total_Bell= zeros(length(Th),length(U_sz));
F_FFF_Bellini= zeros(length(Th),length(U_sz));

DP_alpha_phan = zeros(length(Th),length(U_sz));
DP_o_phan = zeros(length(Th),length(U_sz));
DP_Total_phan = zeros(length(Th),length(U_sz));
F_FFF_Phan = zeros(length(Th),length(U_sz));

F_FFF_Luo = zeros(length(Th),length(U_sz));

Area_cap = pi*R_i^2;       %Area of capillary region
Area_fil = pi*R_o^2;        %Area of filament

for i = 1:1:length(Th)
    for j = 1:1:length(U_sz)
        %Colon with radiation
        F_pressure(i,j) = ((2*pi)/cos(alpha))...
        *(rho_hat*U_sz(j)*((m(i))^(1/n))*((2*n+1)/(4*n))*(delta(i,j)/2)^(-(2*n+1)/(n)) )^(n) * ...
            ((R_o^(2*n))/(1-n)) * ((((gamma(h_4))/(2*gamma(h_3)))*((R_o^(3-n))*((gamma(h_3)*gamma(h_11))/(gamma(
                h_12))) - (R_i^(3-n))*hyp2)) ... ;
            + (-(1/2)*(R_i^(1-n))*hyp3*((R_o^2)-(R_i^2)))) + 2*pi*(K(i)*L_c)*(R_o^2)*(((((3*n+1)/n)*(rho_hat)*(R_o
                ^2))*(R_i^(-(3*n+1)/n)))*U_sz(j))^(n); %Force due to pressure

        F_tau(i,j)= (2*pi)*(m(i)/(2-n))*(((rho_hat*U_sz(j)*(R_o^2)*((delta(i,j))^(-2))*((2*n+1)/n)))*(n))*( ((R_o
            ^(2-n))*(gamma(h_10)*gamma(h_7)/gamma(h_8))) - (R_i^(2-n))*hyp4); %Force due to shear stress
        F_pi(i,j) = (2*K(i)*L_c*(((3*n+1)/n) * ((rho_hat*U_sz(j)*R_o^2)/(R_i^((3*n+1)/n))))^(n))* Area_cap; %force
            to due to capillary region
        F_sz(i,j) = F_pressure(i,j)*cos(alpha) - F_tau(i,j)*sin(alpha) + F_pi(i,j);

        %Colon with no radiation
         F_pressure_nr(i,j) = ((2*pi)/cos(alpha))...
        *(rho_hat*U_sz(j)*((m(i))^(1/n))*((2*n+1)/(4*n))*(delta_nr(i,j)/2)^(-(2*n+1)/(n)) )^(n) * ...
            ((R_o^(2*n))/(1-n)) * ((((gamma(h_4))/(2*gamma(h_3)))*((R_o^(3-n))*((gamma(h_3)*gamma(h_11))/(gamma(
                h_12))) - (R_i^(3-n))*hyp2)) ... ;
            + (-(1/2)*(R_i^(1-n))*hyp3*((R_o^2)-(R_i^2)))) + 2*pi*(K(i)*L_c)*(R_o^2)*(((((3*n+1)/n)*(rho_hat)*(R_o
                ^2))*(R_i^(-(3*n+1)/n)))*U_sz(j))^(n); %Force due to pressure

        F_tau_nr(i,j)= (2*pi)*(m(i)/(2-n))*(((rho_hat*U_sz(j)*(R_o^2)*((delta_nr(i,j))^(-2))*((2*n+1)/n)))*(n))*(
             ((R_o^(2-n))*(gamma(h_10)*gamma(h_7)/gamma(h_8))) - (R_i^(2-n))*hyp4); %Force due to shear stress
        F_sz_nr(i,j) = F_pressure_nr(i,j)*cos(alpha) - F_tau_nr(i,j)*sin(alpha) + F_pi(i,j);

        %Osswald power law
        F_FFF_PL(i,j) = (-(6*pi*etafilm_sf_pl(i,j)*U_sz(j)*(rho_s/rho_m)*(R_o^4))/(cos(alpha)*(delta(i,j)^3)))* ...
            ((log(R_i/R_o) + (3/4) + (1/4)*(R_i/R_o)^4 - (R_i/R_o)^2)) + ...
            (8*pi*etacap_sf_pl(i,j)*L_c*U_sz(j)*(rho_s/rho_m)*((R_o/R_i)^4-(R_o/R_i)^2)); % Original FFF model
                using power law model for viscosity

        %Osswald carreau-yasuda
        F_FFF_CY(i,j) = (-(6*pi*etafilm_sf_cy(i,j)*U_sz(j)*(rho_s/rho_m)*(R_o^4))/(cos(alpha)*(delta(i,j)^3)))* ...
            ((log(R_i/R_o) + (3/4) + (1/4)*(R_i/R_o)^4 - (R_i/R_o)^2)) + ...
            (8*pi*etacap_sf_cy(i,j)*L_c*U_sz(j)*(rho_s/rho_m)*((R_o/R_i)^4-(R_o/R_i)^2)); % Original FFF model
                using Carreau-Yasuda model for viscosity

        %Bellini Model
        Q(j) = Area_fil * U_sz(j);
        DP_Barrel_Bell(i,j) =   m(i)*(  ((1 + 3*n)/(4*n))* ((32*Q(j))/(pi*(2*R_o)^3)) )^(n) * ((4*L_B)/(2*R_o));
        DP_Cont_Bell(i,j) = m(i) * (  ((1 + 3*n)/(4*n))* ((32*Q(j))/(pi)) )^(n)*( (1/((2*R_i)^(3*n))) - (1/((2*R_o)
             ^(3*n)))) * (2/(3*n*tan(beta/2)));
        DP_cap_Bell(i,j) = m(i)*(  ((1 + 3*n)/(4*n))* ((32*Q(j))/(pi*(2*R_i)^3)) )^(n)* ((4*L_c)/(2*R_i));
        DP_Total_Bell(i,j) = DP_Barrel_Bell(i,j) + DP_Cont_Bell(i,j) + DP_cap_Bell(i,j);
        F_FFF_Bellini(i,j) = (DP_Total_Bell(i,j))* Area_fil;

        %Phan Model
```

```
292         DP_alpha_phan (i,j) = m(i) * (  ((1 + 3*n)/(4*n))* ((32*Q(j))/(pi*(2*R_i)^3)) )^(n) * (2/(3*n*tan(beta/2)))
                 + 5*m(i)*((2^(1-n))/(3*n))*tan(beta/2)^(n)*((32*Q(j))/(pi*(2*R_i)^3))^(n);
293         DP_o_phan (i,j) = m(i) * (  ((1 + 3*n)/(4*n))* ((32*Q(j))/(pi*(2*R_i)^3)) )^(n) *(1.18/(n^(0.7)));
294         DP_Total_phan(i,j) = DP_alpha_phan(i,j) + DP_o_phan(i,j) + DP_cap_Bell(i,j);
295         F_FFF_Phan(i,j) = DP_Total_phan(i,j)* Area_fil;
296
297         %Luo Model
298         F_FFF_Luo(i,j) = pi*(R_o^2)*(U_sz(j)^n) * (2*K(i)*L1 * ((N+2)/(R_o^(N)))^(n) + ((2*K(i))/(3*n*sin(theta)))
                *((3*(3*n+1)*(R_o^2)*sin(theta))/(4*n*(1-cos(theta))^(2)*(1+2*cos(theta))))^(n) * ((1/(R_i^(3*n))) -
                (1/(R_o^(3*n))))  + K(i)*(((3*n+1)/(n))*((R_o^2)/(R_i^3)))^(n)*(1.18/(n^(.7))) + 2*K(i)*L3*((N+2)/(R_i
                ^N))^n);
299     end
300 end
301
302 %% Experimental Values
303
304 F_abs_200_4mm = [4.65778997     5.866363697     8.446543081     10.54936033     11.21588916     13.18920024
        16.55766446     21.23686135     24.74688072];
305 V_abs_200_4mm = [0.3369589682   0.5200897478    0.9962945739    1.518380519     2.031550906     2.546479384
        2.992758256     3.43787655      3.641130981];
306
307 F_abs_210_4mm = [3.683622022    4.381749343     6.279326273     7.820651268     8.338273008     9.807873847
        11.95651701     15.31943478     18.81267754     21.76747721     23.26077215];
308 V_abs_210_4mm = [0.3494877206   0.5203487127    1.029069716     1.549498227     2.041580078     2.570490143
        3.061013382     3.523121015     3.876564077     4.147987478     4.182751435];
309
310 F_abs_220_4mm = [1.826572904    2.664615473     4.200714244     5.713427785     6.646119967     8.037127976
        9.498650197     12.07589999     14.75387469     18.47179978     23.89771862     24.86340946];
311 V_abs_220_4mm = [0.3517343437   0.5302820305    1.042136242     1.563198096     2.057095936     2.590438156
        3.050738573     3.569498212     4.030306408     4.471362305     4.90235349      4.871348006];
312
313 F_abs_230_4mm = [1.672047942    2.487999262     4.238098217     5.443044962     6.358893547     7.57993647
        8.761791975     9.644631429     12.3787902      15.12220209     19.38474336     25.59516422     22.31588792];
314 V_abs_230_4mm = [0.3520154956   0.5195799931    1.038670663     1.572369263     2.079192302     2.584018692
        3.032635627     3.609738974     4.045281373     4.535769526     4.97631323      5.281428181     5.162784872];
315
316 %% Plot - Filament temperature
317
318 Tof_C = Tof - 273.15; %Filament initial temperature in Celsius
319
320 figure,
321 Tof1=loglog(u,Tof_C(1,:),'LineWidth',3);
322 hold on
323 Tof2=loglog(u,Tof_C(2,:),'LineWidth',3);
324 Tof3=loglog(u,Tof_C(3,:),'LineWidth',3);
325 Tof4=loglog(u,Tof_C(4,:),'LineWidth',3);
326 hold off
327 legend([Tof1 Tof2 Tof3 Tof4],'200^{o}C','210^{o}C','220^{o}C','230^{o}C','FontSize',11)
328 xlabel('Filament velocity, U_{sz} (mm/s)','FontSize',12)
329 ylabel('Filament initial temperature, T_{of} (^{o}C)','FontSize',12)
330 ylim([20 100])
331 text(.8,25,'ABS, 0.4 mm','FontSize',14)
332 set(gcf,'PaperUnits','inches','PaperPosition',[0 0 7 5])
333 print('-r600','ABS_04mm_Tm104_Tof','-dpng')
334
335 %% Plot - Melt film thickness
336
337 %Melt film thickness in milimeters
338 delta_mm = delta*(10^3);
339 delta_nr_mm = delta_nr*(10^3);
340
341 figure,
342 delta1 = loglog(u,delta_mm(1,:),'-r','LineWidth',3);
343 hold on
344 delta2 = loglog(u,delta_mm(2,:),'-g','LineWidth',3);
```

```
delta3 = loglog(u,delta_mm(3,:),'-b','LineWidth',3);
delta4 = loglog(u,delta_mm(4,:),'-k','LineWidth',3);
%no rad
delta5 = loglog(u,delta_nr_mm(1,:),'--r','LineWidth',3);
delta6 = loglog(u,delta_nr_mm(2,:),'--g','LineWidth',3);
delta7 = loglog(u,delta_nr_mm(3,:),'--b','LineWidth',3);
delta8 = loglog(u,delta_nr_mm(4,:),'--k','LineWidth',3);
hold off
legend([delta1 delta2 delta3 delta4 delta5 delta6 delta7 delta8],'200^{o}C rad','210^{o}C rad','220^{o}C rad','
    230^{o}C rad','200^{o}C no rad','210^{o}C no rad','220^{o}C no rad','230^{o}C no rad','FontSize',11)
xlabel('Filament velocity, U_{sz} (mm/s)','FontSize',12)
ylabel('Melt film thickness, \delta (mm)','FontSize',12)
text(.8,.02,'ABS, 0.4 mm','FontSize',14)
ylim([10^-2 10])
set(gcf,'PaperUnits','inches','PaperPosition',[0 0 7 5])
print('-r600','ABS_04mm_Tm104_delta','-dpng')

%%
figure,
subplot(2,2,1)
plot(F_abs_200_4mm,V_abs_200_4mm,'ok','MarkerSize',8,'MarkerFaceColor','k');
hold on
plot(F_sz(1,:),u, '-k','LineWidth',3);  %Model at 200C
plot(F_sz_nr(1,:),u, '--k','LineWidth',3);  %Model at 200C
plot(F_FFF_PL(1,:),u,'--r','LineWidth',2);
plot(F_FFF_CY(1,:),u,'.-b','LineWidth',2);
plot(F_FFF_Bellini(1,:),u,':c','LineWidth',2);
plot(F_FFF_Phan(1,:),u,'--m','LineWidth',2);
plot(F_FFF_Luo(1,:),u,'-g','LineWidth',2);
hold off
xlim([0 50])
ylim([0 8])
xlabel('Filament force (N)','FontSize',11)
ylabel('Filament velocity (mm/s)','FontSize',11)
legend('Exp Data','Colon et.al with rad','Colon et.al no rad','Osswald w/ PL','Osswald w/ CY','Bellini et. al','
    Phan et. al','Luo et. al','FontSize',5)
text(5,7,'ABS','FontSize',8)
text(5,6.25,'T_{h} = 200^{o}C','FontSize',8)
text(5,5.5,'0.4 mm','FontSize',8)

subplot(2,2,2)
plot(F_abs_210_4mm,V_abs_210_4mm,'ok','MarkerSize',8,'MarkerFaceColor','k')
hold on
plot(F_sz(2,:),u, '-k','LineWidth',3)   %Model at 210C
plot(F_sz_nr(2,:),u, '--k','LineWidth',3)   %Model at 210C
plot(F_FFF_PL(2,:),u,'--r','LineWidth',2);
plot(F_FFF_CY(2,:),u,'.-b','LineWidth',2);
plot(F_FFF_Bellini(2,:),u,':c','LineWidth',2);
plot(F_FFF_Phan(2,:),u,'--m','LineWidth',2);
plot(F_FFF_Luo(2,:),u,'-g','LineWidth',2);
hold off
xlim([0 50])
ylim([0 8])
xlabel('Filament force (N)','FontSize',11)
ylabel('Filament velocity (mm/s)','FontSize',11)
legend('Exp Data','Colon et.al with rad','Colon et.al no rad','Osswald w/ PL','Osswald w/ CY','Bellini et. al','
    Phan et. al','Luo et. al','FontSize',5)
text(1,7,'ABS','FontSize',8)
text(1,6.25,'T_{h} = 210^{o}C','FontSize',8)
text(1,5.5,'0.4 mm','FontSize',8)

subplot(2,2,3)
plot(F_abs_220_4mm,V_abs_220_4mm,'ok','MarkerSize',8,'MarkerFaceColor','k')
hold on
plot(F_sz(3,:),u, '-k','LineWidth',3)   %Model at 220C
```

```
plot(F_sz_nr(3,:),u, '--k','LineWidth',3)   %Model at 220C
plot(F_FFF_PL(3,:),u,'--r','LineWidth',2);
plot(F_FFF_CY(3,:),u,'.-b','LineWidth',2);
plot(F_FFF_Bellini(3,:),u,':c','LineWidth',2);
plot(F_FFF_Phan(3,:),u,'--m','LineWidth',2);
plot(F_FFF_Luo(3,:),u,'-g','LineWidth',2);
hold off
xlim([0 50])
ylim([0 8])
xlabel('Filament force (N)','FontSize',11)
ylabel('Filament velocity (mm/s)','FontSize',11)
legend('Exp Data','Colon et.al with rad','Colon et.al no rad','Osswald w/ PL','Osswald w/ CY','Bellini et. al','
    Phan et. al','Luo et. al','FontSize',5)
text(35,2,'ABS','FontSize',8)
text(35,1.25,'T_{h} = 220^{o}C','FontSize',8)
text(35,.5,'0.4 mm','FontSize',8)

subplot(2,2,4)
hold on
plot(F_abs_230_4mm,V_abs_230_4mm,'ok','MarkerSize',8,'MarkerFaceColor','k')
plot(F_sz(4,:),u, '-k','LineWidth',3)  %Model at 230C
plot(F_sz_nr(4,:),u, '--k','LineWidth',3)  %Model at 230C
plot(F_FFF_PL(4,:),u,'--r','LineWidth',2);
plot(F_FFF_CY(4,:),u,'.-b','LineWidth',2);
plot(F_FFF_Bellini(4,:),u,':c','LineWidth',2);
plot(F_FFF_Phan(4,:),u,'--m','LineWidth',2);
plot(F_FFF_Luo(4,:),u,'-g','LineWidth',2);
hold off
xlim([0 50])
ylim([0 8])
xlabel('Filament force (N)','FontSize',11)
ylabel('Filament velocity (mm/s)','FontSize',11)
legend('Exp Data','Colon et.al with rad','Colon et.al no rad','Osswald w/ PL','Osswald w/ CY','Bellini et. al','
    Phan et. al','Luo et. al','FontSize',5)
text(30,2,'ABS','FontSize',8)
text(30,1.25,'T_{h} = 230^{o}C','FontSize',8)
text(30,.5,'0.4 mm','FontSize',8)

print('-r600','ABS_04mm_Tm104','-dpng')
```

C.2 Matlab Code: Hypergeometric Function

The Hypergeometric function was imported from [116].

```
function z=hypergeometric2f1(a,b,c,x,n)
% HYPERGEOMETRIC2F1 Computes the hypergeometric function
% using a series expansion:
%
%    f(a,b;c;x)=
%
%    1 + [ab/1!c]x + [a(a+1)b(b+1)/2!c(c+1)]x^2 +
%    [a(a+1)(a+2)b(b+1)(b+2)/3!c(c+1)(c+2)]x^3 + ...
%
% The series is expanded to n terms
%
% This function solves the Gaussian Hypergeometric Differential Equation:
%
%     x(1-x)y'' + {c-(a+b+1)x}y' - aby = 0
%
% The Hypergeometric function converges only for:
% |x| < 1
% c != 0, -1, -2, -3, ...
%
```

```
%
% Comments to:
% Diego Garcia   — d.garcia@ieee.org
% Chuck Mongiovi — mongiovi@fast.net
% June 14, 2002
if nargin ~= 5
    error('Usage: hypergeometric2f1(a,b,c,x,n) ——> Wrong number of arguments')
end
if (n <= 0 | n ~= floor(n))
    error('Usage: hypergeometric2f1(a,b,c,x,n) ——> n has to be a positive integer')
end
if (abs(x) > 1)
    error('Usage: hypergeometric2f1(a,b,c,x,n) ——> |x| has to be less than 1')
end
if (c <= 0 & c == floor(c))
    error('Usage: hypergeometric2f1(a,b,c,x,n) ——> c != 0, —1, —2, —3, ...')
end
z = 0;
m = 0;
while (m<n)
    if (m == 0)
        delta = 1;
    else
        delta = delta .* x .* (a + (m — 1)) .* (b + (m—1)) ./ m ./ (c + (m—1));
   end
   z = z + delta;
   m = m + 1;
end
```